UNIVERSITY OF NAIROBI

DESIGN OF EFFICIENT AND STABLE NON-FULLERENE ACCEPTOR-BASED ORGANIC SOLAR CELLS BY BUFFER LAYER MODIFICATION
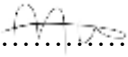
BY

MBILO MWENDE

I80/57296/2020

A Thesis Submitted in Fulfillment of the Requirements for Award of the Degree of Doctor of Philosophy in Physics of the University of Nairobi

2024

DECLARATION

I declare that this thesis is my original work and has not been submitted elsewhere for examination, award of a degree or publication. Where other people's work or my own work has been used, this has properly been acknowledged and referenced in accordance with the University of Nairobi's requirements

Signature…………………………………....Date………..11.7.2024.………..…….

Mbilo Mwende.

I80/57296/2020

Department of Physics, Faculty of Science and Technology, University of Nairobi

This thesis is submitted for examination with our approval as research supervisors

Signature   Date

Prof. Julius M. Mwabora   July 12.2024
Department of Physics
University of Nairobi
P.O Box 30197-00100 Nairobi Kenya
mwabora@uonbi.ac.ke

Prof. Robinson J. Musembi   July. 11, 2024
Department of Physics
University of Nairobi
P.O Box 30197-00100 Nairobi Kenya
musembirj@uonbi.ac.ke

Dr. Won Suk Shin   July. 11, 2024
Energy Materials Research Center
Korea Research Institute of Chemical Technology
141 Gajeongro, Yuseong, Daejeon 34114, Korea
shinws@krict.re.kr

ii

DEDICATION

I dedicate this work to my family and many friends who cheered me throughout my PhD journey.

ACKNOWLEDGEMENTS

ABSTRACT

The practical applications of organic solar cells (OSCs) are hindered by their insufficient lifetimes. Zinc oxide (ZnO) and tin (IV) oxide (SnO_2), which are widely used electron transport layer (ETL) materials in OSCs, suffer from photocatalytic effects and surface defects. These problems limit the power conversion efficiency (PCE) and stability of OSCs and must be solved to realise the practical application of OSCs. This study focuses on solving these problems by modifying ZnO and SnO_2 ETL materials with commercial ultraviolet resins based on polyurethane diacrylate and urethane acrylate, whose given names by the manufacturing company were SAR and OCS, respectively.

In this study, the OSCs ETL, modification interlayer, and photoactive layer were fabricated by spin coating technique on indium tin oxide (ITO) patterned substrates. The hole transport layer (HTL) and top silver (Ag) electrode were deposited using the thermal evaporation method. The interfacial modification properties, such as hydrophobicity, work function (WF), and surface defects, were studied using contact angle measurement, ultraviolet photoelectron spectroscopy (UPS), X-ray photoelectron spectroscopy (XPS), and photoluminescence (PL) spectroscopy. Modifying ZnO and SnO_2 with SAR and OCS resins improved the contact angles and reduced the surface free energy, thus enhancing the interfacial contact between ETLs and the photoactive layer. UPS analysis showed that SAR and OCS modification reduced the WF of ETLs, resulting in energy-level alignment with the photoactive layer. A significant decrease in the surface defects of ETLs upon SAR and OCS resin modification was observed in XPS and PL analyses. The improved interfacial contact at the ETLs/photoactive layer, reduced work functions, and surface defects contributed to the PCE improvement of the OSCs based on ZnO ETL from 13.6% to 14.6% and those based on SnO_2 ETL from 13.8% to 14.4%.

The photocatalytic activity of ZnO and SnO_2, which decomposes the organic photoactive layer material upon light illumination, was found to be suppressed through SAR and OCS modification. The suppressed photocatalytic effect contributed to the improvement in the photostability of OSCs. In addition, the SAR and OCS resins formed a cross-linked network on ETLs which was resistant to thermal stress, contributing to improved OSC thermal stability. Thus, this study presents a good approach to enhance the performance and stability of OSCs utilising ultraviolet resins.

TABLE OF CONTENTS

LIST OF TABLES

LIST OF FIGURES

xiv

LIST OF ABBREVIATIONS AND SYMBOLS

μ_e	Electron Mobility
2-ME	2-methoxyethanol
A	Acceptor
AFM	Atomic Force microscopy
Ag	Silver
Al	Aluminum
Al_2O_3	Aluminum oxide
ALD	Atomic Layer Deposition
BHJ	Bulk heterojunction
BTP-eC9	2,2'-((2Z,2'Z)-((12,13-bis(2-butyloctyl)-3,9-dinonyl-12,13-dihydro-[1,2,5]thiadiazolo[3,4-e]thieno[2'',3'':4',5']thieno[2',3':4,5]pyrrolo[3,2-g]thieno[2',3':4,5]thieno[3,2-b]indole-2,10-diyl)bis(methanylylidene))bis(5,6-dichloro-3-oxo-2,3-dihydro-1H-indene-2,1 diylidene))dimalononitrile
Ca	Calcium
CA	Contact angle
CB	Conduction Band
Cb	Chlorobenzene
CF	Chloroform
CN	Chloronaphthalene
Co^{2+}	Cobalt metal ion
D-A	Donor-acceptor
D	Donor

D18	Poly[(2,6-(4,8-bis(5-(2-ethylhexyl-3-fluoro)thiophen-2-yl)-benzo[1,2-b:4,5-b']dithiophene))-alt-5,5'-(5,8-bis(4-(2-butyloctyl)thiophen-2-yl)dithieno[3',2':3,4;2'',3'':5,6]benzo[1,2-c][1,2,5]thiadiazole)]
D2	Deuterium
DIM	Diiodomethane
DIO	1, 8 diiodooctane
E_{BE}	Binding energy
ECM	Equivalent Circuit Model
E_{cutoff}	Cutoff energy
E_g	Bandgap
EIS	Electrochemical Impedance Spectroscopy
E_{KE}	Kinetic energy
EQE	External Quantum Efficiency
ETL	Electron Transport Layer
E_v	Vacuum level
FF	Fill Factor
GHG	Greenhouse Gas
He	Helium
HOMO	Highest Occupied Molecular Orbital
HTL	Hole Transport Layer
hv	Photon energy
InP	Indium Phosphide
iOSCs	Inverted Organic Solar Cells

IPA	Isopropyl Alcohol
IPCE	Incident photon to current conversion efficiency
ITO	Indium Tin Oxide
J-V	Current-voltage
J_m	Current at maximum power
J_{ph}	Photocurrent density
J_{sat}	Saturated current density
J_{sc}	Short circuit current density
L8-BO	2,2'-((2Z,2'Z)-((3,9-bis(2-butyloctyl)-12,13-bis(2-ethylhexyl)-12,13-dihydro-[1,2,5]thiadiazolo[3,4-e]thieno[2'',3'':4',5']thieno[2',3':4,5]pyrrolo[3,2-g]thieno[2',3':4,5]thieno[3,2-b]indole-2,10-diyl)bis(methanylylidene))bis(5,6-difluoro-3-oxo-2,3-dihydro-1H-indene-2,1-diylidene))dimalononitrile
LED	Light emitting diode
LS	Light soaking
LUMO	Lowest Unoccupied Molecular Orbital
MoO_3	Molybdenum oxide
η	Efficiency
N3	2,2'-((2Z,2'Z)-((12,13-bis(3-ethylheptyl)-3,9-diundecyl-12,13-dihydro-[1,2,5]thiadiazolo[3,4-e]thieno[2'',3'':4',5']thieno[2',3':4,5]pyrrolo[3,2-g]thieno[2',3':4,5]thieno[3,2-b]indole-2,10-diyl)bis(methanylylidene))bis(5,6-difluoro-3-oxo-2,3-dihydro-1H-indene-2,1-diylidene))dimalononitrile
N_e	Number of electrons
NFAs	Non-fullerene acceptors
N_p	Number of photons
NREL	National Renewable Energy Laboratory

N_{trap}	Trap density
^{o}C	Degrees Celsius
OPVs	Organic Photovoltaics
OSCs	Organic solar cells
P (E, T)	Exciton dissociation probability as a function of electric filed (E) and temperature (T)
ϕ	Phase angle
PCE	Power conversion efficiency
PEDOT: PSS	Poly (3, 4-ethylenedioxythiophene) doped with polystyrene sulfonate
P_{in}	Incident light power
PL	Photoluminescence
P_{light}	Light intensity
P_m	Maximum power
PM6	Poly[(2,6-(4,8-bis(5-(2-ethylhexyl-3-fluoro)thiophen-2-yl)-benzo[1,2-b:4,5-b']dithiophene))-alt-(5,5-(1',3'-di-2-thienyl-5',7'-bis(2-ethylhexyl)benzo[1',2'-c:4',5'-c']dithiophene-4,8-dione)]
PTFE	Polytetrafluoroethylene
PV	Photovoltaic
RH	Relative humidity
RMS	Root mean square
RS	Raman Scattering
R_{series}	Series resistance
$R_{surface}$	Surface resistance
SCLC	Space Charge Limited Current

SnO_2	Tin (IV) oxide
T_{80}	Time required for efficiency to drop to 80%
UPS	Ultraviolet Photoelectron Spectroscopy
UV-Vis	Ultraviolet visible
UV	Ultraviolet
UVO	Ultraviolet Ozone
V_a	Applied voltage
VB	Valence Band
V_{eff}	Effective voltage
V_m	Voltage at maximum power
V_o	Oxygen vacancy
V_{oc}	Open circuit voltage
V_{TFL}	Trap-filled limited voltage
WFs	Work functions
Xe	Xenon
XPS	X-ray Photoelectron Spectroscopy
Y6-BO	2,2'-((2Z,2'Z)-((12,13-bis(2-butyloctyl)-3,9-diundecyl-12,13-dihydro-[1,2,5]thiadiazolo[3,4-e]thieno[2'',3'':4',5']thieno[2',3':4,5]pyrrolo[3,2-g]thieno[2',3':4,5]thieno[3,2-b]indole-2,10-diyl)bis(methanylylidene))bis(5,6-difluoro-3-oxo-2,3-dihydro-1H-indene-2,1-diylidene))dimalononitrile
Y6	2,2'-((2Z,2'Z)-((12,13-bis(2-ethylhexyl)-3,9-diundecyl-12,13-dihydro-[1,2,5]thiadiazolo[3,4-e]thieno[2'',3'':4',5']thieno[2',3':4,5]pyrrolo[3,2-g]thieno[2',3':4,5]thieno[3,2-b]indole-2,10-diyl)bis(methanylylidene))bis(5,6-difluoro-3-oxo-2,3-dihydro-1H-indene-2,1-diylidene))dimalononitrile
ZnO	Zinc Oxide

ZnP	Zinc phosphide
γ	Surface free energy
ε	Dielectric constant of a material
ε_o	Dielectric constant in vacuum
θ_C	Contact angle
θ_w	Water contact angle
θ_{dim}	Diiodomethane contact angle
Ω	Ohms
Φ	Work function

CHAPTER ONE: INTRODUCTION

1.1 Background to the Study

The demand for clean energy is currently increasing, a trend that has been attributed to the continuous growth of the global world population, urbanisation, improvement in quality of life, and changing lifestyle, among other factors. This has had an immense impact on the socioeconomic activities, thus expanding urbanisation and industrialisation (Ebrahimi and Rahmani, 2019). However, energy sustainability remains a major challenge for both developed and underdeveloped countries (Kabeyi and Olanrewaju, 2022). Fossil fuels dominate the global energy consumption, accounting for around 80% of consumed energy in total (Ahmad and Zhang, 2020). The most dominant fossil fuels, including coal, natural gas, and oil, are estimated to be exhausted in the near future (Holechek *et al.*, 2022). When fossil fuels are burnt, greenhouse gases (GHG) such as nitrous oxide, sulfur dioxide, carbon dioxide, methane, and fluoro-based gases are emitted (Li *et al.*, 2021a). Greenhouse gas emissions are harmful to humans and the existence of the ecosystem, and cause global warming and climate change. This has attracted significant attention for venturing into other clean sources of energy that are low-cost, renewable, and have lower greenhouse gas emissions, such as hydro, wind, biomass, and solar energy (Gul *et al.*, 2023).

Among the mentioned sources of renewable energy, solar energy has been widely accepted as the most reliable owing to its exceptional benefits, such as global availability and low cost (Dambhare *et al.*, 2021). Electricity is generated from solar energy using solar cells through the photovoltaic (PV) effect (Dambhare *et al.*, 2021; Vodapally and Ali, 2022). Various solar photovoltaic technologies have been employed to generate electricity from solar energy. These solar photovoltaic technologies are grouped into four diverse generations, namely; first, second, third, and fourth (Pastuszak and Węgierek, 2022). These generations are further classified depending on the materials employed for solar cell manufacturing (see Figure 1.1).
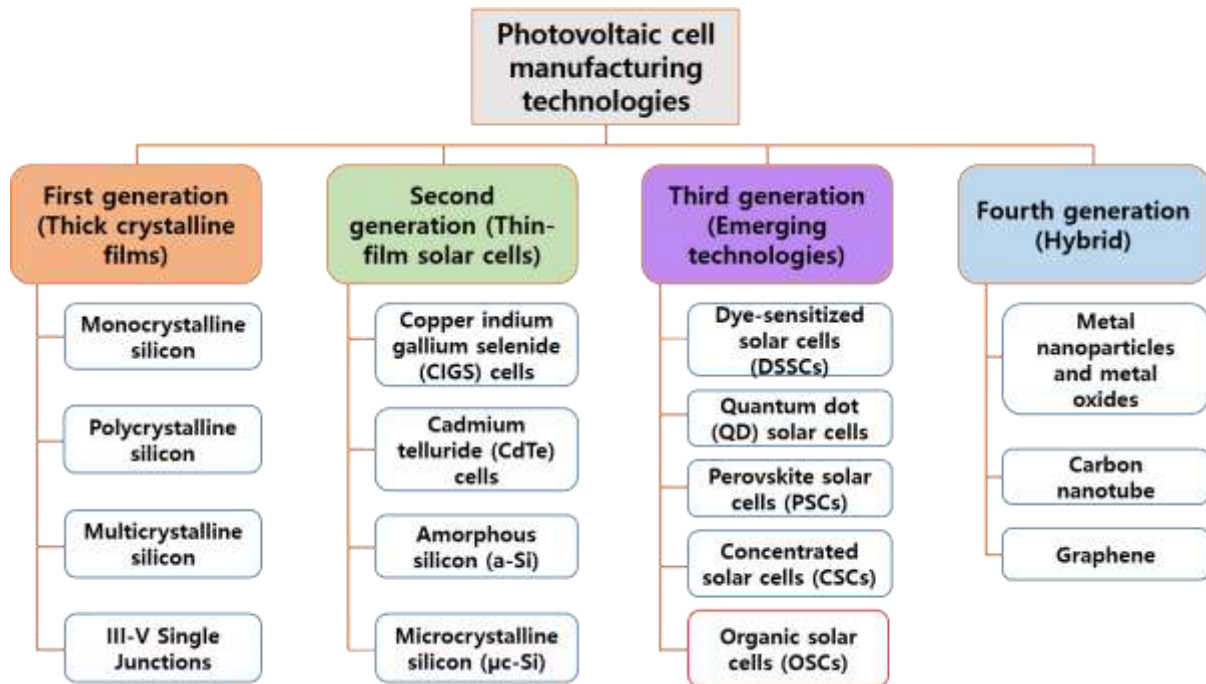
Figure 1.1: Four classifications of solar photovoltaic technology, which fall under first, second, third, and fourth generations (Adapted from: Dambhare *et al.*, 2021; Pastuszak and Węgierek, 2022).

The most prevalent solar photovoltaic technology is the first-generation, which comprises monocrystalline/single and polycrystalline silicon solar devices (Rathore *et al.*, 2021). The popularity of first-generation solar cells is ascribed to their high power conversion efficiencies (Figure 1.2), small bandgaps, and long lifetimes of over 25 years (Pastuszak and Węgierek, 2022).
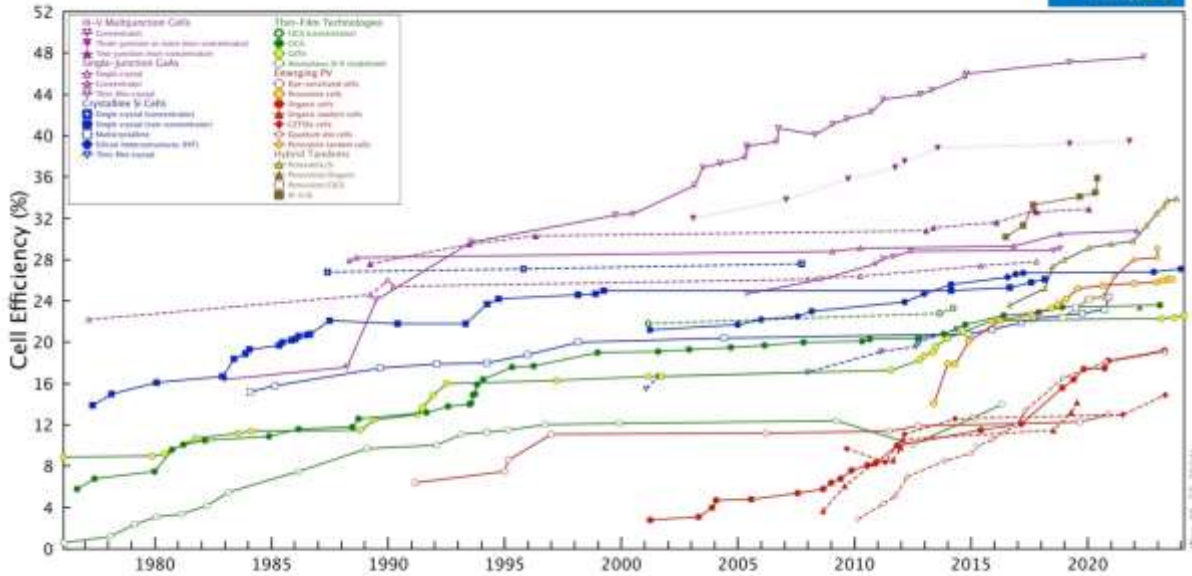
Figure 1.2: Top solar cell efficiencies of various solar photovoltaic technologies per the National Renewable Energy Laboratory (NREL) reports (NREL, 2024).

First-generation solar cells face the limitations of high manufacturing costs, high operational energy requirements, prolonged energy return periods, and the requirement to use pure silicon with a decent crystal structure (Sampaio and González, 2017). Second-generation technologies have been applied to overcome the limitations of first-generation technologies. Unlike first-generation materials, second-generation materials have been reported to have an inexpensive installation process, increased flexibility, high efficiency of ~12%, and long lifetime of ~25 years (Mundo-Hernández *et al.*, 2014). The second-generation materials have limitations of light and moisture degradation, toxicity, scarcity, and larger bandgaps that restrict photon utilisation in solar cells (Avrutin *et al.*, 2011; Dhere, 2006; El Chaar *et al.*, 2011; Hosenuzzaman *et al.*, 2015).

Third-generation technologies, specifically organic solar cells (OSCs), have the potential to replace first-generation solar cell technologies. This is due to their excellent characteristics, which include low production costs, flexibility, large-scale production, semitransparency, and lightweight (Chen *et al.*, 2023; Duan and Uddin, 2020). Generally, OSCs are defined as those whose photoactive or absorbing layer is composed solely of organic semiconductors that form

3

an electron donor (D) and an electron acceptor (A) (D-A) configuration. The donor materials are either polymers or small molecules (Solak and Irmak, 2023), while the acceptors can constitute small molecules, fullerenes, polymers, and non-fullerenes (NFAs) (Ganesamoorthy *et al.*, 2017). These OSCs fall into four major groups, depending on the arrangement of the photoactive layer material (Solak and Irmak, 2023), as shown in Figure 1.3. The single-layered OSC type consists of a blend of D and A materials in one layer placed between top and bottom electrodes. In the bilayer type, the photoactive layer has two layers, one with the D material and the other with the A material. The third type is the bulk heterojunction (BHJ), formed by an interpenetrating network of D- and A-blended materials. The last type is called tandem OSC, which consists of two or more subcells separated by a junction within one OSC structure. These types of OSCs are further classified as conventional or inverted (Li *et al.*, 2020), subject to the positioning of the top or bottom electrodes as well as the buffer layers (see Figure 1.3).
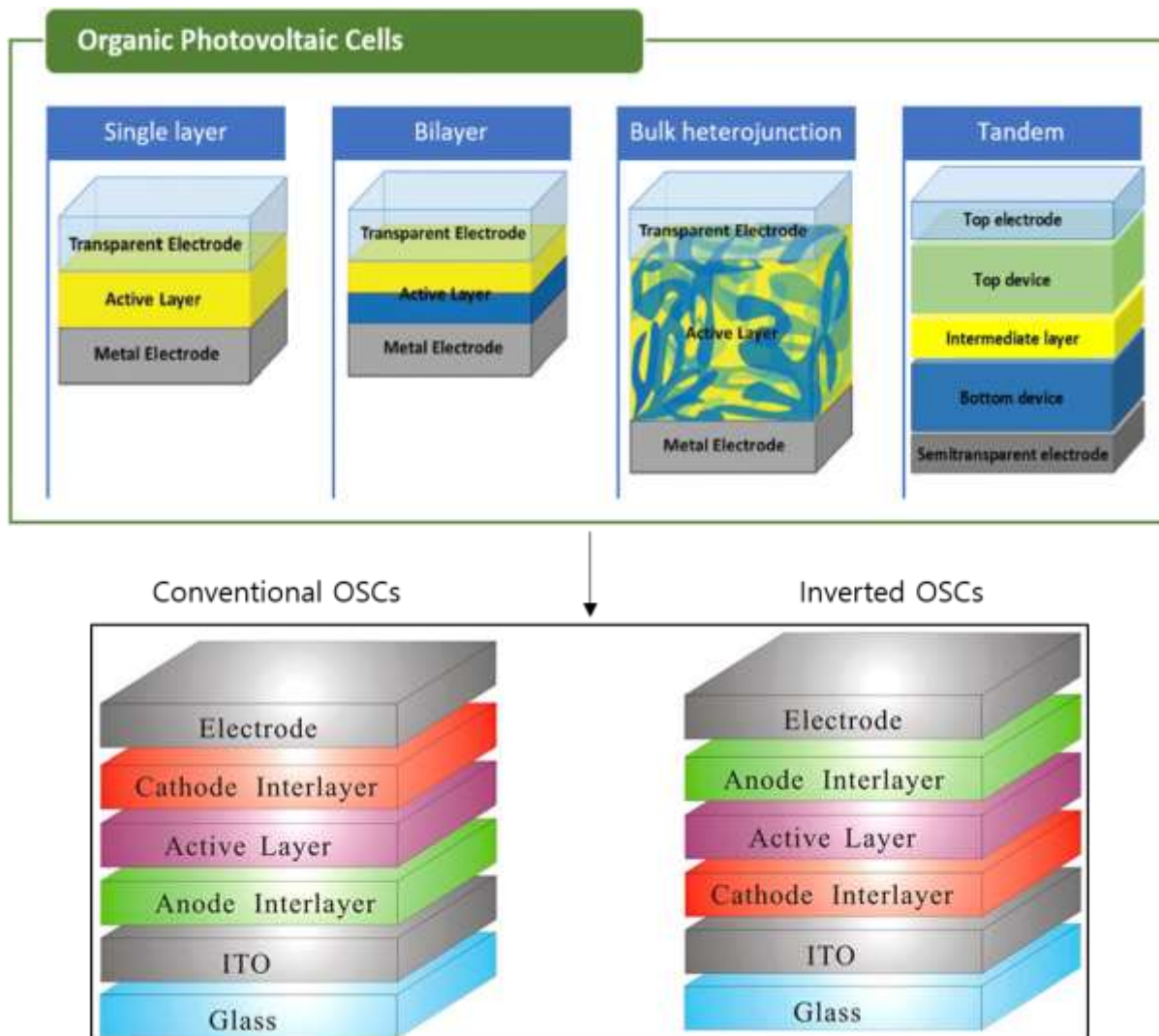
Figure 1.3: Types of OSCs based on the arrangement of the active layer materials and positioning of various OSC layers (Adapted from: Li *et al.*, 2020; Solak and Irmak, 2023).

Among the OSCs developed to date, those with non-fullerenes as the acceptors have shown a substantial improvement in power conversion efficiency (PCE) (Figure 1.4), with a record PCE of >19% for single-junction-based devices and >20% for tandem-junction-based devices, respectively (Jin *et al.*, 2023).
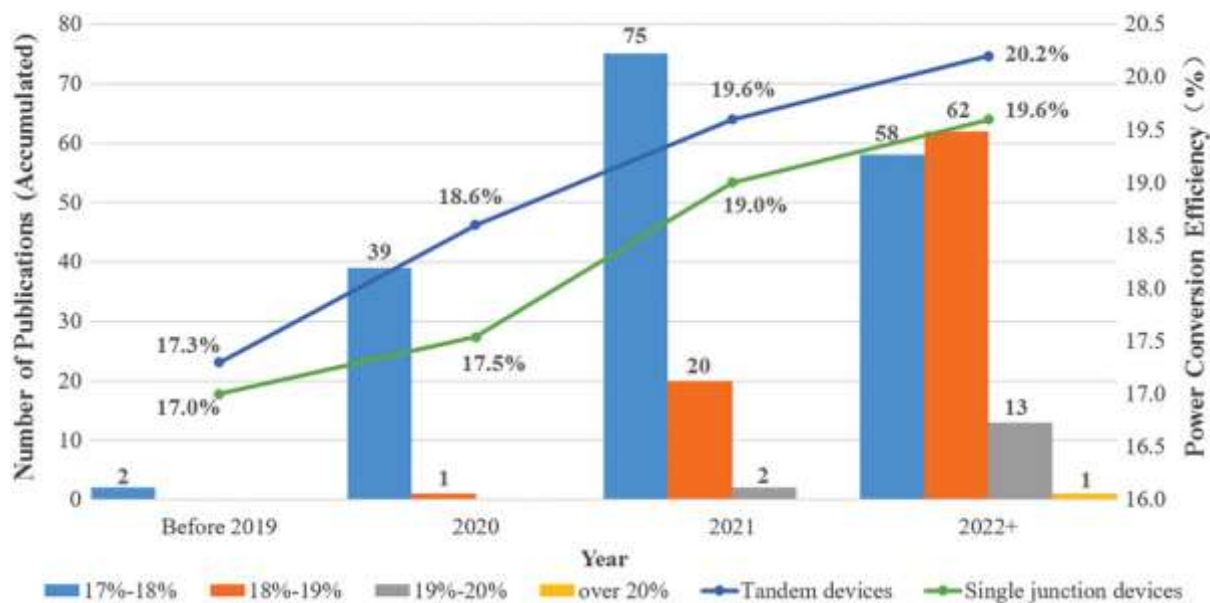
Figure 1.4: Record power conversion efficiencies of NFA-based OSCs attained recently in single junction and tandem devices (Jin *et al.*, 2023).

This top performance of NFA-based OSCs has been reached by implementing various strategies, as shown in Figure 1.5.
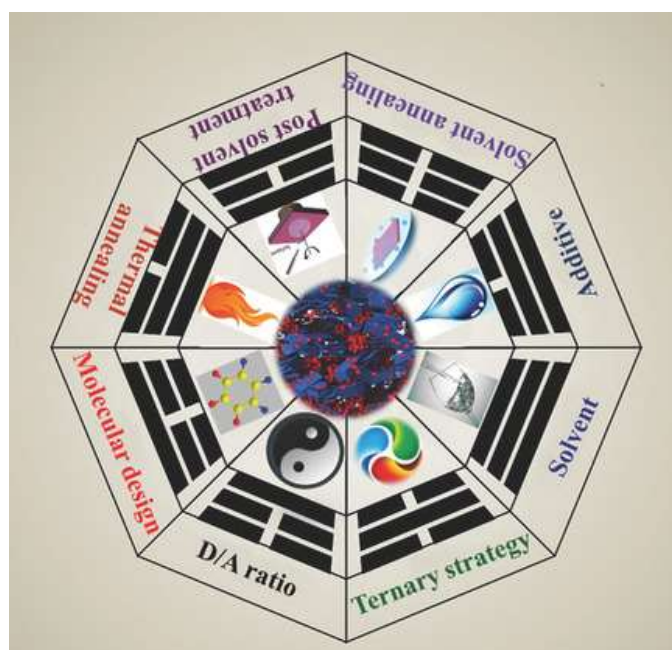
Figure 1.5: Different strategies adopted to realise high performance in NFA-based OSCs (Zhao *et al.*, 2018).

Despite this good achievement in the performance efficiencies of OSCs, their practical and commercial applications are yet to be realised owing to instability issues (Xu *et al.*, 2021). Usually, the instability of OSCs is caused by a number of factors (Figure 1.6) which include metastable morphology, light, heat, oxygen, moisture, mechanical stress, diffusion of electrodes to the photoactive layer, and unstable buffer interlayers (Xu *et al.*, 2021).
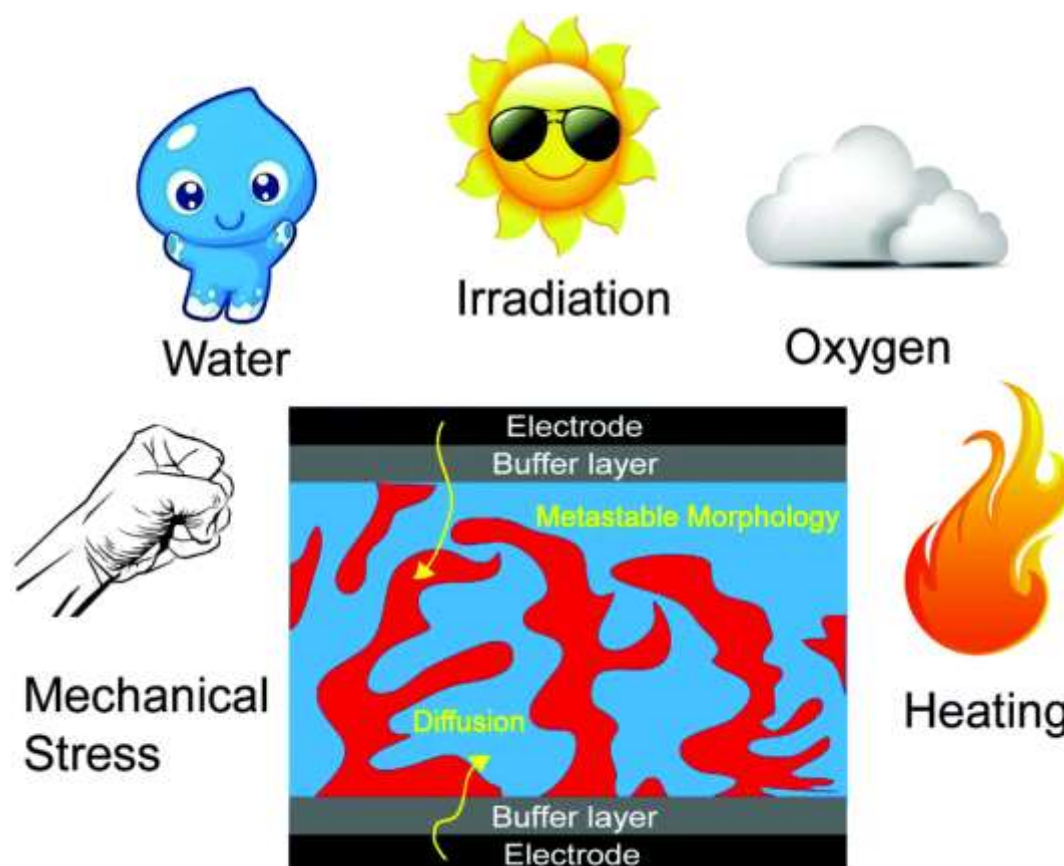
Figure 1.6: A schematic demonstration of the factors that hinder the stability of OSCs (Cheng and Zhan, 2016; Duan and Uddin, 2020).

Efforts have been made to address these instability causes, with major investigations based on morphology optimisation (An *et al.*, 2023a; An *et al.*, 2023b; Chang *et al.*, 2020) as well as encapsulation strategies (Planes *et al.*, 2020), which have led to significant contributions to OSCs' stability. Less effort has been devoted to the interfacial or buffer layers, which also constitute the causes of the OSCs' instability. In this regard, this study sought to improve the stability of OSCs by modifying the buffer layer, specifically the electron transport layer (ETL).

1.2 Statement of the Problem

In inverted OSCs, zinc oxide (ZnO) as well as tin (IV) oxide (SnO$_2$) are commonly employed as electron transport layers. This is because of their promising features such as high electron mobility, high optical transparency, easy solution processability, low cost, and flexible energy levels (Di Mario *et al.*, 2023a; Kong *et al.*, 2021; Liang *et al.*, 2015; Liu *et al.*, 2021). Nonetheless, the photocatalytic nature, surface defects, and inorganic and brittle nature of metal oxides result in interfacial instability when used in OSCs. Therefore, it is essential to solve the interfacial instability issue arising from the use of metal oxides so as to realise stable OSCs. This study sought to address the interfacial instability problem by modifying zinc oxide and tin (IV) oxide surfaces with ultraviolet (UV)-curable organic resins.

1.3 Objectives of the Study

1.3.1 General Objective

The general objective of this work was to enhance the performance and the stability of OSCs by modifying the ETL (zinc oxide and tin (IV) oxide) with ultraviolet-curable resins.

1.3.2 Specific Objectives

The specific objectives of this work were as follows:

1. To optimise zinc oxide/ultraviolet-curable resins and tin (IV) oxide ETLs.
2. To determine the properties of zinc oxide, tin (IV) oxide, and ultraviolet-curable resins.
3. To investigate the effect of modifying zinc oxide and tin (IV) oxide with ultraviolet-curable resins on the interfacial characteristics.
4. To characterise PM6:Y6-BO-based OSCs with zinc oxide and tin (IV) oxide electron transport layers modified with ultraviolet-curable resins.
5. To study the stability of PM6:Y6-BO-based OSCs with zinc oxide and tin (IV) oxide electron transport layers modified with ultraviolet-curable resins.

1.4 Justification and Significance of the Study

Substantial effort have been put on various approaches to make OSCs more stable. Although progress has been made in bridging the gap between the performance and stability of OSCs, a threshold for commercial viability has yet to be realised. Therefore, a stability gap exists in attaining the commercial applicability of solar cells. Metal oxides, which are commonly employed as ETL materials in OSCs, have surface defects and suffer from a photocatalytic effect that decomposes the photoactive layer upon ultraviolet light illumination. Owing to their inorganic nature, they form a poor ETL/organic photoactive layer interfacial contact. All of these factors cumulatively limit the performance along with the stability of OSCs. Therefore, there is a need to develop possible solutions to the problems that arise when metal oxides are used as electron transport materials. This study addresses these problems by modifying zinc oxide and tin (IV) oxide electron transport materials with cheap and commercially available ultraviolet resins.

The coating industry commonly uses ultraviolet curable resins to enhance the properties of furniture, such as increasing durability and resistance to scratches and chemicals. Ultraviolet resins have the advantage of containing chemical groups that can be quickly cross-linked under a low ultraviolet lamp power, making their processing affordable and straightforward. This chemical resistivity of ultraviolet resins can help reduce the chemical reactivity of zinc oxide and tin (IV) oxide. The rapid cross-linking technology of ultraviolet resins is expected to anchor them onto the metal oxide surface, creating a robust and durable interfacial layer. Moreover, the organic form of ultraviolet resins can prevent the mismatched inorganic/organic contact (ETL/photoactive layer) in OSCs, acting as a barrier. Considering these properties, ultraviolet resins are a suitable choice and have the potential to be used as surface modification materials of zinc oxide and tin (IV) oxide in this study. Therefore, this study provides a practical approach to applying ultraviolet resins as electron transport interlayer materials, which can increase the performance and stability of OSCs.

CHAPTER TWO: LITERATURE REVIEW

2.1 Historical Evolution of OSCs

Organic photovoltaics were first discovered in the 1950s, with various organic materials, such as dyes and similar compounds, being applied as photoactive layer materials (Spanggaard and Krebs, 2004). In the 1980s, the application of polymers materials as absorbers in photovoltaic cells was realised (Spanggaard and Krebs, 2004). Unfortunately, photovoltaic cells based on polymers and dyes yielded very low PCE of < 0.1%. A breakthrough in organic photovoltaics was realised after PCE ~1% was achieved using a dye molecule (Tang, 1986) and the D-A concept with polymer-polymer, polymer-dye, polymer-fullerene, and dye-dye organic materials (Spanggaard and Krebs, 2004).

Polymer-fullerenes have been extensively investigated owing to the discovery of fullerenes with excellent electron affinities (He and Li, 2011). Fullerenes have been studied for many decades, leading to their highest efficiency of 12.1% in 2017 (Kumari *et al.*, 2017). Although fullerenes have gained considerable attention as electron acceptors in OSCs, their limited flexibility, high synthesis costs, limited stability, and weak photoabsorption (Li *et al.*, 2022a) limit their further applications and discoveries toward realising the theoretically predicted PCE limit (Shockley and Queisser, 1961).

These limitations of fullerene-based electron acceptors have transpired into non-fullerene electron acceptor NFAs. Unlike fullerene electron acceptors, NFAs exhibit superior optical absorption, flexible energy levels, and bandgaps, low cost of material synthesis, and improved stability (Gertsen *et al.*, 2020; Luo *et al.*, 2022; Zhang *et al.*, 2023). The development of high-efficiency NFA-based OSCs began in 2015 (Armin *et al.*, 2021). However, the first-ever NFA-based OSC outperformed fullerene-based OSCs in 2017 (Zhao *et al.*, 2017). Since this discovery, NFA-based OSCs have been progressively developed, achieving over 20% efficiency (Zheng *et al.*, 2022).

2.2 Commercialisation of Organic Solar Cells

Currently, OSC devices have demonstrated PCEs over 20%, reaching the commercialisation threshold. However, problems associated with these high-performance OSCs hinder their commercial viability. First, the majority of high-performance OSCs realised so far are fabricated by using solvents like chlorobenzene and chloroform, which are halogenated and hazardous, thus posing an environmental threat (Xue *et al.*, 2018). Secondly, high PCEs in OSCs have been realised in small-area devices. For commercial viability, OSC photoactive materials must exhibit significant thickness-tolerant photovoltaic characteristics (Xue *et al.*, 2018). Additionally, the high manufacturing costs of photoactive materials resulting from detailed and expensive synthetic procedures limit the cost-effectiveness of OSCs (Xue *et al.*, 2018). Finally, insufficient OSC lifetime remains a critical factor that limits the industrial realisation of high-performance OSCs (Mateker and McGehee, 2017; Zhang *et al.*, 2019a; Zhang *et al.*, 2018).

2.3 Organic Solar Cell Instability Mechanisms

Under normal working conditions, photoactive materials of OSCs suffer degradation caused by internal and external factors. Internally, the metastable morphology, diffusion of the electrodes, and charge transfer layer materials towards the photoactive layers result in OSC degradation (Duan and Uddin, 2020). One reported cause of the unstable morphology in OSCs is the incompatibility between the D and A molecules (Zhang *et al.*, 2019a), which results in poor phase separation. Franke *et al.* (2008) reported the possibility of hole transport layer materials diffusing to the photoactive layer in tandem OSC devices, resulting in photocurrent and voltage drop. Additionally, evidence of photocurrent loss in OSCs due to diffusion of the electrode (aluminum (Al)) into the charge transport layer was reported by Voroshazi *et al.* (2015).

In outdoor applications, exposing OSCs to heat, light, oxygen, moisture, and mechanical stress is unavoidable. Light illumination and oxygen and moisture permeation can oxidise photoactive layer materials, electrodes, and charge transport layers (Duan and Uddin, 2020). The light/photooxidation of photoactive layer materials can lead to variations in the molecular structures of the D and A materials, thus misaligning the energy levels, which results in PCE loss (Aygül *et al.*, 2013). Ambient air can oxidise low work-function electrodes (calcium (Ca)

11

and Al) into metal oxides (Glatthaar *et al.*, 2007). The formed metal oxides provide electrical insulation, thus hindering the process of charge transport and extraction in OSCs. Heating is a thermodynamic process that can trigger the evolution of OSC morphology. A change of the active layer morphology can result in a polarity mismatch with the charge transport layers, thereby creating a charge extraction barrier (Duan *et al.*, 2019). Finally, mechanical stress is unavoidable during the transportation and installation of the OSC devices. This stress may result in cracks and punctures within the OSC device layers, making them prone to moisture and water ingress, causing degradation (Juillard *et al.*, 2018).

2.4 Cumulative Approaches to OSCs Stability Enhancement

In recent times, improving the stability of OSCs has become a top priority for commercial applications (Li *et al.*, 2023a). Generally, stability enhancement strategies are classified into four major categories, as shown in Figure 2.1. Significant effort has been put to enhancing the stability by optimising the photoactive layer. However, apart from the photoactive layer, charge transport layers, especially the electron transport layer, which forms an interface with the photoactive layer, play a critical role in the interfacial stability of inverted OSCs (iOSCs) (Li *et al.*, 2023a).
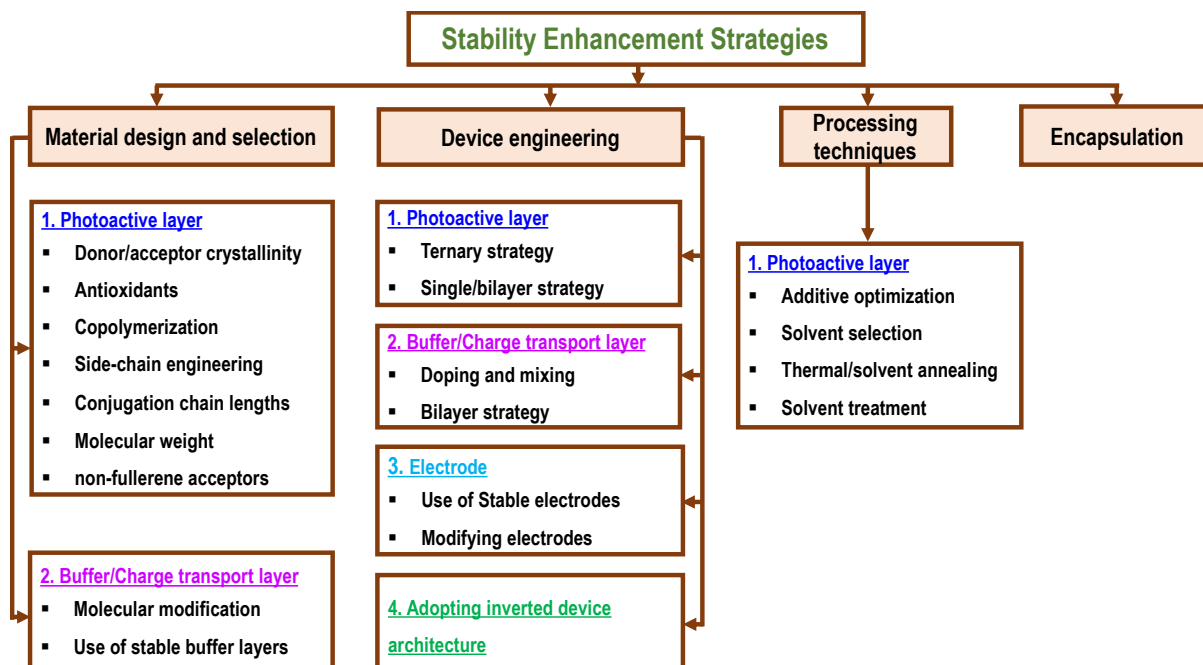
Figure 2.1: Schematic illustration of the approaches which have been employed to enhance the stability of OSCs (Adapted from: Cheng and Zhan, 2016; Duan and Uddin, 2020).

2.5 ETL/Photoactive Layer Interfacial Instability in Inverted Organic Solar Cells (iOSCs)

In iOSCs, the widely used ETL materials are tin (IV) oxide (SnO_2) and zinc oxide (ZnO) (Di Mario *et al.*, 2023a; Swami *et al.*, 2023). This is because ZnO possesses good features, such as high charge mobility, transparency, tunable energy level, and a simple solution processing procedure (Liu *et al.*, 2021). Similarly, SnO_2 exhibits outstanding features such as, tunable energy level, high charge mobility, high optical transparency, good chemical stability, and higher resistance to ultraviolet (UV) light (Di Mario *et al.*, 2023a). However, various stability problems arise when ZnO and SnO_2 ETLs are used in iOSCs.

First, ZnO obtained from solution processing has surface defects, such as hydroxyl groups and oxygen vacancies (Yang and Yu, 2023), which act as charge recombination centres. The recombination centres are sensitive to atmospheric conditions, such as moisture and oxygen, which are detrimental to the stability of OSC devices (Yang and Yu, 2023). Another limitation of using ZnO in OSCs is that it is brittle and inorganic in nature. Thus, it forms poor physical interface with the organic absorber, which results in OSC device instability (Cai *et al.*, 2021). Notably, ZnO is better known for its photocatalytic activity subject to UV light irradiation, and it decomposes the non-fullerene acceptors in iOSCs, resulting in a photostability problem (Jiang *et al.*, 2019; Soultati *et al.*, 2020).

On the other hand, SnO_2 has a broader bandgap and lower UV light sensitivity, making it less photocatalytic (Jiang *et al.*, 2019) than ZnO. SnO_2 is also inorganic, when used as ETL in OSCs, it forms a mismatched physical interface with the organic photoactive layer (Kong *et al.*, 2021). In addition, SnO_2 processed by solution methods has mass surface defects, which are disadvantageous to the iOSCs' stability (Kong *et al.*, 2021).

2.6 Review of Interfacial Stability Enhancement Studies

Surface passivation or the modification of ZnO or SnO_2 ETLs is beneficial for augmenting the iOSCs' stability (Xu *et al.*, 2021). In recent times, Li *et al.* (2022b) modified ZnO ETL with a naphthalene diimide derivative organic molecule in NFA iOSCs based on a D18:N3 photoactive layer blend processed in chloroform solvent by using 1, 8 diiodooctane (DIO) as solvent additive. The modified ETL layer was thermally treated at 120 °C after deposition. This modification suppressed the photocatalytic effect and reduced the mass defects on the surface of ZnO, resulting in a performance improvement from 16.64% to 18.20%. Notably, a high

photostability of T_{80} (time required for the efficiency to drop to 80% of its original value) for more than five years was obtained for the D18:N3 based iOSC with the ZnO-modified ETL under I-sun (100 mW cm^{-2}) irradiation simulated by a white light-emitting diode (LED). Su *et al.* (2022) used functionalised graphene oxide-based nanosheets to modify the ZnO ETL in a PM6:Y6 blend system processed from chloroform (CF) solvent with a chloronaphthalene (CN) additive. This modification resulted in a PCE improvement from 14.5% to 16.5%. In addition, the thermal stability of iOSCs based on the modified ZnO ETL at 65 °C inside a glovebox was T_{80}=2712 hours (h) compared to T_{80}=240 h of iOSCs based on the pristine ZnO ETL. Similarly, it was found that graphene oxide-based nanosheets scavenged reactive radicals on ZnO, mitigating its photocatalytic activity. This improved the photostability under one sun irradiation simulated by an LED from 220 h to 2000 h.

Macromolecular organic compounds called calixarenes were utilised to modify the ZnO ETL in PM6:L8-BO based iOSCs processed in chloroform solvent with a DIO additive (Li *et al.*, 2020). The modification layer of calixarenes was deposited on ZnO through spin-coating and thermally treated at 180 °C for 20 min. This organic passivation interlayer improved the PCE from 17.14% to 18.25%, with improved thermal and photostability. The iOSCs based on plain ZnO attained T_{80}=200 h, while iOSCs based on modified ZnO attained T_{90}=200 h after thermal stress inside a glovebox at 85 °C. Similarly, the iOSCs based on pristine ZnO decayed to 80% of their original PCE after 160 h of continuous 1-sun irradiation provided by the LED. Conversely, iOSCs based on the modified ZnO ETL exhibited T_{80}=480 h. Modification of the ZnO ETL to enhance air stability was also investigated. For instance, Yang and Yu (2023) modified ZnO ETL with caffeic acid in iOSCs based on PM6:L8-BO BHJ which was processed using chlorobenzene (Cb) solvent and DIO solvent additive, and improved the PCE from 16.41% to 18.2%. Notably, this modification reduced the polarity of ZnO and mitigated its surface defects. As a result, iOSCs based on pristine ZnO lost 50% of their PCE after 840 h of exposure to ambient atmosphere. In contrast, iOSCs based on modified ZnO lost 25% of their PCE after the same exposure time and conditions.

In addition to the use of organic compounds to modify ZnO, inorganic materials have also been used to stabilise iOSCs. Lan *et al.* (2023) used atomic layer deposited (ALD) aluminum oxide (Al$_2$O$_3$) to modify the ZnO ETL in iOSCs based on a PM6:Y6-BO blend in chloroform solvent with a DIO additive. This Al$_2$O$_3$ was deposited at 200 °C substrate and chamber temperature.

14

After modification, the performance of the iOSCs increased from 15.63% to 16.61%. The air stability of iOSCs based on modified ZnO at 40% relative humidity was improved after 500 h of exposure compared to that with unmodified ZnO.

The surface modification approach has also been utilised to stabilise iOSCs based on the SnO_2 ETL as well as improve their performance. An anthraquinone derivative was used to passivate the SnO_2 surface in iOSCs based on a PM6: BTP-eC9 blend processed from chloroform with a DIO additive (Yu *et al.*, 2022). The PCE of iOSCs increased from 15.6% to 17.7% after anthraquinone modification. Light stability was also investigated under continuous illumination for 370 h. The iOSCs based on modified SnO_2 retained 59.3% of their PCE, whereas iOSCs based on unmodified SnO_2 retained 13.7% of their PCE. Zhang *et al.* (2021) blended SnO_2 with cobalt metal ions (Co^{2+}) and used it as an ETL in iOSCs based on a PM6:Y6 blend processed from chloroform solvent with chloronaphthalene additive. The iOSCs with the SnO_2:Co^{2+} ETL presented a higher PCE of 15.3%, compared to the 15.1% PCE of iOSCs based on the plain SnO_2 ETL. Notably, the photostability of iOSCs based on the SnO_2:Co^{2+} ETL was improved as opposed to the iOSCs based on the SnO_2-only ETL under both LED and UV light illumination.

A stability study reported by Peng *et al.* (2020) utilised quantum dots (InP/ZnP) to mitigate the SnO_2 ETL surface defects in iOSCs based on a PM6:Y6 blend processed from chloroform solvent with a chloronaphthalene additive. This passivation strategy resulted in a performance enhancement from 13.86% to 15.22%. Interestingly, this bilayer ETL comprising SnO_2/InP/ZnP resulted in a T_{80}=500 h, which was even higher than the T_{80}=100 h of the normal OSCs processed using PEDOT: PSS. The performance and storage stability of iOSCs based on a PM6:Y6 blend processed from chloroform with chloronaphthalene as the additive were investigated by employing SnO_2 modified with dimethylaminoethyl methacrylate (Fu *et al.*, 2021). The performance of the iOSCs was improved from 13.08% to 15.45% by the SnO_2 ETL modification. The OSC devices with modified SnO_2 ETL lost 5% PCE after 960 h, while devices based on the pristine SnO_2 ETL lost 15% PCE after the same time.

From the above-reviewed literature reports, it is evident that a research gap exists between the employed stability enhancement strategies and the required fulfilment criteria for the commercialisation of OSCs. First, halogenated CF and Cb solvents, which threaten the

environment, were utilised to process the photoactive layers. Second, in some literature reports, the modification materials were processed using high temperatures (>150 °C), which can reduce the ITO substrate conductivity. The thermal stability tests in the literature were mainly undertaken in nitrogen environment with negligible moisture and oxygen. It is anticipated that in a nitrogen environment, solar cell devices will exhibit minimal decay in PCE. In addition, the photostability tests reported in the literature mostly use LED as the light source. LEDs have a lower solar irradiance in the ultraviolet region than metal halide lamps, resulting in spectral irradiance equivalence problems. The limitations of these approaches in the literature motivated our research study, which focused on the thermal and photo stabilisation of green solvent-processed iOSCs by electron transport layer modification. Specifically, ZnO and SnO_2 ETLs were modified using room-temperature-processed cross-linkable ultraviolet-curable resins in PM6:Y6-BO-based OSCs. It is noteworthy that the use of ultraviolet-curable resins as modification materials for ETL in OSCs has been applied for the first time.

CHAPTER THREE: THEORETICAL FRAMEWORK

3.1 Photovoltaic Effect in OSCs

The mechanism of operation of OSCs can be scaled down into four significant steps, as illustrated in Figure 3.1 (Sun *et al.*, 2023). The first step involves absorption of light by the organic absorber (D-A) materials to generate excitons (Mohamed El Amine *et al.*, 2023). These excitons diffuse through the D and A phases to the D/A interface, dissociating into free charges (holes and electrons). The electrons are transferred through the A phase, lowest unoccupied molecular orbital (LUMO) level, ETL/A interface to the cathode. On the other hand, free holes are transported via the D phase, highest occupied molecular orbital (HOMO) level, HTL/D interface to the anode completing the circuit (Mohamed El Amine *et al.*, 2023). This results in the generation of a photocurrent.
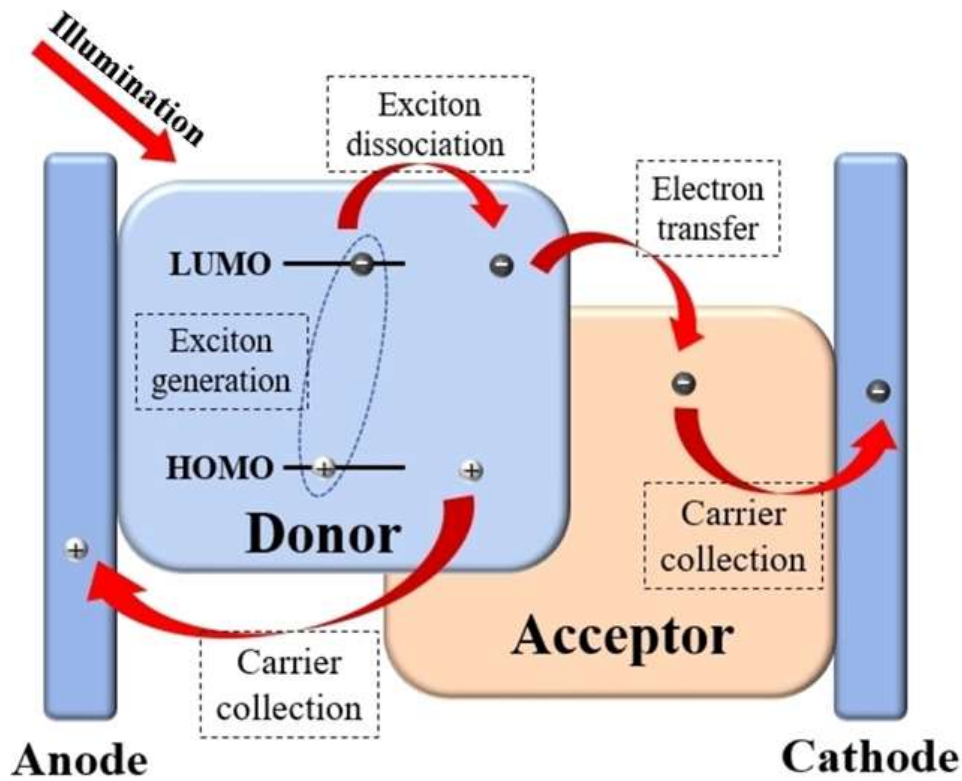
Figure 3.1: Representation diagram of the four-step working operation of OSCs (Sun *et al.*, 2023).

3.2 Photovoltaic Performance Measurement in OSCs

Three photovoltaic parameters, namely Voltage (V_{oc}), current density (J_{sc}), and fill factor (FF), are used in analysing the OSCs (Sun *et al.*, 2023). The subscripts sc and oc refer to short and open circuits, respectively. J_{sc} refers to the operating current in the OSCs when the output voltage is zero, whereas V_{oc} refers to the output voltage in the OSCs when the output current is zero. The loss due to resistance during OSCs' operation is referred to as FF and is given by Equation (3.1).

$$FF = \frac{J_M \times V_M}{V_{OC} \times J_{SC}} = \frac{P_M}{V_{OC} \times J_{SC}} \tag{3.1}$$

Here, J_M refer to the current while V_M refer to the voltage obtained at the maximum power (P_M) (see Figure 3.2).
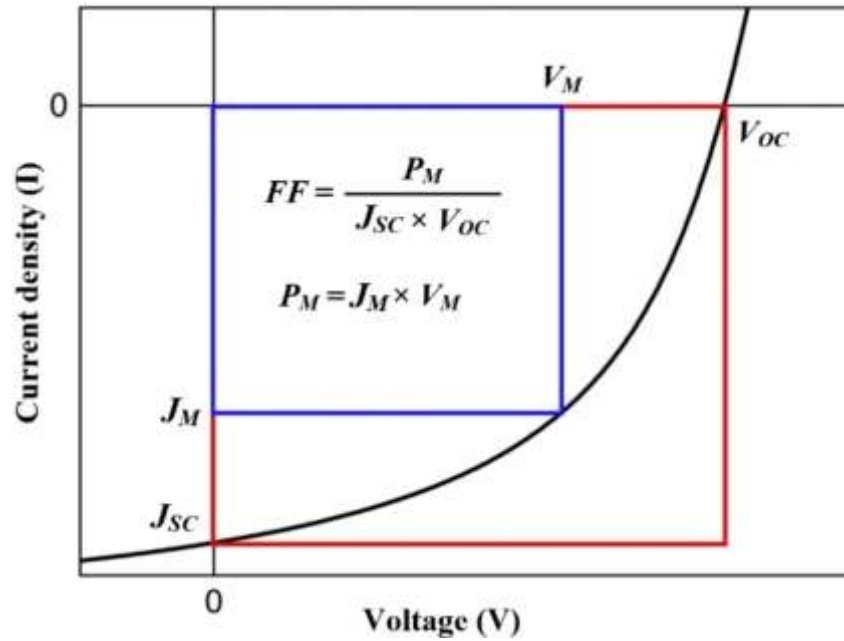
Figure 3.2: A depiction outlining the output J-V parameters of OSCs (Sun *et al.*, 2023).

Equation (3.2) determines the efficiency of OSC devices.

$$\eta = \frac{V_{OC} \times J_{SC} \times FF}{P_{in}} \tag{3.2}$$

18

Where P_{in} refers to the light power incident on the OSC device. The external quantum efficiency (EQE) also characterises OSCs. EQE typically refers to the ratio of extracted electrons (N_e) as a result of a photocurrent to the injected photons (N_p) (Sun *et al.*, 2023), as expressed in Equation (3.3).

$$EQE = \frac{N_e}{N_p} \times 100\% \qquad (3.3)$$

EQE is an essential technique for characterising photovoltaic devices, as it estimates the OSC device bandgap and theoretical integration of J_{sc} under illumination (Almora *et al.*, 2021). Additionally, experimental EQE measurements assess the accuracy of the J-V measurement conditions by comparing the integrated J_{sc} to the J_{sc} obtained during J-V characterisation (Almora *et al.*, 2021).

3.3 Optical Characterisation/Properties of Semiconductor Materials

3.3.1 Ultraviolet-visible (UV-Vis) Spectroscopy

This technique is commonly employed for measuring the transmittance and absorbance of materials. The essential components of the UV-Vis spectrophotometer are depicted in Figure 3.3. The UV-Vis spectrophotometer consists of tungsten and deuterium (D2) lamps, which provide light in the visible and ultraviolet regions, respectively (Rocha *et al.*, 2018). A monochromator filters the broad wavelengths of the light sources into specific wavelengths corresponding to the material type. This filtered light is focused onto the sample, which absorbs, reflects, or transmits light. The photodetector detects the transmitted light beam coupled with several amplifiers to amplify the transmitted light beam signal (Rocha *et al.*, 2018). The photodetector is connected to a computer that processes the amplified transmitted light beam signal and compares it with the incident light beam to output a spectrum (Rocha *et al.*, 2018). The working mechanism of a UV-Vis spectrophotometer relies on the Beer-Lambert law (Rocha *et al.*, 2018), which is mathematically expressed as Equation (3.4).

$$A = \epsilon \times b \times C \qquad (3.4)$$

Where A, ϵ, b, and C represent absorbance, molar absorptivity, optical path length, and concentration respectively. The fraction of electromagnetic radiation or incident light at particular wavelengths passing through a material can be expressed as the transmittance, which

is given by Equation (3.5) (Ramadhani *et al.*, 2019).

$$T = \frac{I}{I_o} \qquad (3.5)$$

Where I and I_o are the transmitted and incident lights, respectively. The transmittance of a material is inversely proportional to its absorbance, and this relationship is expressed in Equation (3.6).

$$A = \log\frac{1}{T} \qquad (3.6)$$
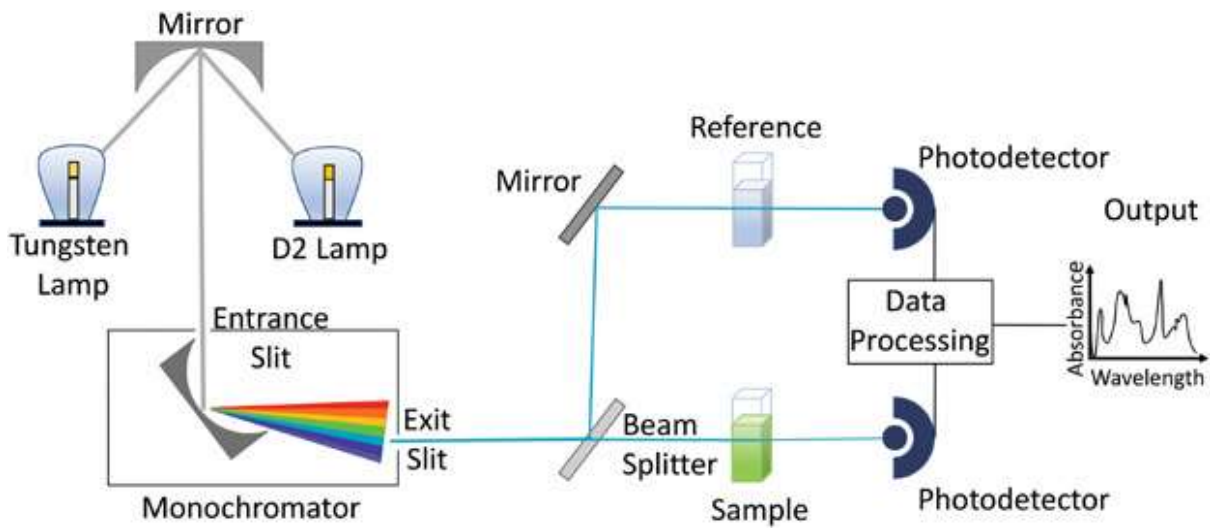
Figure 3.3: An illustration of the working principle of the UV-Vis spectrophotometer (Rocha *et al.*, 2018).

The Tauc model is usually adopted to estimate the optical bandgaps of materials (Tauc *et al.*, 1966). According to the model, the absorption coefficient (α) is related to the photon energy (hν) and bandgap (E_g), as shown in Equation (3.7).

$$(\alpha h\nu)^{\frac{1}{n}} = A(h\nu - E_g) \qquad (3.7)$$

Here, h describes Planck's constant, A refers to the proportionality constant, and n refers to the electronic transition nature, which can be defined in four forms, as illustrated in Table 3.1.

Table 3. 1: Various types of electronic transitions exhibited by different materials (Viezbicke *et al.*, 2015).

Electronic Transitions	n
Direct allowed	1/2
Direct forbidden	3/2
Indirect allowed	2
Indirect forbidden	3

In most cases, the dominant contributors to the absorption process are the allowed transitions. Simply put, Tauc estimation requires the absorbance of a material to be obtained in the energy value range below and above the bandgap transition. Equation (3.7) can be represented in a graph form, as shown in Figure 3.4. The exact bandgap can therefore be estimated by extending the linear portion of the curve in Figure 3.4 to zero absorption coefficient (Viezbicke *et al.*, 2015).
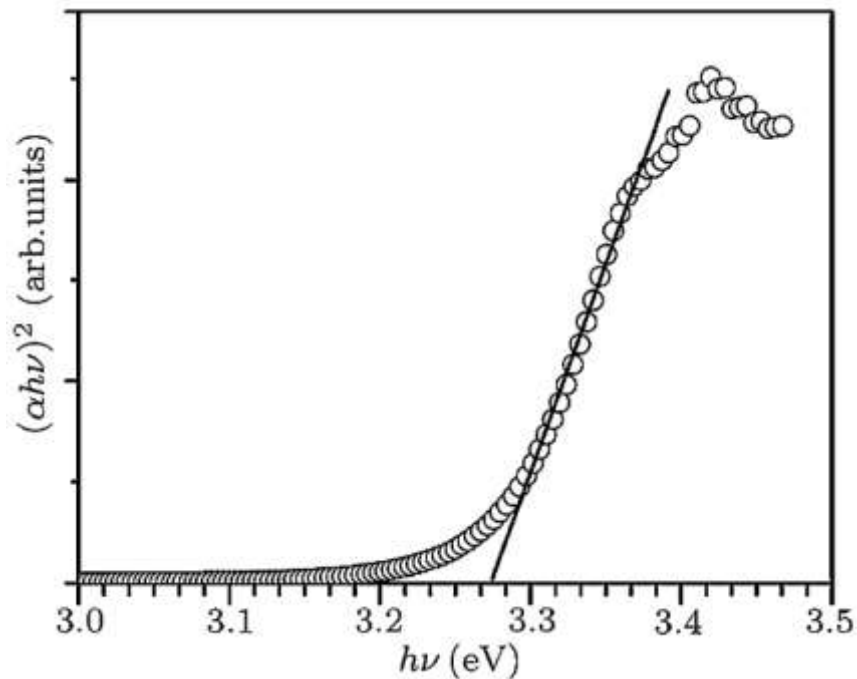
Figure 3.4: Illustration of a Tauc plot showing an extrapolation of the linear part to the x-axis intercept to obtain bandgap (Viezbicke *et al.*, 2015).

3.3.2 Photoluminescence (PL) Spectroscopy

PL spectroscopy is an optical characterisation technique that addresses material interactions with electromagnetic radiation (Alshehawy *et al.*, 2021). This technique can be applied to study the crystal quality, energy band, and structural defects of materials (Divya *et al.*, 2021) by measuring how the fluorescence of molecules varies depending on the wavelength (Alshehawy *et al.*, 2021). A PL spectrometer operates based on the mechanism illustrated in Figure 3.5. The excitation laser beam from the laser source is directed toward the sample through optical lenses. This laser beam excites the electrons in the sample to higher-energy states. The electrons at higher energy excited states then fall to the ground state emitting photons, which the spectrometer detects at particular wavelengths. The spectrometer then separates the emitted photon into its constituent wavelengths, which are then recorded as the spectra of emission intensity versus wavelength (Alshehawy *et al.*, 2021).
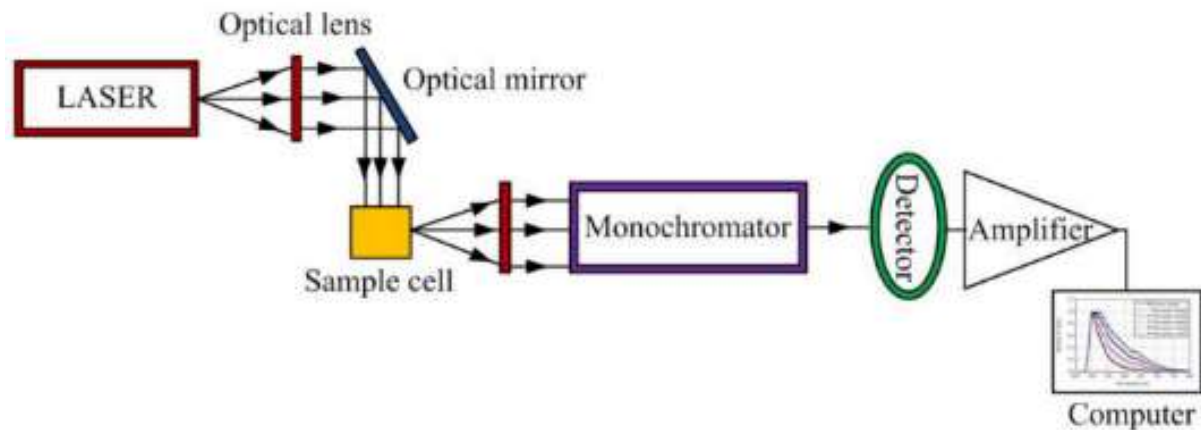
Figure 3.5: Schematic illustration of photoluminescence spectroscopy measurement system (Alshehawy *et al.*, 2021).

3.4 Surface and Structural Characterisation

3.4.1 Contact Angle (θ_C) Measurement

The (θ_C) measurements are used to investigate the surface wettability, adhesion properties, surface energy, and polarity (hydrophobic or hydrophilic) of a surface (Palencia, 2017). There exist three interfacial tensions when a liquid drop is cast on the surface of a solid, namely, liquid-gas (γ_{LG}), solid-gas (γ_{SG}), and solid-liquid (γ_{SL}) (Palencia, 2017). A contact angle is formed at the intersection of the γ_{SL} and γ_{LG} interfaces, as presented in Figure 3.6.
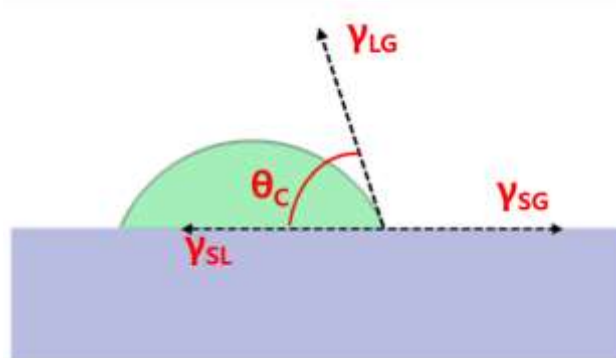
Figure 3.6: An illustration of the liquid drop casted on a surface of the solid with interfacial tensions and contact angle (Palencia, 2017).

When $\theta_C < 90°$, spreading (wettability) of the liquid drop over a large area is favoured, whereas when $\theta_C > 90°$, spreading of the liquid drop is unfavourable (Palencia, 2017). The surface free energy (γ) of a material is a critical factor for studying the interaction of a surface of the solid with other materials. The determination of the γ of a surface of the solid requires that contact angles be obtained using at least two test solvents with dissimilar and known polar components (γ_L^p) and dispersive (nonpolar) (γ_L^d) components. Examples of some commonly used test solvents and their corresponding polar and dispersive γ parts are presented in Table 3.2.

Table 3. 2: Parts of surface energy (γ_l) for different test solvents (Kozbial *et al.*, 2014).

	γ_L (mJm^{-2})	γ_L^p (mJm^{-2})	γ_L^d (mJm^{-2})
Water (W)	72.8	51.0	21.8
Diiodomethane (DIM)	50.8	0.0	50.8
Ethylene glycol (EG)	48.0	19.0	29.0
Glycerol (G)	64.0	30.0	34.0

Several models, including the Youngs, Neumann, Owens−Wendt, and Fowkes (Kozbial *et al.*, 2014; Palencia, 2017) are employed to determine the γ from the experimentally obtained contact angles.

(a) Young's Model

In this model, a mechanical equilibrium of a drop of the liquid on a material surface under interfacial tensions is described by Young's Equation (3.8) (Liber-Kneć and Łagan, 2021).

$$\cos\theta = \frac{\gamma_{SG} - \gamma_{SL}}{\gamma_{LG}} \tag{3.8}$$

However, Equation (3.8) is mechanical and does not consider the chemical aspect of the solid-liquid interaction (Zhang *et al.*, 2019b). The wetting of a surface is designated as a chemo-mechanical occurrence. Therefore, models that consider chemical interactions tend to be more effective and predictive than Young's theory (Zhang *et al.*, 2019b).

(b) Neumann Model

In this model, the θ_C of liquid drop on the surface of a solid is described by Equation (3.9) (Kozbial *et al.*, 2014).

$$\cos\theta = -1 + 2\sqrt{\frac{\gamma_S}{\gamma_L}}\, e^{-\beta(\gamma_S - \gamma_L)^2} \tag{3.9}$$

Here, γ_S and γ_L denote the solids' and liquids' surface energy, whereas β refers to a parameter correlated to the surface of a solid. Rewriting Equation (3.9) results in Equation (3.10) (Kozbial *et al.*, 2014).

$$\ln\left[\gamma_L\left(\frac{1+\cos\theta}{2}\right)^2\right] = -2\beta(\gamma_S - \gamma_L)^2 + \ln(\gamma_S) \tag{3.10}$$

Because γ_L of the solvents used is always known, the left side of Equation (3.10) versus γ_L can be plotted. Therefore, polynomial regression fitting can determine β and γ_S^d from plotted data (Kozbial *et al.*, 2014).

(c) Fowkes Model

This model splits γ_L and γ_S into polar and nonpolar components, as shown below (Kozbial *et al.*, 2014).

$$\frac{\gamma_L(\cos\theta+1)}{2} = \left(\gamma_S^d\right)^{1/2}\left(\gamma_L^d\right)^{1/2} + \left(\gamma_L^p\right)^{1/2}\left(\gamma_S^p\right)^{1/2} \qquad (3.11)$$

Here, $\gamma_S{}^p$ and $\gamma_S{}^d$ refer to the polar and dispersive parts of the solid, respectively. The summation of $\gamma_S{}^p$ and $\gamma_S{}^d$ obtained from Equation (3.11) is assumed to be the total γ_S, which is expressed as Equation (3.12) (Kozbial *et al.*, 2014).

$$\gamma_S = \gamma_S^p + \gamma_S^d \qquad (3.12)$$

(d) Owens-Wendt Model

This model expands the Fowkes Equation (3.12) to construct a geometric mean correlation for γ_{SL} (Zhang *et al.*, 2019b), as illustrated in Equation (3.13).

$$\gamma_{SL} = \gamma_L + \gamma_S - 2\left(\gamma_L^d\gamma_S^d\right)^{\frac{1}{2}} - 2\left(\gamma_L^p\gamma_S^p\right)^{\frac{1}{2}} \qquad (3.13)$$

Replacing Equation (3.13) into Equation (3.8) outputs the Owens-Wendt Equation (3.14) (Kozbial *et al.*, 2014);

$$\frac{\gamma_L(\cos\theta+1)}{2\left(\gamma_L^d\right)^{1/2}} = \left(\gamma_S^d\right)^{1/2} + \left(\gamma_s^p\right)^{1/2}\frac{\left(\gamma_L^p\right)^{1/2}}{\left(\gamma_L^d\right)^{1/2}} \qquad (3.14)$$

The left part of the Owens-Wendt Equation (3.14) can be plotted against $\left(\gamma_L^p\right)^{1/2}/\left(\gamma_L^d\right)^{1/2}$ to obtain a linear curve. The γ_S^d and γ_S^p are then obtained by squaring the y-intercept and the slope of the plot, respectively, after a linear regression (Kozbial *et al.*, 2014; Zhang *et al.*, 2019b).

3.4.2 Atomic Force Microscopy (AFM)

AFM images the surface topography of materials. The AFM operation relies on the attractive and repulsive forces between the material surface and the scanning probe (Müller *et al.*, 2021). The working mechanism of AFM encompasses a raster scan of the cantilever tip, as shown in Figure 3.7. When this tip is scanned over a material surface, it senses its interactive forces with the sample surface, resulting in bending of the cantilever (Pletikapia and Ivoševi Denardis, 2017). The laser light measures the bending reflected by the cantilever to the photodetector. If a cantilever deflection changes, the sample and the tip distance also change, establishing a

constant distance with the feedback loop sandwiched between the tip-sample position unit and a piezoelectric scanner controlled by a computer. Consequently, the cantilever deflection values registered electronically are transformed into a three-dimensional image.
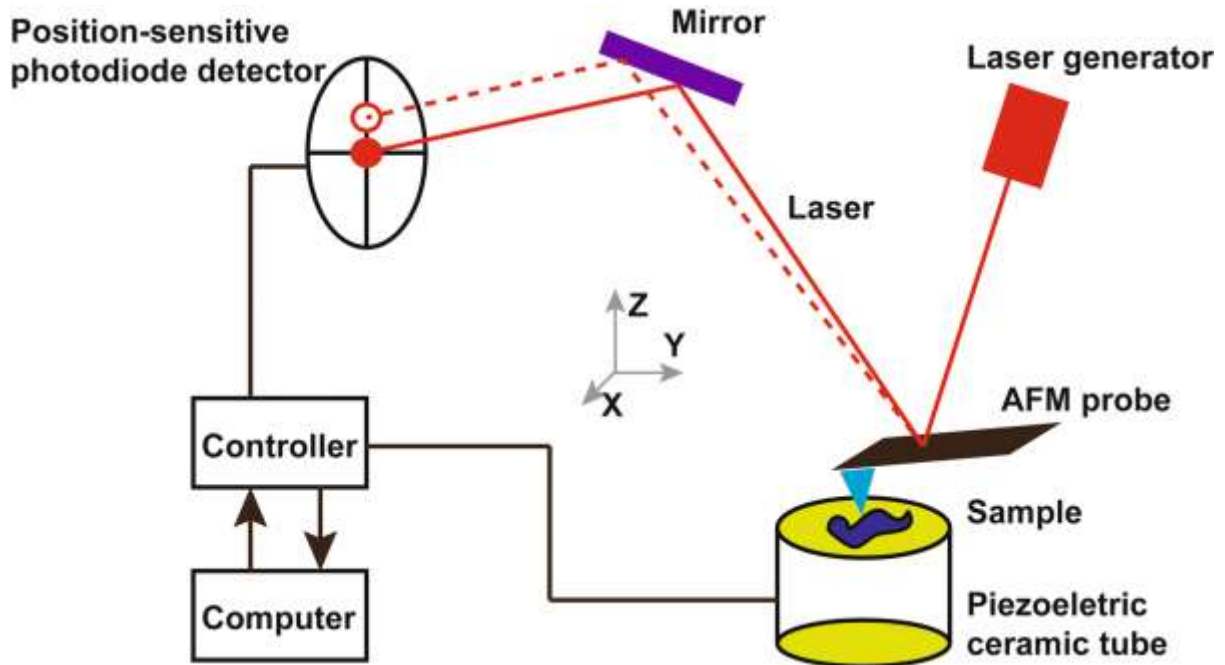
Figure 3.7: An illustration of the operation mode of AFM (Deng *et al.*, 2018).

AFM operation can be grouped into three distinct modes: semi-contact (tapping), contact, and non-contact, as illustrated in Figure 3.8 (Deng *et al.*, 2018).

① Semi-contact Mode

In the tapping mode, the cantilever tip oscillates and touches the sample surface. This mode eradicates the effect of lateral forces and minimises the force produced by the adsorbent layer, outputting a high-resolution image.

② Contact Mode

This mode maintains a slight contact and constant force at the interface of the probe tip and the surface of the sample.

③ Non-contact Mode

The cantilever tip is vibrated continuously on the sample surface without contact. The detector then senses distant forces, for instance, electrostatic/van der Waals, which do not destroy the scanned sample.
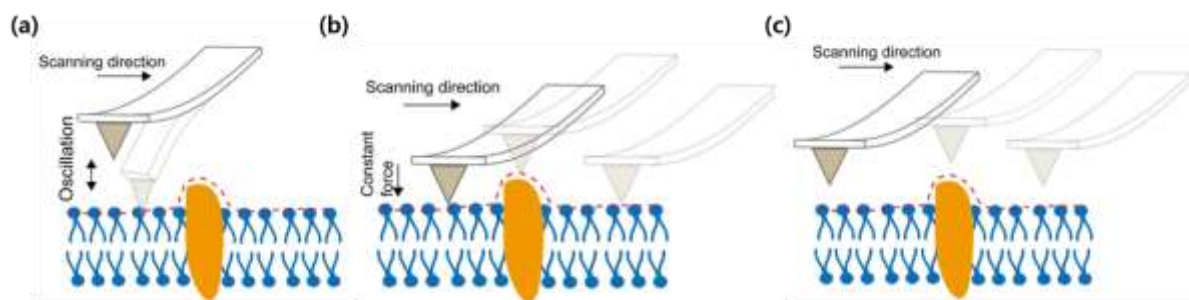
Figure 3.8: The various types of operation modes of atomic force microscope. (a) Tapping (b) Contact and (c) Non-contact (Deng *et al.*, 2018).

3.4.3 Raman Spectroscopy

In this spectroscopy, scientists study the molecules' vibrational modes by analysing the light that is scattered inelastically (Taghizadeh *et al.*, 2020). Raman spectroscopy is usually employed to pinpoint materials via their distinctive vibrational fingerprints. Two classifications of light scattering exist based on the scattering sample size: Rayleigh and Mie (Cho and Ahn, 2020). In the Mie type, even light scattering of entire colours occurs irrespective of the wavelength because of the larger size of the sample molecules compared to the incident light wavelength (Cho and Ahn, 2020). Nonetheless, the Rayleigh type is responsible for the sky blue colour. Rayleigh scattering of most of the light incident on a sample occurs at a wavelength similar to that of the incident light. Nonetheless, some photons undergo scattering inelastically, whereby the wavelength of the scattered light changes. Once Raman scattering (RS) take place, the scattered light wavelength either reduces (Stokes RS) or increases (anti-Stokes RS) (see Figure 3.9).
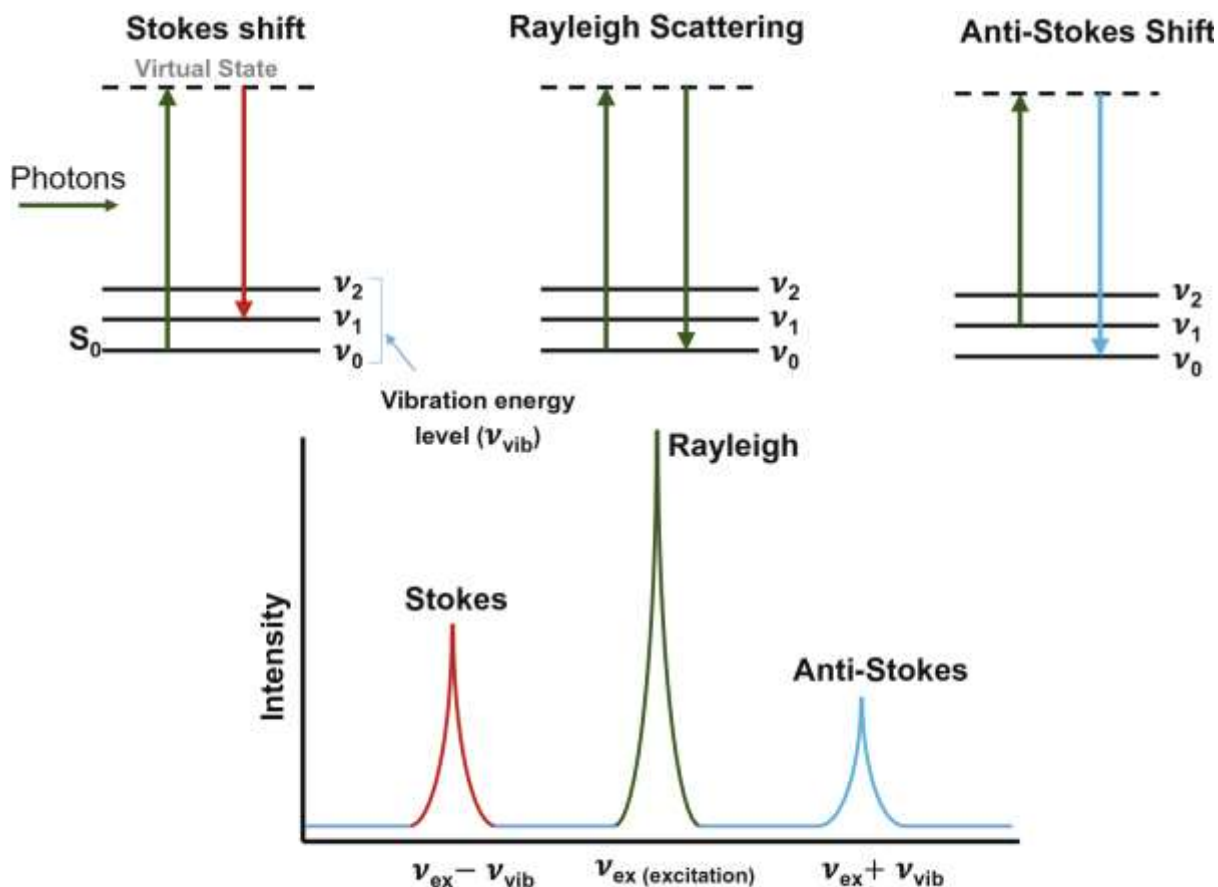
Figure 3.9: An Illustration of different modes of Raman scattering (Cho and Ahn, 2020).

The measurement of Raman spectra follows the steps illustrated in Figure 3.10 (Downes and Elfick, 2010). A laser beam illuminates the sample, emitting the light back. The dichroic mirror filters the emitted light from the wavelength of the laser light. This light is then dispersed and focused by the spectroscope to a 2-dimensional detector, which outputs the Raman spectrum.
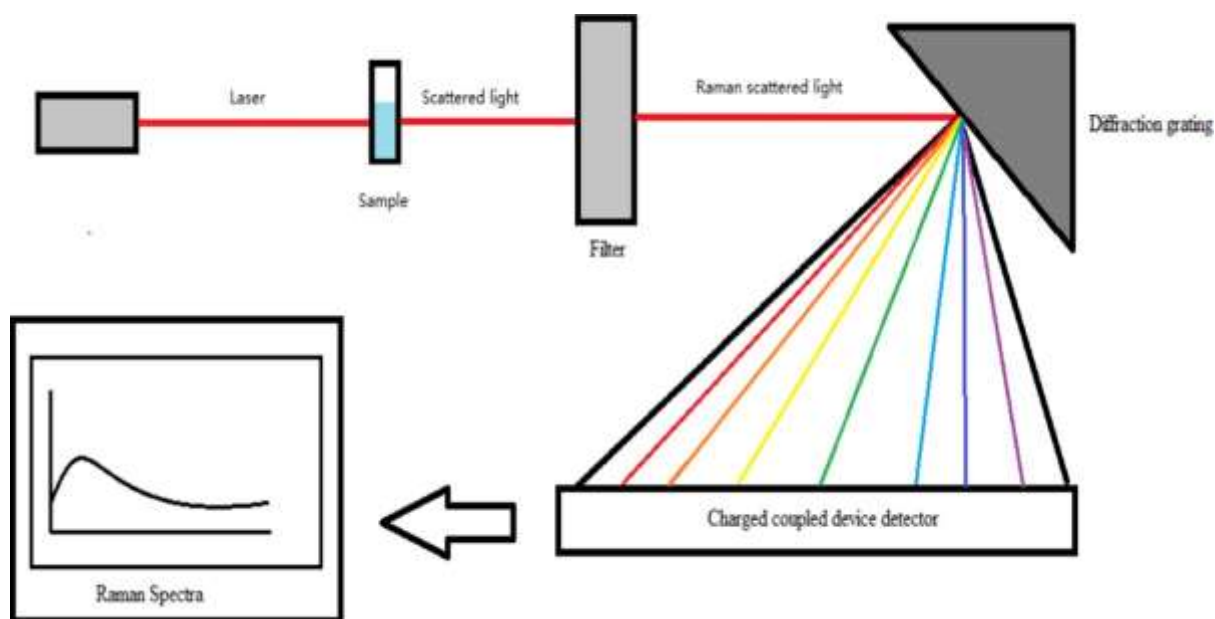
Figure 3.10: An illustration of the operation mode of a Raman spectrophotometer (Lin *et al.*, 2021).

3.4.4 Ultraviolet Photoelectron Spectroscopy (UPS)

The UPS technique is utilised to study the electronic structure of materials (Maheu *et al.*, 2018) and the work function (Φ) on material surfaces (Whitten, 2023). It analyses the kinetic energy of photoelectrons emanated by material surfaces upon illumination with ultraviolet (UV) light (Maheu *et al.*, 2018). When the sample get illuminated with UV light, electrons in the sample become excited and transition to the conduction band (CB) from the valence band (VB). The CB is beyond the vacuum level (E_v). During this electronic transition, some electrons lose energy (termed secondary electrons), whereas others transition elastically. The transitioning electrons together output the UPS spectra (observed spectrum), as illustrated in Figure 3.11 (Whitten, 2023).
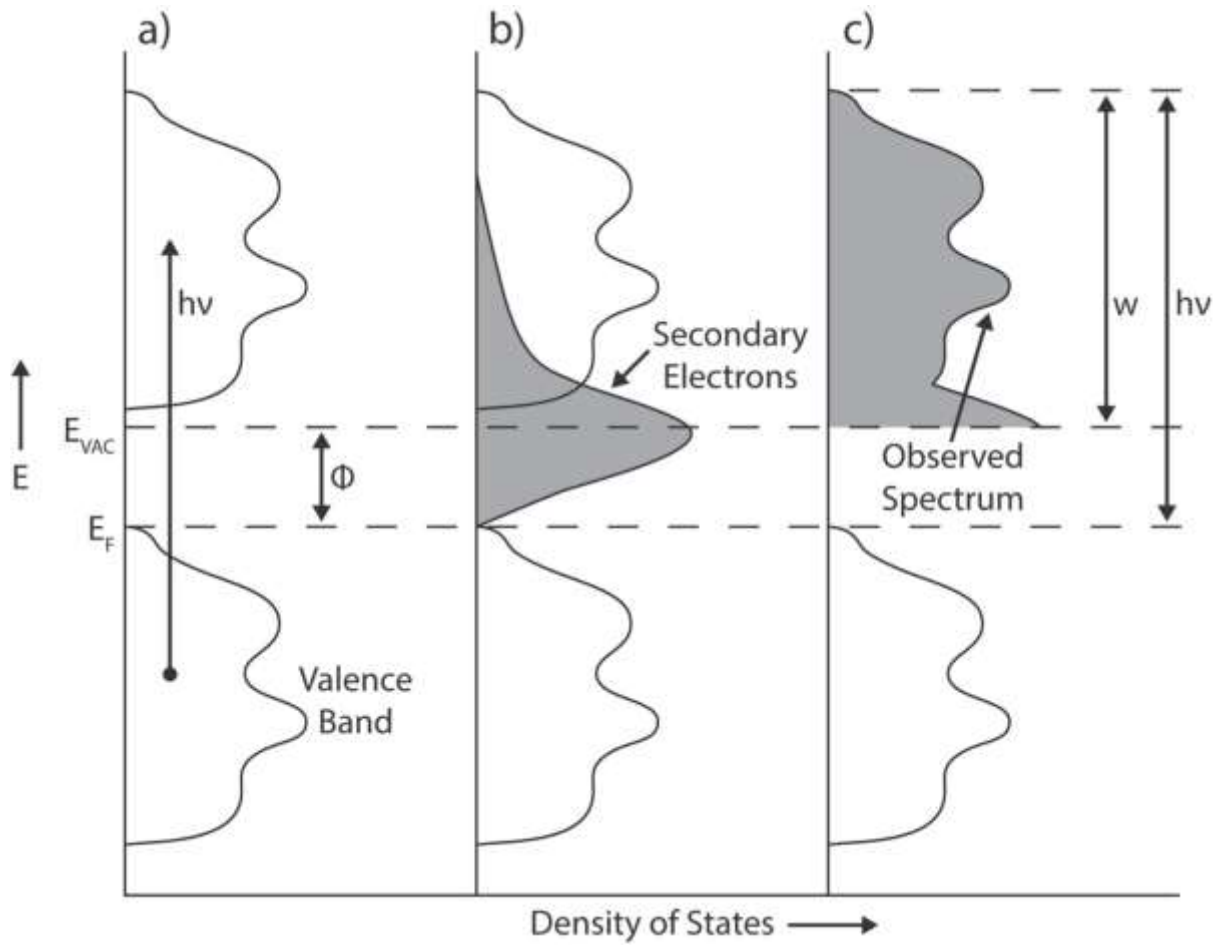
Figure 3.11: Schematic illustration of UPS measurement process (Whitten, 2023). The fermi level of the measurement equipment, the light source's energy, and the output spectrum's width are herein abbreviated as E_F, hv, and w, respectively.

To obtain the (Φ), the cutoff of the secondary electrons (E_{cutoff}) is subtracted from the photon energy of the light source used (Yang and Yu, 2023) as shown in Equation (3.15).

$$\Phi = hv - E_{cutoff} \qquad (3.15)$$

3.4.5 X-ray Photoelectron Spectroscopy (XPS)

This surface characterisation method determines the chemical state and elemental composition (Axnanda *et al.*, 2015). The operation of XPS is centered on the photoelectron effect (Korin *et al.*, 2017), as explained by Anwar *et al.* (2022). A beam of X-rays with energy (hv) is irradiated on the surface of the material under investigation. The penetration of photoelectrons into the

material results in photon absorption, causing core electron (e^-) ionisation/emission in various directions (Anwar *et al.*, 2022). Free electrons with a particular kinetic energy (E_{KE}) are generated through the photoelectric effect and recorded by an electron detector. The energy analyser analyses the recorded e^- to output the XPS spectra, as illustrated in Figure 3.12 (Korin *et al.*, 2017). Every element yields a particular peak in the XPS spectra at a specified binding energy (E_{BE}) value, which helps in determining the electronic structure according to Equation (3.16).

$$E_{BE} = h\nu - E_{KE} - \Phi \tag{3.16}$$

Here, Φ refer to the work function of the investigated material.
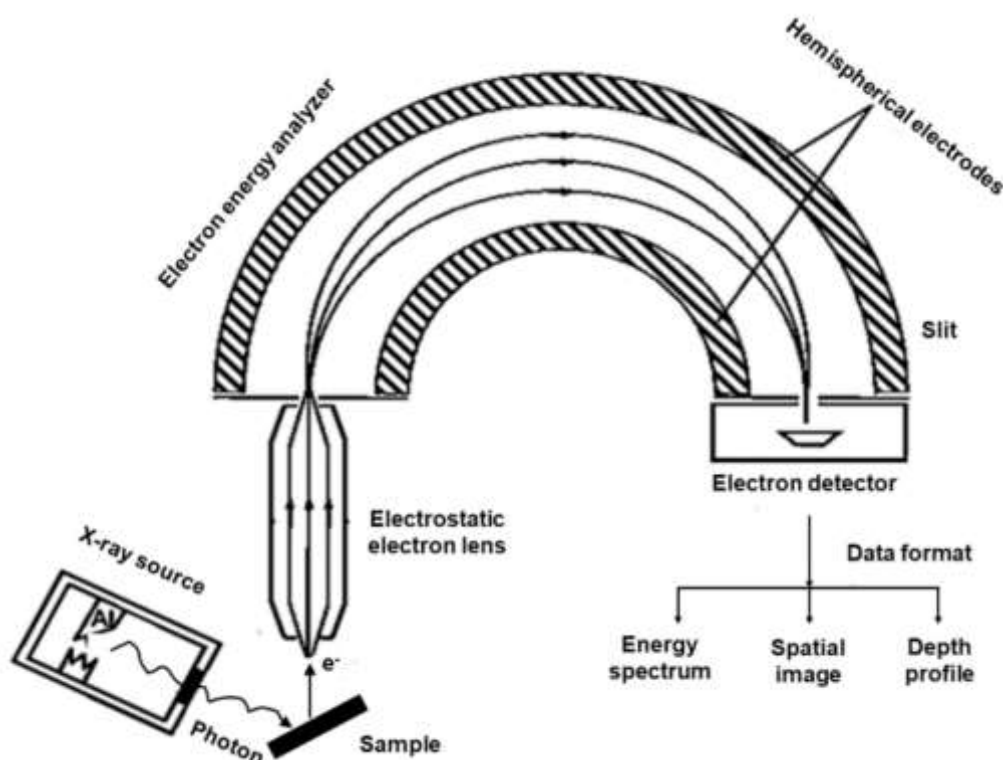
Figure 3.12: The schematic illustration of XPS's essential parts and operation mechanism (Anwar *et al.*, 2022).

3.4.6 Electrochemical Impedance Spectroscopy (EIS)

The degree of opposition to current flow under the voltage applied in electrical circuits is referred to as impedance (Laschuk *et al.*, 2021). Typically, in EIS measurements, a sinusoidal voltage is superimposed on the direct current signal to form an electrochemical scheme,

resulting in an output current density over a wide frequency range (Lazanas and Prodromidis, 2023). Both the applied voltage and output current density share the same frequency, while their amplitudes and phases differ, as shown in Figure 3.13. The fraction of the applied voltage to the output current density estimates the impedance according to Equation (3.17).

$$Z(t) = \frac{E(t)}{j(t)}$$ (3.17)

E (t) and j (t) denote the applied voltage and the output current density, respectively.
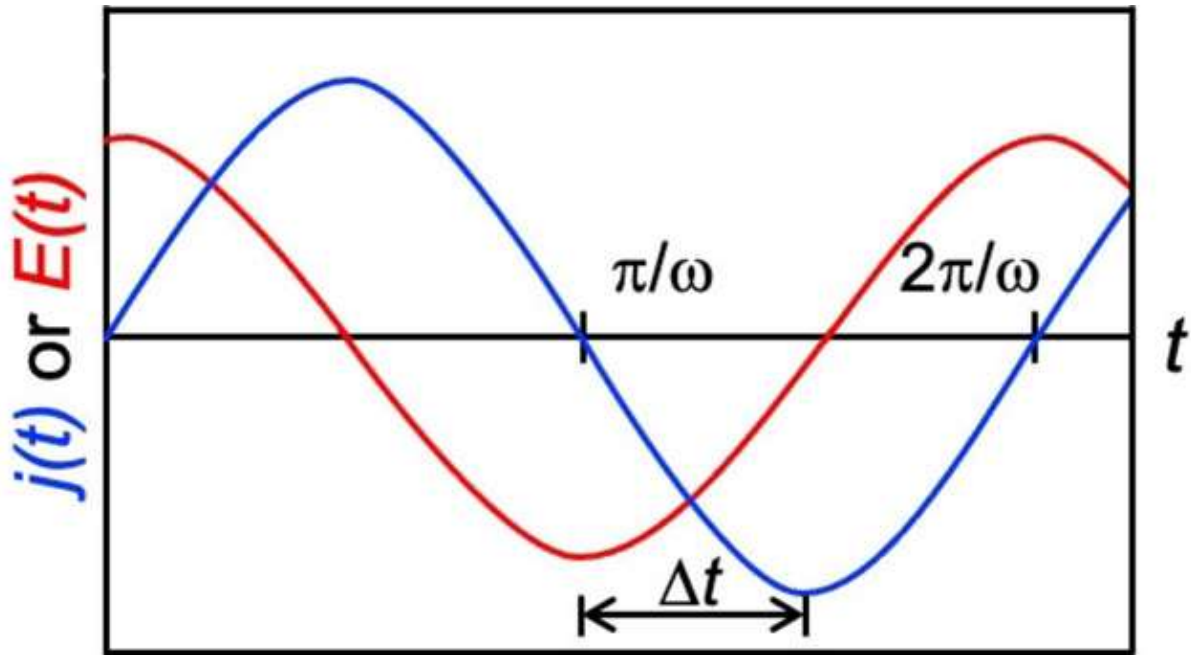
Figure 3.13: Schematic illustration of the correlation between applied voltage (red curve) and the current density (blue curve) (Vadhva *et al.*, 2021). The phase difference between E (t) and j (t) is denoted as **Δ**t.

Significant information is obtained from the measured EIS data through the frequency variation. The data from the EIS measurements can be presented using two plots, Bode and Nyquist, as shown in Figure 3.14. The information obtained from these two plots is complementary and includes the impedance ($Z(\omega)$), imaginary part Im ($Z(\omega)$), and real part Re ($Z(\omega)$) of the impedance (Vadhva *et al.*, 2021). Generally, impedance is a complex term given by the Re ($Z(\omega)$) and Im ($Z(\omega)$) parts, as shown in Equation (3.18).

$$|Z(\omega)| = \sqrt{Im(Z(\omega))^2 + Re(Z(\omega))^2} \qquad (3.18)$$

The angle (ϕ) corresponding to the different E (t) and j (t) phases is given in the Bode plot (Figure 3.14 (c)) and can be related to the Re (Z (ω)) and Im (Z (ω)) impedance parts in accordance with Equation (3.19).

$$\phi(\omega) = \tan^{-1}\frac{Re(Z(\omega))}{Im(Z(\omega))} \qquad (3.19)$$
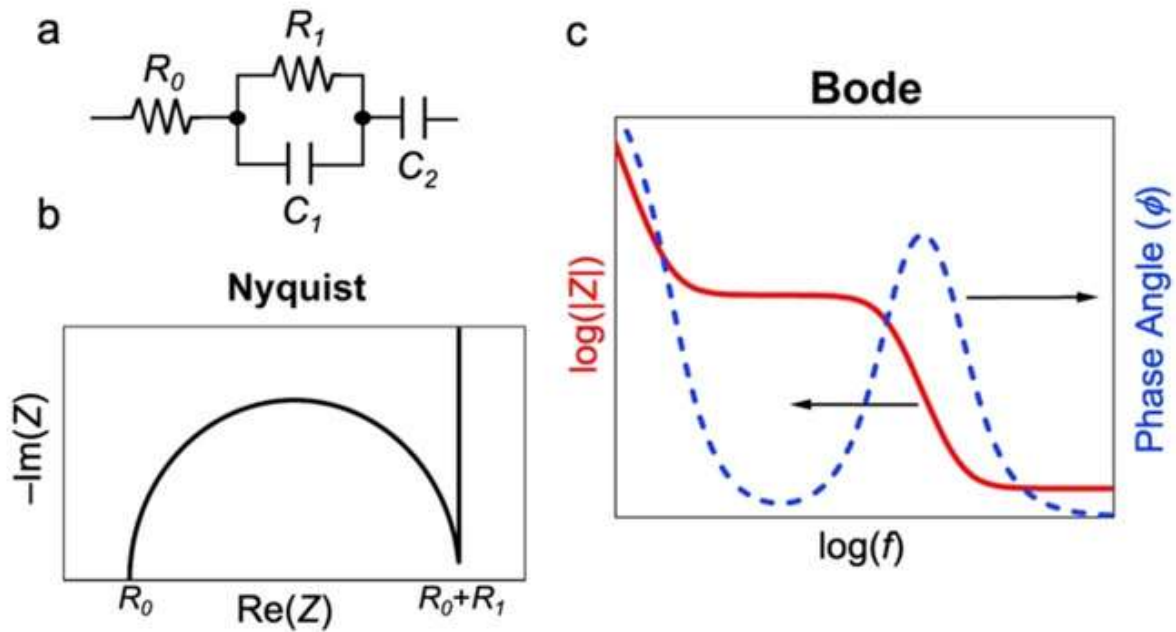
Figure 3.14: A schematic representation of (a) Equivalent circuit model, (b) Nyquist, and (c) Bode plots (Vadhva *et al.*, 2021).

An illustration using the Bode and Nyquist plots can be accomplished by considering an electrochemical system (equivalent circuit model). For example, a circuit comprising of a resistor (R_o) in series connection to a resistor-capacitor (R_1C_1) unit and another capacitor (C_2) is illustrated in Figure 3.14 (a). Furthermore, a Bode plot can provide an EIS data representation on a time scale. Hence, unlike in the Nyquist plot, particular Z (ω) contributions can be correlated to the time constant.

CHAPTER FOUR: MATERIALS AND METHODS

4.1 Materials

In this research, 2-methoxyethanol (2-ME) (CAS No: 109-86-4) and o-xylene (CAS No: 95-47-6) were obtained from Sigma-Aldrich. Ultraviolet (UV) curable resins (SAR and OCS), whose molecular structures are depicted in Figure 4.1, were purchased from the Special Materials Source (SMS) in Korea. The epoxy resin was obtained from NAGASE & Co., Ltd. The PM6 (CAS No: 1802013-83-7) polymer and Y6-BO (CAS No: 2389125-23-7) non-fullerene acceptor, the molecular structures of which are presented in Figure 4.2, were acquired from Brilliant Matters. Molybdenum oxide (MoO_3) (CAS No: 1313-27-5) powder and silver (Ag) beads (CAS No: 7440-22-4) were supplied by ITASCO (Taewon Scientific Co., Ltd). Zinc oxide (ZnO) nanoparticles in butanol and 15% SnO_2 (CAS No: 18282-10-5) in water colloidal dispersion were purchased from Nano Clean Tech and Alfa Aesar, respectively. All chemicals were acquired from their respective companies and used without further purification.
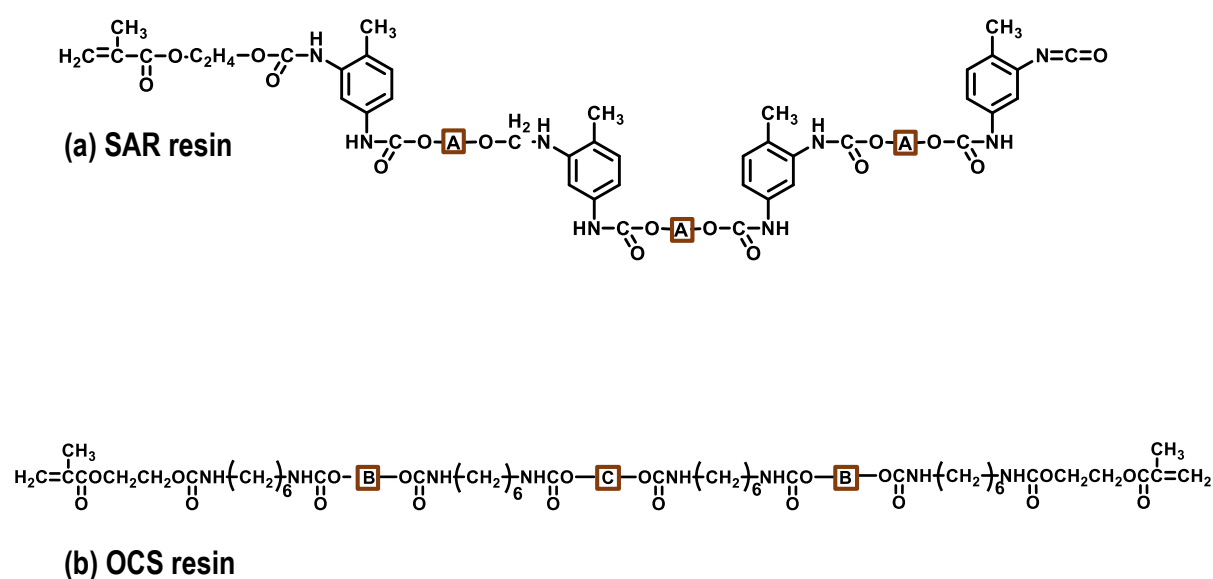
Figure 4.1: The molecular structures of the SAR and OCS resins utilised in this investigation to modify ZnO and SnO_2 ETLs. The squared letters A, B, and C within the molecular structures of ultraviolet resins refer to diols.
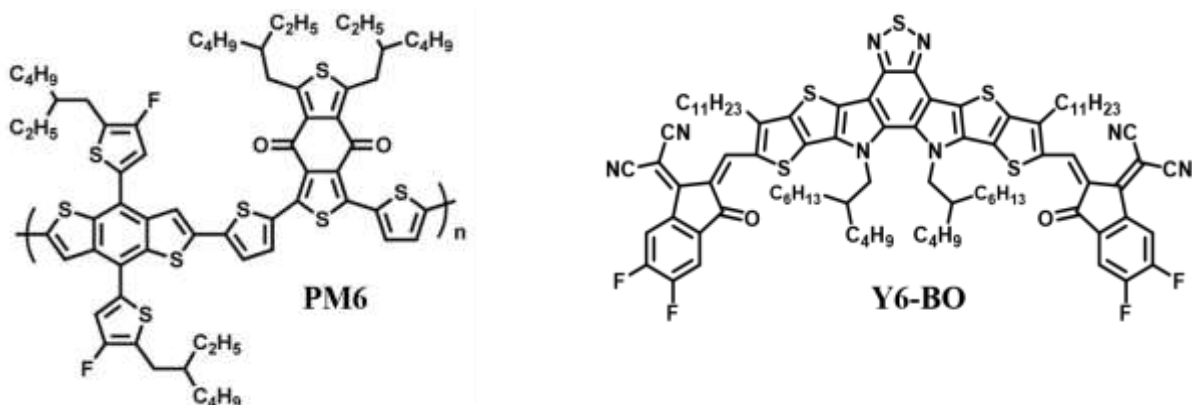
Figure 4.2: Molecular structures of PM6 and Y6-BO photoactive layer materials utilised in this investigation.

4.2 Methods

4.2.1 Substrates Cleansing Procedure

In this study, silicon, plain glass, quartz, and indium tin oxide (ITO) pre-patterned substrates were used for film deposition and OSC device fabrication. All the substrates were cleaned using a standard procedure involving three steps in an ultrasonication bath. First, the substrates were cleaned in soapy deionised water for 25 minutes, then rinsed twice with plain deionised water for 25 minutes each. Second, the substrates were washed in acetone three times for 25 minutes each. Finally, the substrates were cleaned using isopropyl alcohol (IPA) 3 times for 25 minutes each. After cleaning, the substrates were moved to a hot oven and left to dry overnight at $130\,°C$ before use.

4.2.2 Precursor Solution Preparation

Commercial SnO_2 (15% in water colloidal dispersion solution) was diluted six times with water to obtain 1:6 (volume/volume) concentration. The SAR and OCS solutions were obtained by mixing various weights in a 2-methoxyethanol solvent. The active layer solution was made by mixing the PM6:Y6-BO (9.6:11.52 mg) blend in 1 mL of o-xylene solvent and stirring on a magnetic stirrer at 80 °C for at least 3 h before deposition.

4.2.3 Deposition Steps of Electron Transport Layer Films

Before depositing the ETL films, the UV-ozone (UVO) treatment was done on the substrates for at least 15 minutes to remove the organic impurities left during the cleaning steps with organic acetone and IPA solvents to improve the hydrophilicity and enhance clearance.

ZnO and SnO$_2$ electron transport layers were deposited on the substrates from their precursor solutions by one-step spin coating (5000 revolutions per minute (rpm) for 20 seconds and 5000 rpm/40 seconds, respectively) to form the desired thickness. The thermal annealing of the deposited ZnO and SnO$_2$ ETLs was then done on a hot plate at 110 °C and 170 °C, respectively, for 10 minutes each. Modification interlayers of SAR or OCS UV resins were coated on top of ZnO and SnO$_2$ ETLs at 5000 rpm/20 seconds and cross-linked under 365 nm wavelength UV lamp irradiation for 5 minutes and 10 minutes, respectively.

4.2.4 Fabrication of Organic Solar Cells

A 5-µm polytetrafluoroethylene (PTFE) filter was utilised to filter the PM6:Y6-BO precursor solution to eliminate its bulk residue before deposition. In the glovebox, the one-step spin coating of the photoactive layer film (PM6:Y6-BO) on the ITO/ETL/UV resins was carried out at 1800 rpm/17 seconds to achieve the desired thickness, subsequent to pre-annealing at 130 °C for 10 minutes. The photoactive layer film on the ETL was transferred to the thermal evaporation chamber where the HTL (MoO$_3$) (7 nm) and the top electrode (Ag (70 nm)) were deposited by thermal evaporation in a vacuum. Inverted OSCs with the device architecture ITO/ETLs/PM6:Y6-BO/MoO$_3$/Ag were obtained, as presented in Figure 4.3. Glass-on-glass encapsulation was applied to the fabricated OSCs using epoxy resin and cured under UVC (100-280 nm) light before light soaking and thermal stability tests.
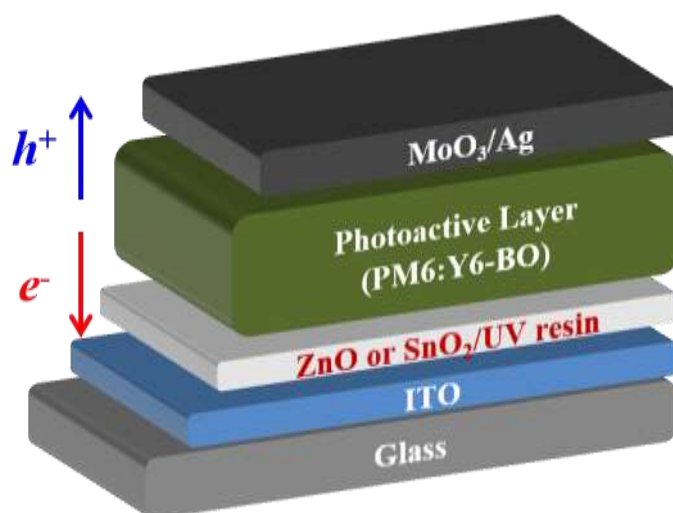
Figure 4.3: A photograph of the device architecture of the OSC device fabricated in this study with different layers.

36

4.3 Characterisation

4.3.1 ETL Film Characterisation

(a) Ultraviolet-visible Spectroscopy

The absorbance of neat ZnO, SAR, SnO_2, and OCS films were determined by use of a Shimadzu UV-2550 UV-visible spectrophotometer (Figure 4.4) in 300 -800 nm wavelength range and the corresponding bandgaps were acquired from the Tauc plot. The same wavelength range applied to determine the absorbance as well as the transmittance of the ZnO and SnO_2 ETLs modified with SAR and OCS resins. The absorbance of pristine PM6, Y6-BO, and the mixture of PM6:Y6-BO on various ETL films was measured in the 300 -1100 nm wavelength range.

Figure 4.4: Photographic illustration of the optical absorption spectra measurement using the UV-visible spectrophotometer connected to a computer.

(b) Solvent Contact Angle (CA) Measurements

The surface wettability of the ETL films was investigated by determining the solvent θ_C in water as well as in DIM using a DSA100 drop shape analyser. The measured water and DIM θ_C on the ETL films were used to calculate the γ according to the Owen–Wendt method (Rudawska and Jacniacka, 2009).

(c) Ultraviolet Photoelectron Spectroscopy

The ionisation potentials and work functions (WFs) of various ETL films were characterised using an ultraviolet photoelectron spectroscopy system (Thermos Scientific K-alpha[+]) with a helium lamp (HeI) 21.22 eV radiation source. The secondary electron cutoffs (E_{cutoff}) of the various ETL films obtained from the UPS equipment were used to calculate the work functions according to the equation WF=21.22 eV-E_{cutoff}.

(d) X-ray Photoelectron Spectroscopy

A K-ALPHA[+] Thermo Scientific system based on the Al Kα source of X-ray was employed to measure the XPS spectra corresponding to the O 1s, Sn 3d, and Zn 2p states in the SnO_2 and ZnO ETLs deposited on silicon substrates before and after modification with the SAR and OCS resins.

(e) Steady-state Photoluminescence Spectroscopy

The PL spectra corresponding to SnO_2 and ZnO ETL films before and after modification on quartz substrates were measured using steady-state PL equipment at 340 nm laser excitation. The PL spectra were obtained in the 300-700 nm wavelength range.

(f) Atomic Force Microscopy

The ETL film morphology was studied using an atomic force microscope in the tapping mode. The ZnO/UV resins and SnO_2/UV resins ETLs for AFM analysis were prepared through spin coating on ITO patterned substrates cut to standard 0.5×0.5 cm sizes. The AFM images of the ETL films obtained from the controlled computer of the AFM machine did not require any further analysis.

(g) Profilometer Measurements

The photoactive layer thickness was determined using KLA-Tencor surface profilometer (see Figure 4.5).

Figure 4.5: Photographic demonstration of Alpha Step-IQ surface profiler measurement system.

4.3.2 OSC Device Characterisation

(a) Photovoltaic Performance

The photovoltaic performance characteristics, comprising J_{sc}, V_{oc}, and FF, were obtained using a computer-controlled LAB50, McScience Solar Simulator under 1-sun (100 mW cm^{-2}) illumination provided by Xenon (Xe) arc lamp at room temperature. The OSC device area was 0.12 cm^2.

(b) EQE Measurements

The EQE and integrated J_{sc} of OSCs with different ETL films were obtained using (K3100 IQX (McScience Inc.) spectral incident photon-to-current efficiency (IPCE) equipment.

(c) Charge Transport

Electron-only devices (ITO/ETL/photoactive layer/SnO$_2$ or ZnO/Ag) were employed to study the charge mobility (μ_e). The J-V curves of electron-only devices measured in the dark are represented as three regions at high bias, intermediate and low bias that are termed child's, trap-filled and ohmic (Fu *et al.*, 2021). The space charge limited current method (SCLC) that used the Mott-Gurney expression $\mu_e = \frac{8Jd^3}{9V^2\varepsilon\varepsilon_o}$ was utilised (Dahlström *et al.*, 2020; Schauer, 2005). Here, J/V^2 refers to the current density vs. voltage slope in the child's region and d refers to the

39

PM6:Y6-BO thickness (100 nm). ε and ε_o refer to the dielectric constant of PM6:Y6-BO (ε=3) material and in vacuum (8.85×10^{-12} Fm^{-1}), respectively.

(d) Trap Density

The trap density (N_{trap}) was also calculated from the electron-only devices according to the equation $N_{trap} = 2V_{TFL}\frac{\varepsilon\varepsilon_o}{qd^2}$. Here, V_{TFL} and q refer to trap-filled voltage and elementary charge, respectively. V_{TFL} is obtained from the juncture between ohmic and trap-filled regions of the measured J-V curves (Fu *et al.*, 2021).

(e) Charge Dissociation

To study the charge dissociation phenomenon in organic solar cells, the photocurrent (J_{ph}) and effective voltage (V_{eff}) (Cai *et al.*, 2023) were computed. Here, J_{ph}=J_L-J_D, where J_L and J_D denote current densities measured under sunlight and darkness, respectively. On the other hand, V_{eff} is obtained as (V_o-V_a), where V_o and V_a denote the voltage at J_{ph}=0 (V_o) and applied bias voltage V_a, respectively. The exciton dissociation probabilities of the organic solar cells were determined by J_{ph}/J_{sat}, where J_{sat} denote the saturated current density (Li *et al.*, 2021b), given by J_{ph} at V_D=0. Where V_D is the voltage in the dark.

(f) Charge Recombination

Recombination of charges in OSCs was investigated using the J_{sc} and V_{oc} versus light intensity (P_{light}) curves. Different light intensity filters ranging between (1–91.6 mW cm^{-2}) were employed to obtain specific J_{sc} and V_{oc} values. The V_{oc}, J_{sc}, and P_{light} relate according to the expressions $V_{oc} \propto n \ln (P_{light})$ and $J_{sc} \propto \alpha \ln P_{light}$ (Cai *et al.*, 2021). Wherein n and α refer to the slopes of V_{oc} and J_{sc} against P_{light}, respectively. These slopes (n and α) were used to estimate trap-assisted recombination and bimolecular recombination, respectively.

(g) Electrochemical Impedance Spectroscopy Measurement

The electrochemical impedance spectra of the OSCs were measured using IVIUM STAT Tech equipment. The EIS spectra were obtained at a 500–500 000 Hz frequency with a bias voltage equivalent to the V_{oc} of the investigated OSCs. Nyquist curves obtained from the EIS were fitted using an equivalent circuit model (ECM) depicted in Figure 4.6 to obtain the series (R_{series}) and surface ($R_{surface}$) resistance in the OSCs.
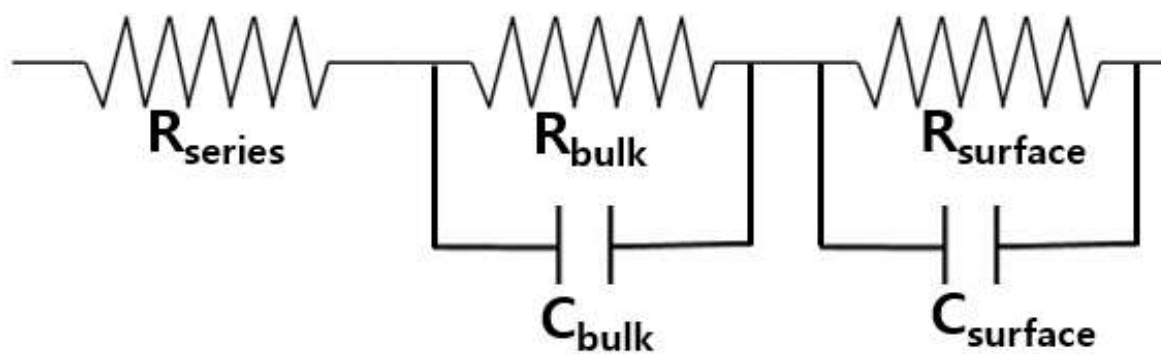
Figure 4.6: The ECM utilised in this investigation for fitting the EIS curves of OSCs.

(h) Stability Measurements

1. UV Stability

The ultraviolet stability of the acceptor (Y6-BO) films coated on different ETL forms was investigated. A UV lamp (365 nm, 8 W) was used to illuminate the Y6-BO/ETL films, as displayed in Figure 4.7.
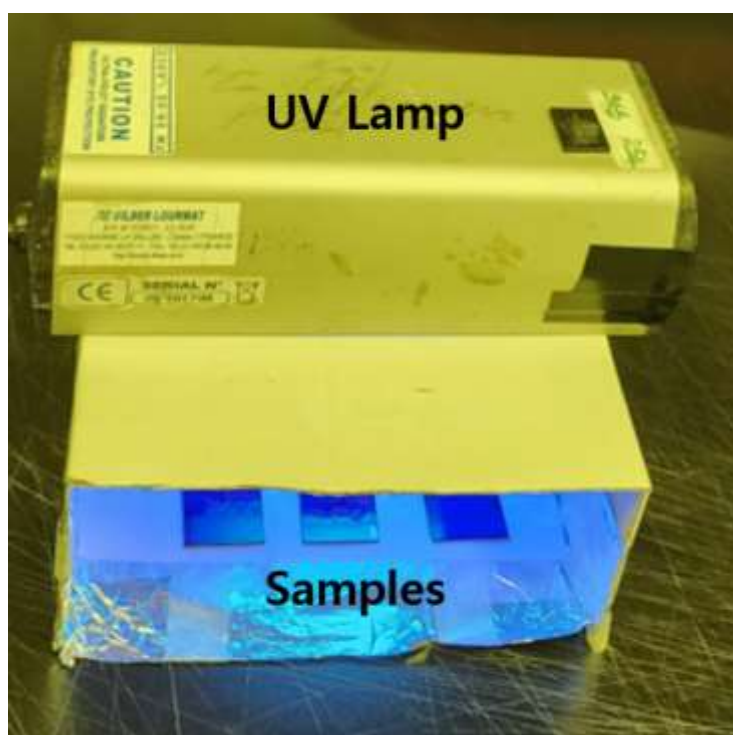
Figure 4.7: Pictorial representation of the UV lamp irradiation process of the samples during cross-linking and UV stability study.

First, the UV-Vis data of the illuminated samples was obtained from a UV-Vis spectrophotometer. The UV stability was estimated as changes in the intensities of the NFA (Y6-BO) absorption peaks with irradiation time. Secondly, the UV stability was investigated using Renishaw inVia plus Raman spectroscopy at a 514 nm laser excitation wavelength within the 1460-1600 cm^{-1} Raman shift. The UV stability was obtained from the changes in the peak intensities of the C=C donor (D)-acceptor (A) linker in Y6-BO at 1554 cm^{-1} Raman shift with irradiation time.

2. Light Soaking (LS) Stability

The LS stability of OSC devices with various ETLs was investigated by monitoring the PCE change over time under constant 1-sun irradiation in an LS chamber with a halogen light source. The temperature and the relative humidity (RH) in the LS chamber were fixed at 40 °C and 85%, respectively.

3. Thermal Stability

To determine the thermal stability, the evolution of PCE of OSCs subjected to thermal stress (85 °C) and RH ranging between 58-68% with time was recorded. A hot plate was used for the thermal stability study as depicted in Figure 4.8.
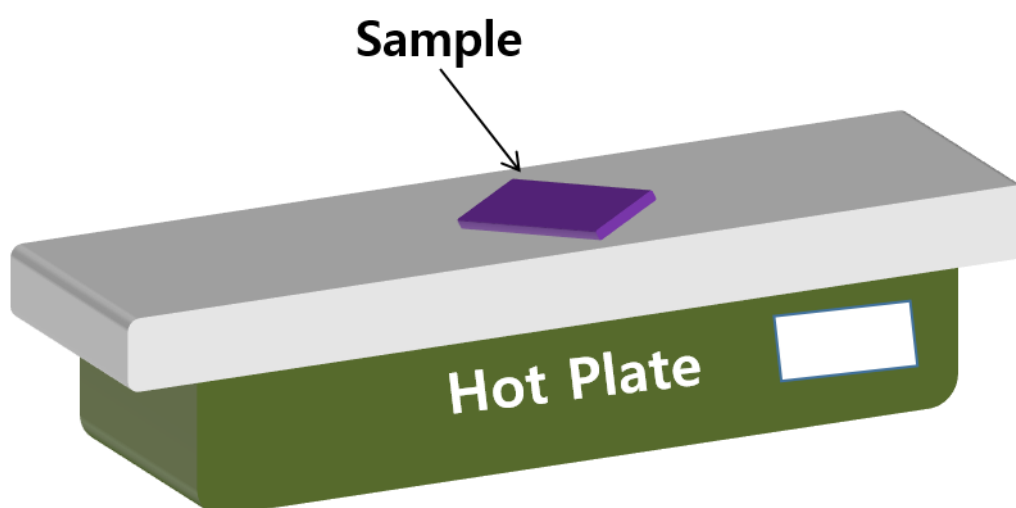
Figure 4.8: Schematic illustration of thermal stability test, whereby OSC device (sample) gets heated on a hotplate in air.

CHAPTER FIVE: RESULTS AND DISCUSSIONS

5.1 Introduction

This chapter is grouped into two parts: The first part focuses on the effect of using ultraviolet resins on ZnO ETL and OSCs. Specifically, the interfacial modification properties of ultraviolet resins, the photovoltaic performance of OSC devices with ZnO ETL modified with ultraviolet resins, and the effect of ZnO ETL modification with ultraviolet resins on the stability of OSCs were investigated. The second part demonstrates the effectiveness of ultraviolet resins using SnO_2 ETL.

5.2 Effect of Ultraviolet Resins as ZnO Surface Modifier

5.2.1 Properties of Ultraviolet Resins

In this study, two ultraviolet resins, SAR and OCS, were used to modify ETLs in OSCs. SAR and OCS resins were commercially acquired with 51,400 and 3,720 mPa.second (centipoise) viscosities, respectively. Their chemical structures showed that both SAR and OCS possess acrylate, a cross-linkable chemical group. The presence of acrylate groups in SAR and OCS resins endowed them with cross-linking characteristics. Both SAR and OCS resins have amine groups that can form interfacial dipoles, thus tuning the ETLs' energy levels to match those of the photoactive materials. Both resins (SAR and OCS) exhibited optical absorption in the UV region and had wider bandgaps than ZnO, as shown in Figure 5.1. The wider bandgaps make them less sensitive to UV light (Jiang *et al.*, 2019). Thus, their application to ZnO ETL is anticipated not to increase the photocatalytic effect.
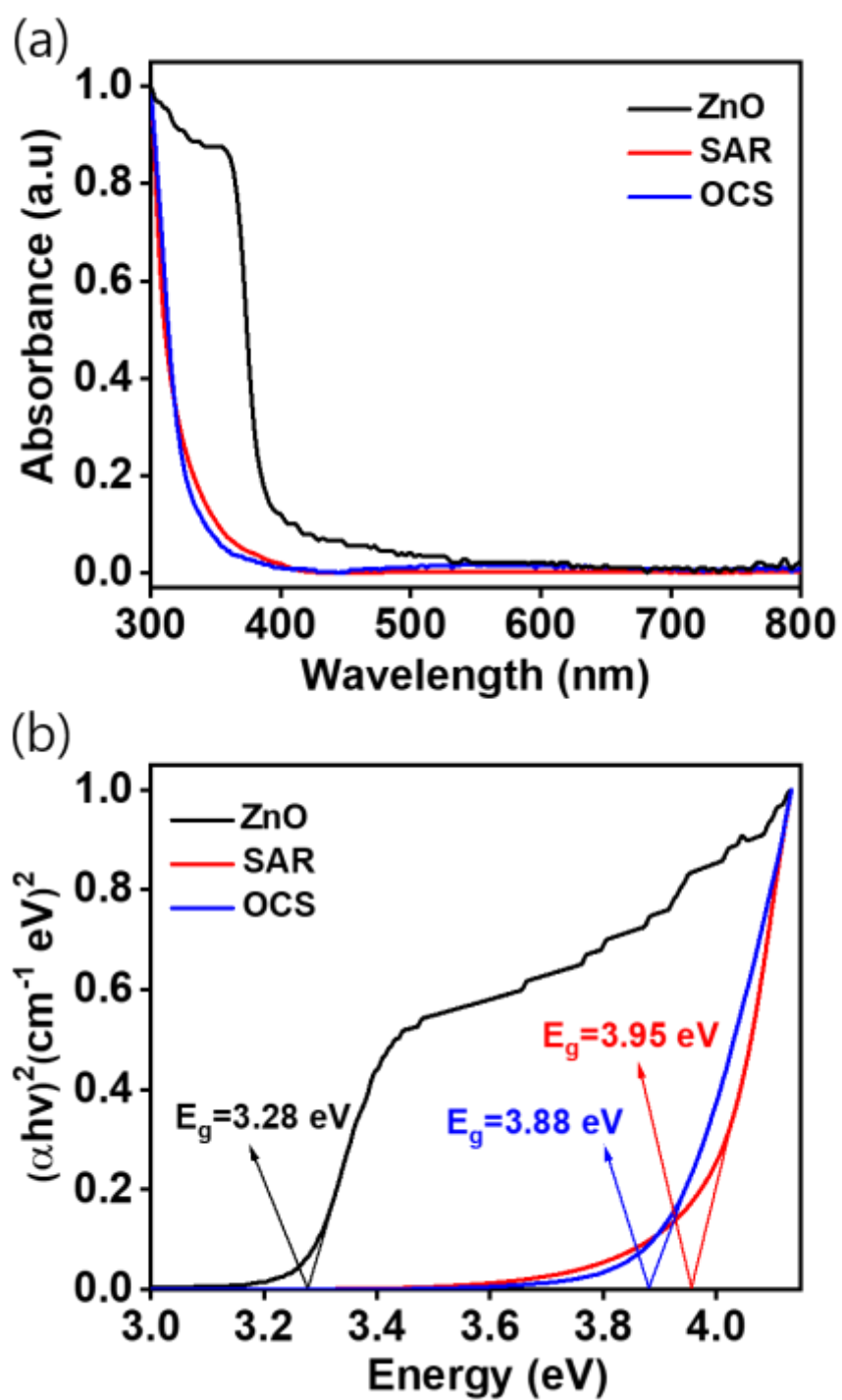
Figure 5.1: **(a)** UV-visible spectra of pristine ZnO ETL, neat SAR, and OCS films. **(b)** Tauc plot showing the calculated optical bandgaps.

5.2.2 Solvent Resistant Properties of SAR and OCS Resins

Before testing the solvent-resistant properties, the photocuring times of the SAR and OCS resins were optimised. This optimisation was performed by monitoring the variation in the PCE of the OSC devices based on SAR and OCS interlayers cured at various times, as shown in Table 5.1 and Figure 5.2. The optimal curing times for the SAR and OCS resins were 5 and 10 minutes, respectively. Based on this optimal curing time, the ETL films (ZnO/SAR or ZnO/OCS) were tested for solvent-resistance properties. The solvent-resistant properties of the cross-linked SAR or OCS resins coated on the ZnO ETL were tested according to a previously reported method (Cai *et al.*, 2021). Generally, the absorption of cross-linked films is measured before and after washing by spin coating the solvents, and a comparison is made. As depicted in Figure 5.3, the absorption peak of the cross-linked films of SAR or OCS coated on the ZnO ETL remained unchanged after washing with the 2-methoxylethanol solvent. In contrast, the absorption peak of the uncross-linked SAR or OCS films coated on ZnO reduced after washing. The retention of the absorption peaks of the cross-linked SAR or OCS films coated on ZnO ETL revealed high solvent-resistant characteristics. This result benefits the deposition of photoactive layers from different solution processing procedures (Cai *et al.*, 2021).

Table 5. 1: Optimisation of the photo-curing time of the SAR and OCS resins.

ETLs	Photo curing time (minutes)	V_{oc} [V]	J_{sc} [mA cm^{-2}]	FF [%]	PCE [%]
ZnO/SAR	0	0.80	23.27	72.57	13.54
	1	0.80	24.20	72.73	14.24
	3	0.80	24.67	72.93	14.45
	5	0.80	25.01	72.95	14.62
	10	0.80	24.14	72.81	14.12
	15	0.80	23.49	72.27	13.72
ZnO/OCS	0	0.80	23.14	72.32	13.44
	1	0.80	23.34	72.63	13.63
	3	0.80	23.70	72.92	13.81
	5	0.80	24.40	72.97	14.44
	10	0.81	24.62	73.12	14.57
	15	0.81	24.09	72.71	14.16
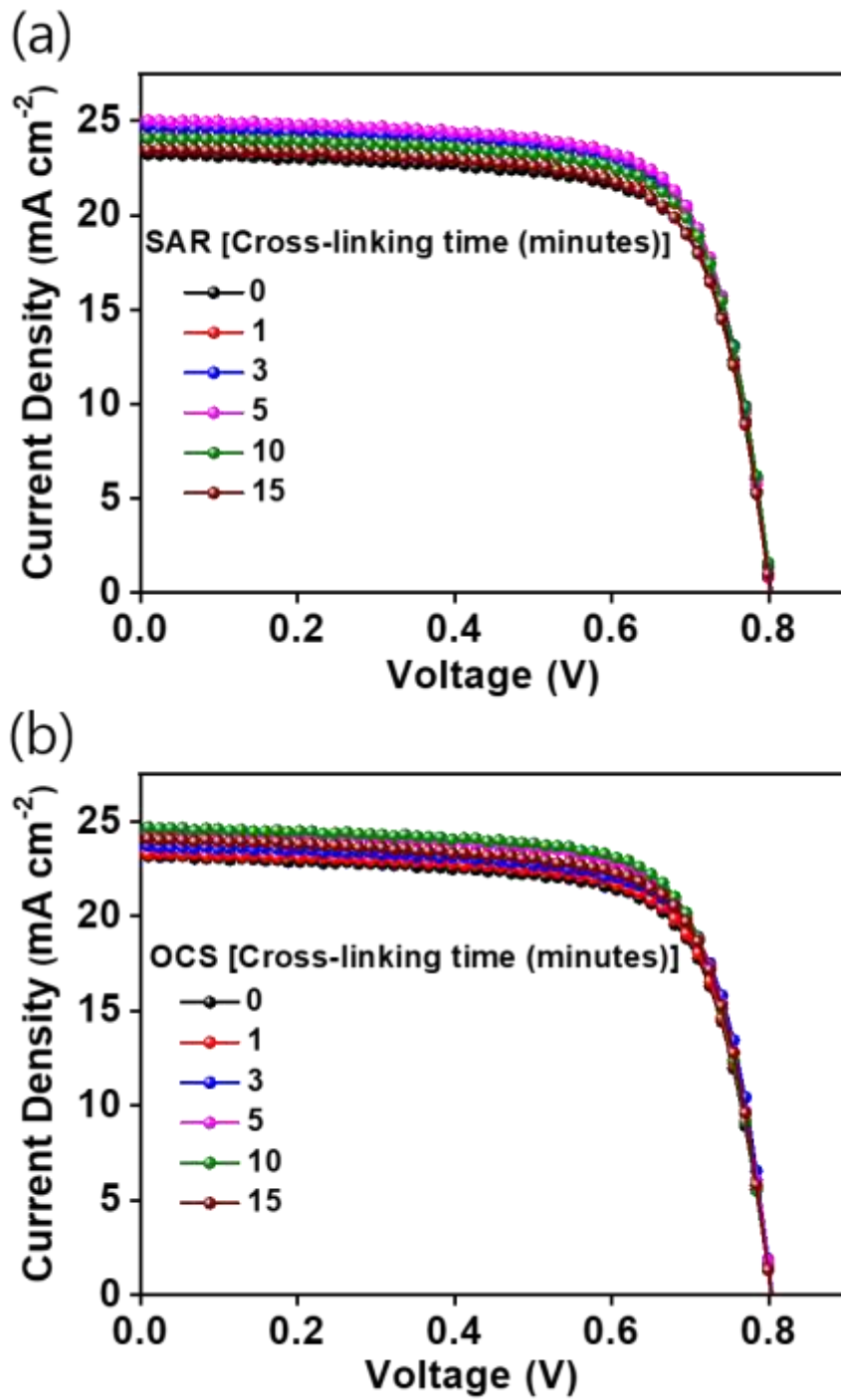
Figure 5.2: J-V curves of the OSC devices based on (a) SAR and (b) OCS interlayers photo-cured (cross-linked) at different times.
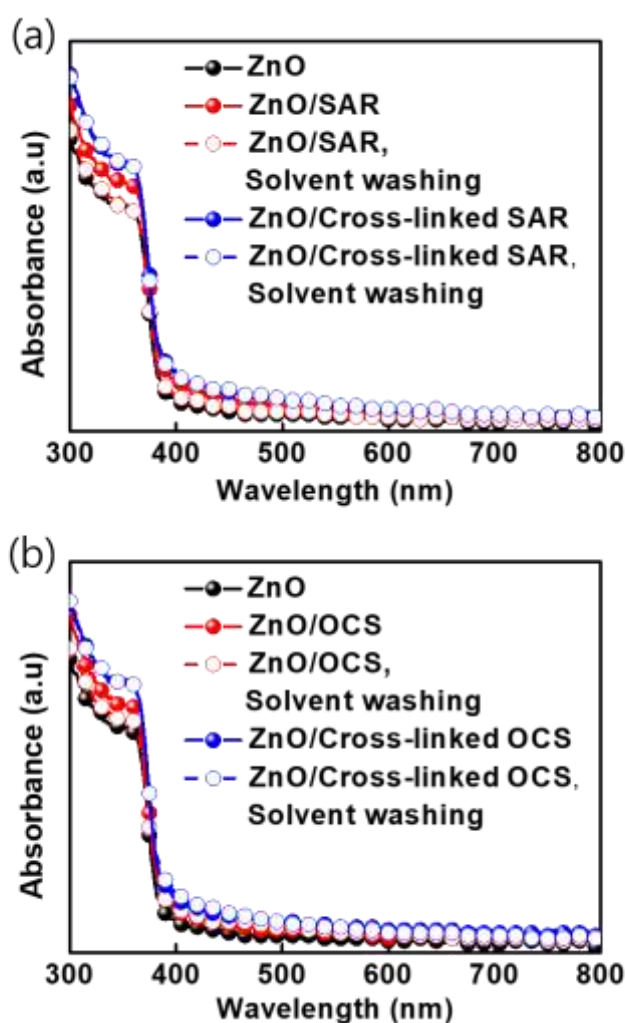
Figure 5.3: UV-Vis absorption spectra illustrating solvent-resistant properties of resins coated on ZnO ETL (a) SAR resin (b) OCS resin.

5.2.3 Interfacial Modification Characteristics of UV Resins

The effects of the SAR and OCS resins on the absorbance and transmittance of ZnO are presented in Figure 5.4. Coating SAR or OCS resins on ZnO ETL enhanced absorption intensity in the UV-visible region due to increased zinc ion concentration. Notably, the optical transmittance of ZnO remained high (above 80 %) and unaltered in the UV-visible region after the SAR and OCS modification, implying that the SAR and OCS resins do not interfere with the transparency of ZnO (Yan *et al.*, 2023).
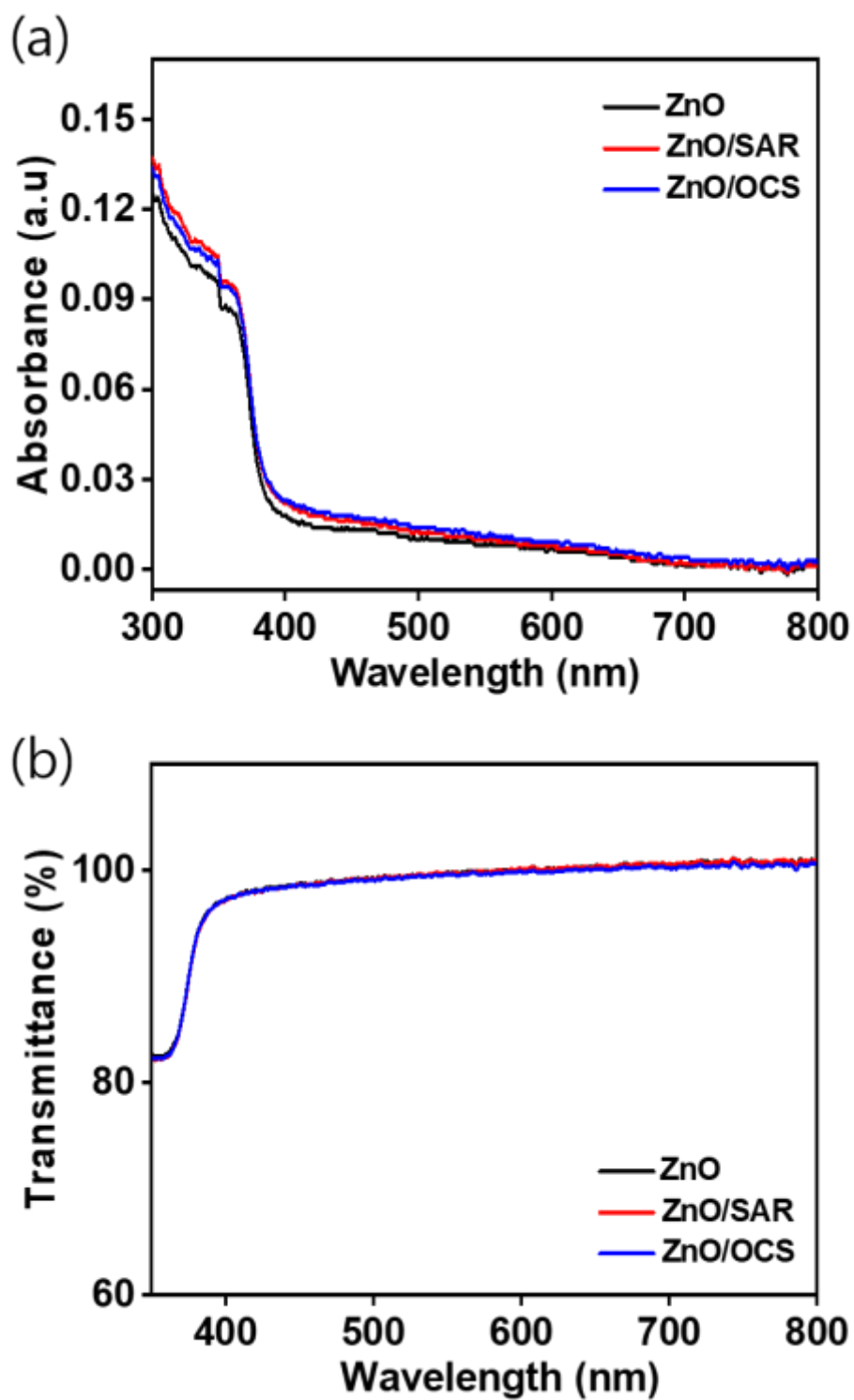
Figure 5.4: (a) Absorption and (b) Optical transmittance curves of SAR and OCS resins coated on ZnO film.

Water and diiodomethane (DIM) drops on the ZnO-modified surface were used to study the surface wettability properties. The DIM and water θ_C on the ZnO-based films were measured as shown in Figure 5.5. The γ values of the modified ETL films were computed from the measured contact angles, as recorded in Table 5.2. The θ_C and γ of the ETLs and PM6:Y6-BO films were compared to establish the interface contact formed. ZnO's water contact angle (θ_w) was measured as 34.9^o while the θ_w of SAR and OCS resins on ZnO were measured as 58.4^o and 71.2^o, respectively. After modification, the enhancement of θ_w of ZnO demonstrates increased hydrophobicity, which could make the ETL have higher resistance to moisture ingress, preventing the decomposition of OSCs. The γ value of the ZnO film was reduced from 64.48 to 51.95 and 47.93 mJ m^{-2} after SAR resin and OCS resin modification, respectively. Relative to the ZnO-only film, the θ_w and γ of ZnO-modified films were more close to those of active layer blend (PM6:Y6-BO) (104.3^o and 29.74 mJ m^{-2}), implying that a better ETL/active layer interfacial contact was formed by modifying ZnO ETL.
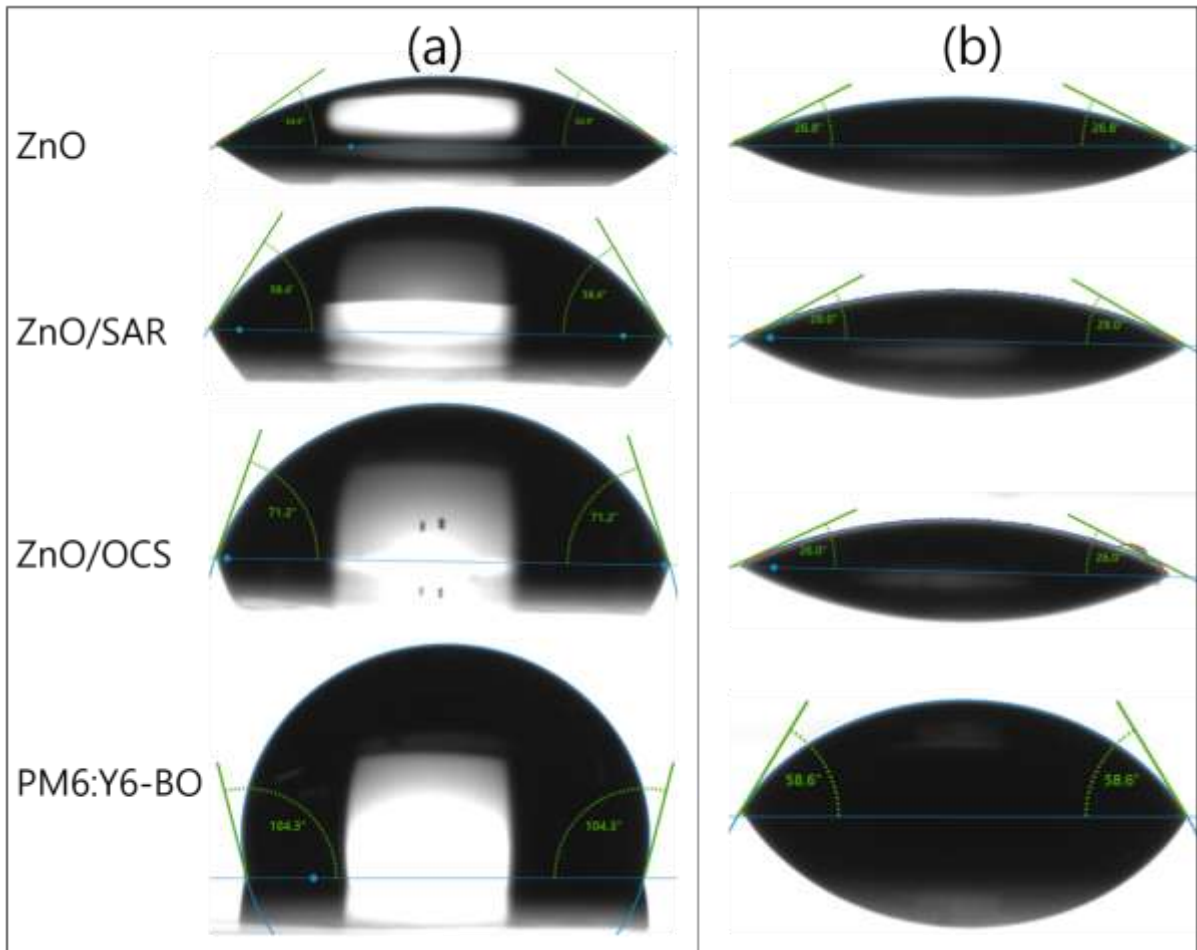
Figure 5.5: θ_C of (a) water and (b) Diiodomethane drops on ZnO, ZnO/SAR, and ZnO/OCS ETLs, and PM6:Y6-BO films.

Table 5. 2: Summary of the θ_C and calculated γ of bare ZnO, ZnO/SAR, and ZnO/OCS ETLs, and PM6:Y6-BO films.

ETL Films	θ_{water} (°)	$\theta_{diiodomethane}$ (°)	γ (mJ m^{-2})
ZnO	34.90	26.80	64.48
ZnO/SAR	58.40	29.00	51.95
ZnO/OCS	71.20	26.00	47.93
PM6:Y6-BO	104.3	58.60	29.74

The effect of the SAR and OCS resins on the WF of ZnO ETL was investigated using UPS, as shown in Figure 5.6 (a). The work functions were calculated from the secondary electron cutoffs (Figure 5.6 (b)), as discussed in the methods section. The WF of ZnO ETL was calculated as 3.83 eV, whereas the work function of ZnO modified with SAR and OCS resins was 3.8 and 3.71 eV, respectively. This decreased WF is believed to be due to the dipole formation from the amine groups of the SAR and OCS resins (Zhu *et al.*, 2019). A decrease in the WF of the ZnO ETL is beneficial for charge extraction and the enhancement of the voltage (V_{oc}) in OSCs.
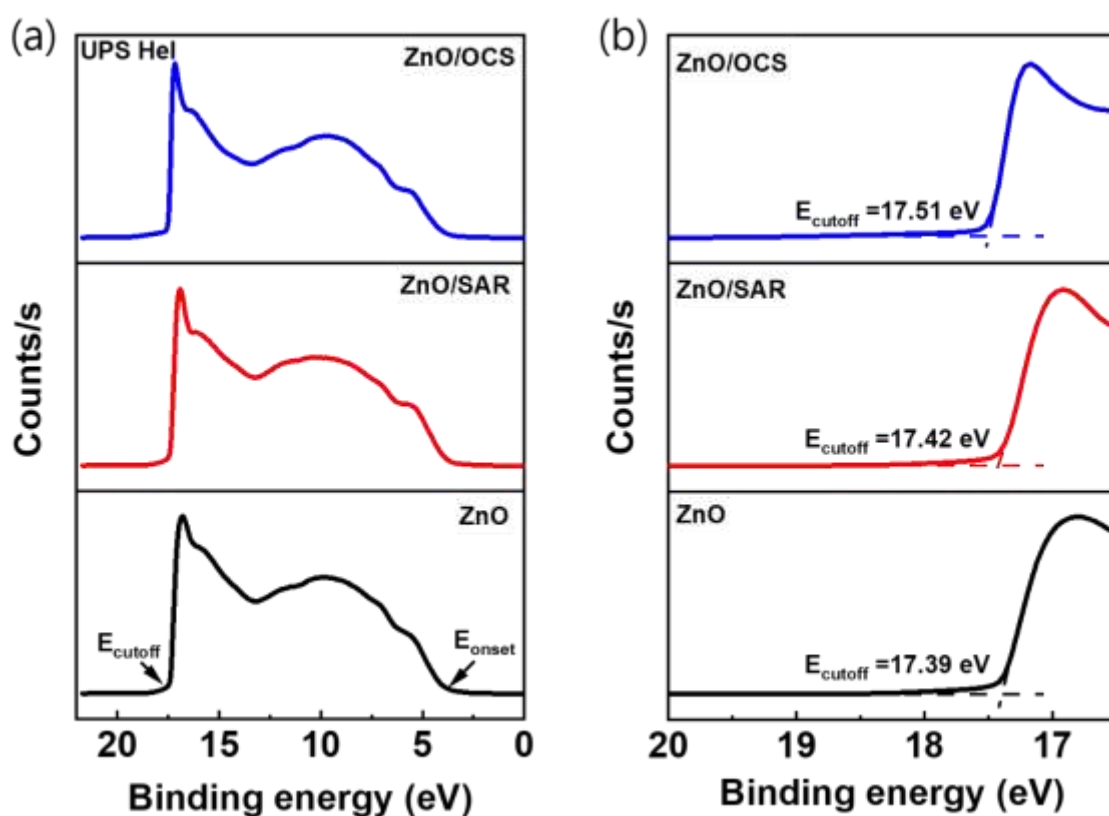
Figure 5.6: UPS plots of electron counts versus binding energy of ZnO-modified ETL films. (a) Full UPS spectra, and (b) The secondary electron cutoffs with calculated work functions.

To establish the effect of the SAR or OCS resins on the chemical state and surface of ZnO, XPS spectra of O 1s and Zn 2p core-level electrons were measured, as shown in Figure 5.7. The Zn 2p spectra have a peak at 1020.8 eV assigned to the Zn 2$p_{3/2}$ state, which defines the Zn^{2+} chemical state (Yang and Yu, 2023). The Zn 2$p_{3/2}$ peak blue shifts by 0.2 eV towards low BE, implying an increased concentration of zinc ions, suggesting a possible interaction between SAR and OCS resins with ZnO. The O 1s XPS spectra have two prominent peaks at 530 eV and 532 eV, assigned to the Zn-O bond and defective oxygen (V$_o$), respectively (Yang and Yu, 2023). With the modification of ZnO with SAR and OCS resins, a third peak appeared at 531 eV, which is speculated to result from the replacement of the hydrogen (H) of –OH adsorbed on the ZnO surface by carbon from the carbonyl group (Fan *et al.*, 2016; Yang and Yu, 2023) at the terminals of the SAR or OCS resins. The ratio of the ZnO defective oxygen peak to the Zn-O bond peak was 0.81. Upon SAR and OCS modification, the ratio reduced to 0.64 and 0.53, respectively, symbolizing passivated surface defects on ZnO.
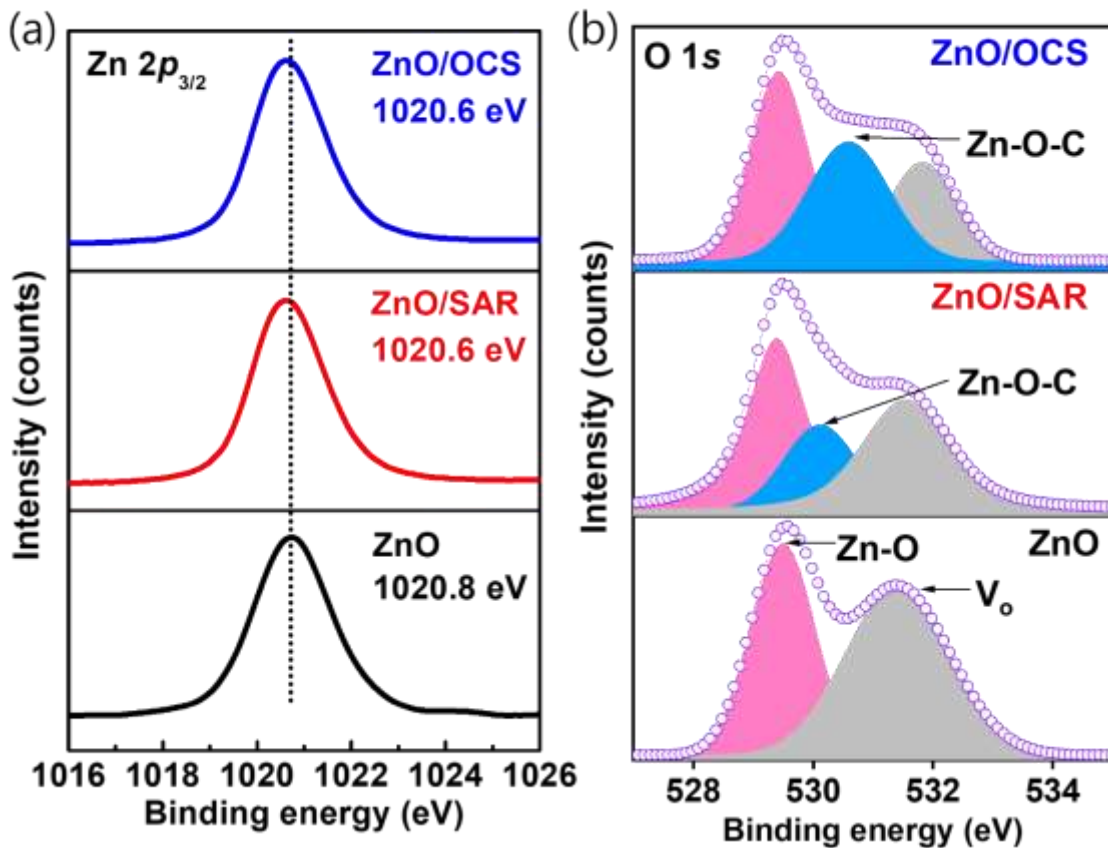
Figure 5.7: XPS spectra of various ETL films. (a) Zn 2p and (b) O 1s.

Further studies on the surface defect passivation were conducted using PL spectroscopy, as presented in Figure 5.8. The PL spectra of ZnO have UV and visible region emission peaks centred at 393 and 489 nm, respectively, corresponding to exciton recombination and surface defects on ZnO (Huang *et al.*, 2022). The UV and Visible peak intensities of the various ETL films are listed in Table 5.3. It was discovered that the PL peak intensities were reduced by modifying ZnO. To establish the variation in surface defects upon modifying ZnO, the ratio of the Visible to UV region emission peak intensities was calculated, as shown in Table 5.3. For the case of the ZnO-only films, a ratio of 0.92 was calculated, whereas for the ZnO/SAR and ZnO/OCS films, lower ratios of 0.89 and 0.88 were obtained, respectively. The ratio of the Visible to UV region emission peak intensities reduced upon ZnO modification, further confirming the passivation of surface defects on ZnO (Huang *et al.*, 2022).
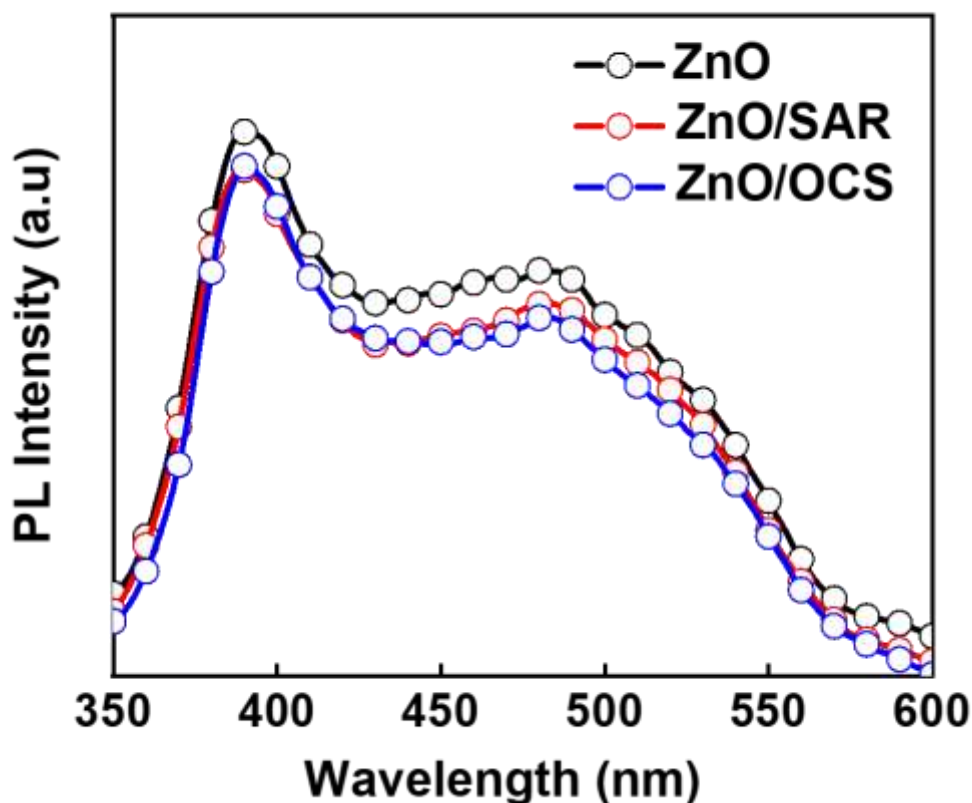
Figure 5.8: Photoluminescence spectra of ZnO, ZnO/SAR, and ZnO/OCS electron transport layer films excited at 340 nm wavelength.

Table 5. 3: PL and UV-visible emission peak intensities of ZnO, ZnO/SAR, and ZnO/OCS films, and the corresponding Visible to UV emission peak ratios.

ETL Films	UV emission Peak (Peak 1)	Visible emission peak (Peak 2)	Ratio (Peak2/Peak1)
ZnO	22.065	20.250	0.92
ZnO/SAR	20.367	18.139	0.89
ZnO/OCS	20.014	17.569	0.88

5.2.4 Photovoltaic Performance of OSCs based on ZnO ETLs

The effect of modifying ZnO with SAR or OCS resins on the performance of OSCs was investigated using the ITO/ZnO/UV resins/PM6:Y6-BO/MoO$_3$/Ag device structure. This study used a blend of PM6 with Y6-BO materials in the active layer. This decision was based on the materials' reported outstanding performance and the fact that Y6-BO has decent solubility in green solvent o-xylene, as highlighted by Abbas *et al.* (2022). The study's findings are presented in Table 5.4, which outlines the photovoltaic performance characteristics of OSCs with ZnO-modified ETLs. The PCE of OSCs with bare ZnO ETL was obtained as 13.6%, whereas the PCE of OSCs with modified ZnO ETLs was obtained as 14.6%.

Table 5. 4 Photovoltaic performance of OSCs with ZnO, ZnO/SAR, and ZnO/OCS ETLs. In parenthesis are the statistical data from 6 averaged devices.

ETL	V_{oc} [V]	J_{sc} [mA/cm^2]	J_{cal} [mA/cm^2]	FF [%]	PCE [%]
ZnO	0.800	24.24	23.0	70.0	13.6 (13.41±0.15)
ZnO/SAR	0.801	25.01	24.2	73.0	14.6 (14.50±0.11)
ZnO/OCS	0.809	24.62	23.5	73.1	14.6 (14.41±0.18)

The J-V and EQE curves of the OSCs are shown in Figure 5.9, where the J-V curve of ZnO-based OSCs is lower relative to that of OSCs with the modified ZnO ETL. Also, the EQE curves of the OSCs with modified ZnO were higher as compared to those of the ZnO-based OSCs in the UV-Vis region, implying enhanced photon utilisation with SAR and OCS modification. The calculated J_{sc} from the EQE curves were consistent with the J_{sc} obtained from the J-V measurements under light, confirming the precision of the measurements.
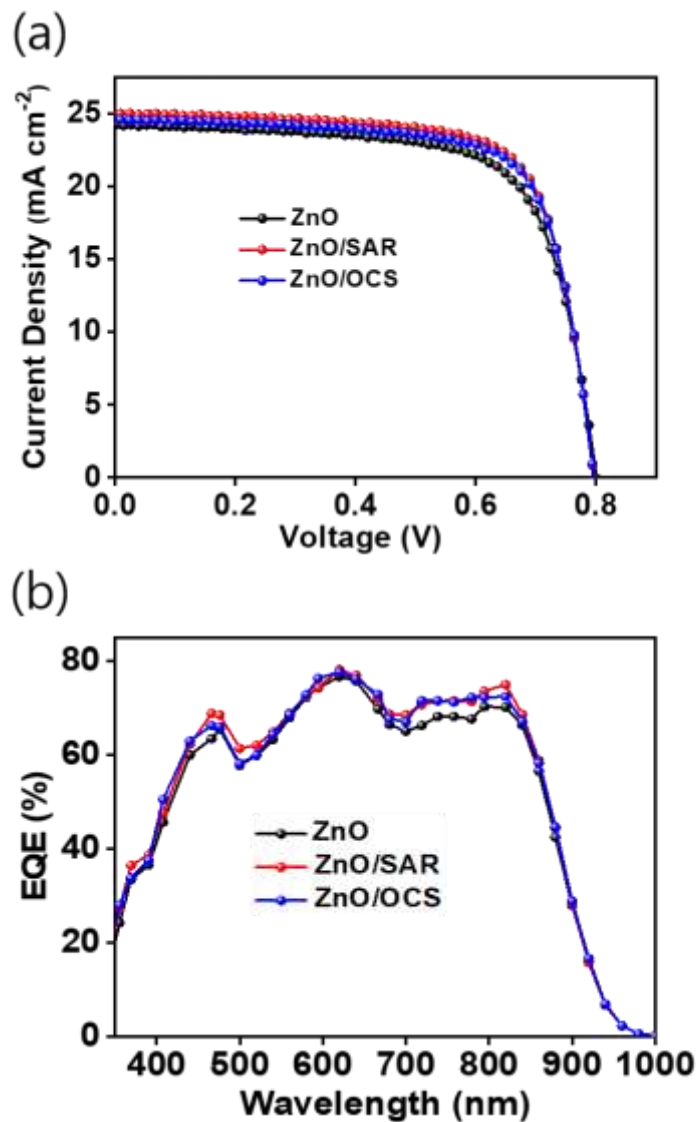
Figure 5.9: (a) The J-V and (b) EQE curves of OSCs with ZnO-modified ETLs.

Further studies were conducted to determine the causes of the improved PCE after modifying the ZnO ETL. First, the charge dissociation probability P (E, T), was obtained from photocurrent measurements, as described in the methodology section. The photocurrent curves of the OSCs with ZnO-modified ETLs are presented in Figure 5.10. The P (E, T) value of the OSCs with the pristine ZnO ETL was 95.5%. In contrast, the P (E, T) of the OSC devices with ZnO/SAR and ZnO/OCS were obtained as 97.4% and 97.2%, respectively. The larger P (E, T) values of the OSCs obtained after modifying ZnO ETL imply that the charge extraction process in the OSCs was improved, accounting for enhanced J_{sc} and FF.
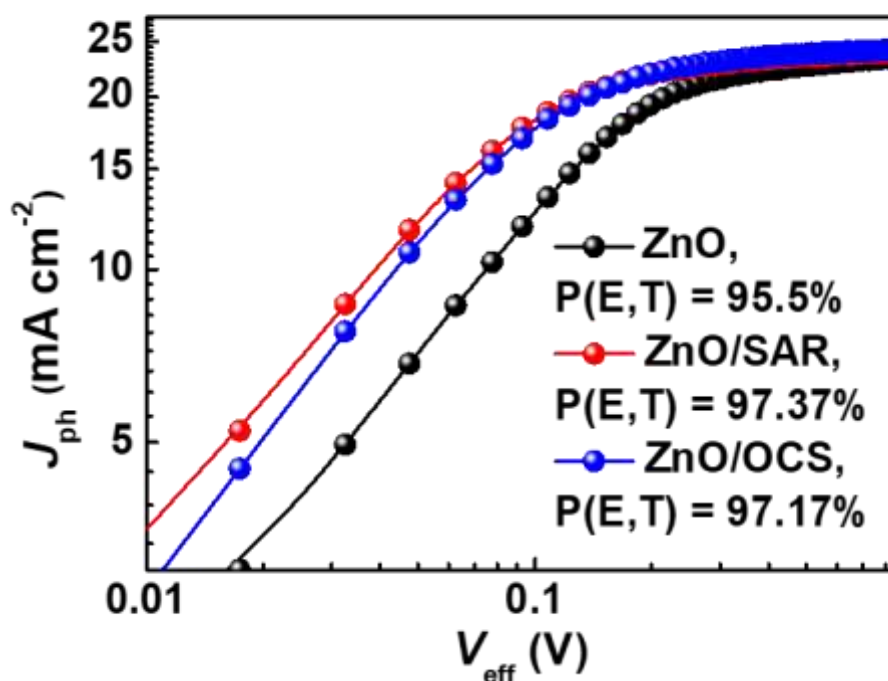
Figure 5.10: J_{ph}-V_{eff} curves of OSCs with ZnO, ZnO/SAR, and ZnO/OCS ETLs.

The exciton dissociation efficiency of the OSCs is directly related to the morphology of the photoactive layer. Inspired by the observed phenomenon of enhanced P (E, T) of OSCs with modified ZnO, the morphological evolution of the PM6:Y6-BO blend coated on ZnO-modified ETLs was studied, as shown in Figure 5.11. It was observed that upon modification of the ZnO ETL film with SAR and OCS resins, the root mean square (RMS) value of the PM6:Y6-BO film decreased from 1.14 nm to 1.05 nm and 1.03 nm, respectively. This decrease in the RMS values of the PM6:Y6-BO films coated on ZnO/SAR and ZnO/OCS demonstrated that a more

homogeneous and uniform surface was formed, which is favourable for the dissociation of exciton and transport of charges in the photoactive layer. This result supports the increased exciton dissociation probability obtained for the OSCs with ZnO-modified ETLs.
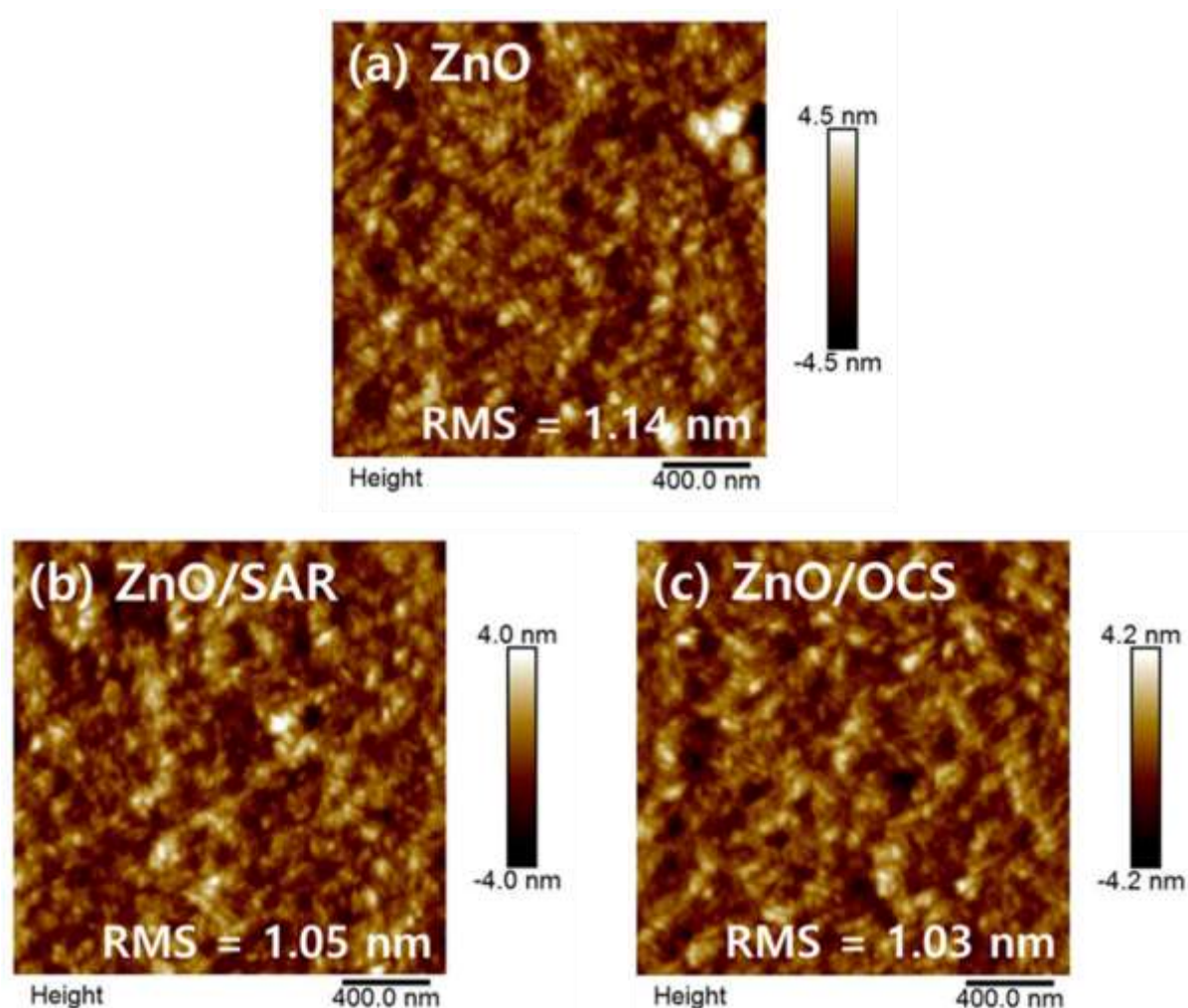
Figure 5.11: The topographic AFM height images of the PM6:Y6-BO films coated on (a) ZnO, (b) ZnO/SAR, and (c) ZnO/OCS ETLs obtained using AFM.

Secondly, the charge recombination behaviour of OSC devices with ZnO-modified ETLs was studied by measuring the J_{sc} and V_{oc} versus P_{light} curves and the electrochemical impedance spectra, as described in the methodology section and presented in Figure 5.12. When the J_{sc}-P_{light} curve slope (α) approaches one, bimolecular recombination is termed weaker (Mai *et al.*, 2023), whereas when the slope of V_{oc} - P_{light} (n) nears $2kT/q$, trap-assisted recombination is termed dominant (Song *et al.*, 2023). Here, k, q, and T refer to the Boltzmann constant,

elementary charge, and absolute temperature, respectively. As shown in Figure 5.12 (a), the α value of the OSCs with the ZnO ETL was 0.95, whereas that of the OSC devices with ZnO/SAR and ZnO/OCS ETLs was 0.96. The higher α value obtained for the case of the modified ZnO ETLs indicates weaker bimolecular recombination. Similarly, the lower value of n obtained in Figure 5.12 (b) suggests that trap-assisted recombination in OSC devices with ZnO-modified ETLs was suppressed. The electrochemical impedance spectra in Figure 5.12 (c) were used to study the changes in the resistivity of OSCs as a result of ZnO ETL modification. The series resistances of the OSCs with ZnO/SAR and ZnO/OCS ETLs were 11 and 10 Ω, respectively, while that of the control OSC devices with bare ZnO ETL was 24 Ω. This reduced resistance confirms the reduced charge recombination in the OSCs upon ZnO ETL modification. The suppression of charge recombination facilitates charge extraction and transport, thus improving photovoltaic performance.
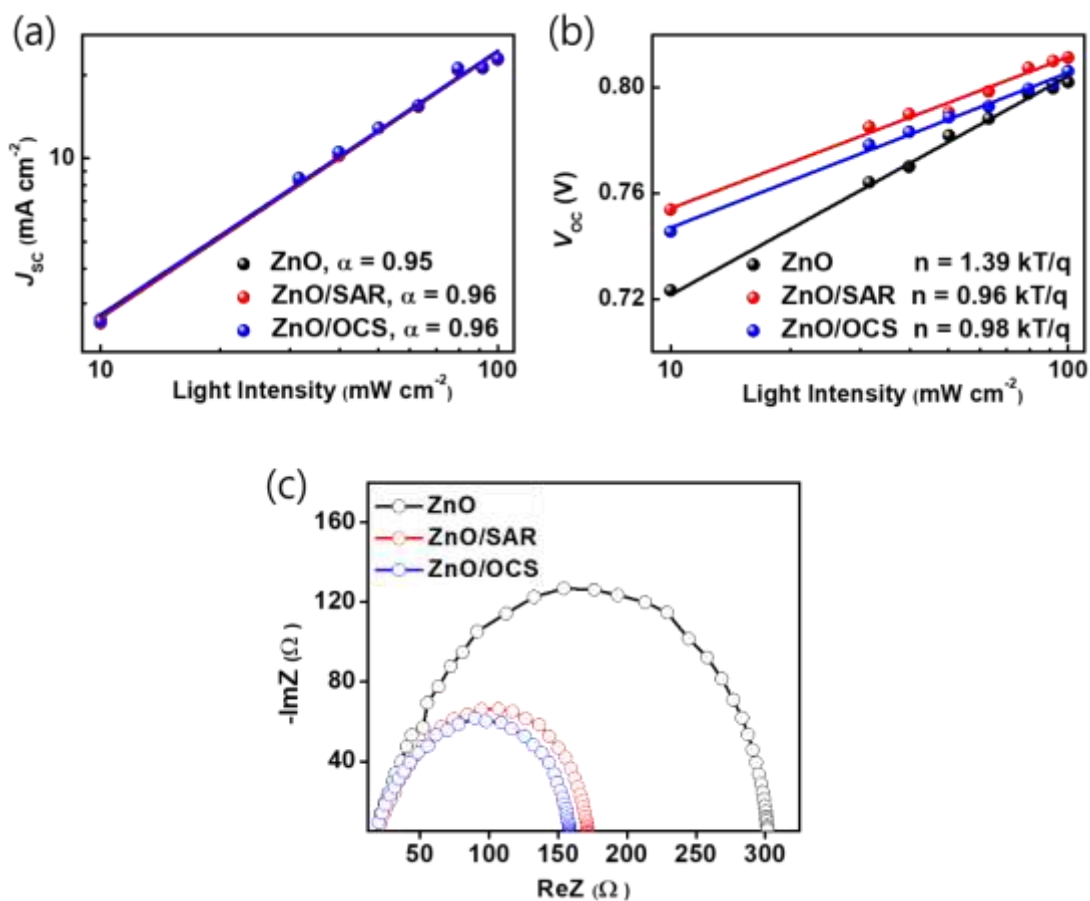
Figure 5.12: (a) J_{sc}-P_{light} curves, (b) V_{oc}-P_{light} curves, and (c) Nyquist curves of OSCs with ZnO, ZnO/SAR, and ZnO/OCS ETLs.

Finally, the electron mobility (μ_e) and trap density (N_{trap}) of the ITO/ZnO/UV resins/PM6:Y6-BO/ZnO/Ag devices were determined, as discussed in the methodology section and depicted in Figure 5.13. The μ_e of the unmodified ZnO based device was found to be 4.4×10^{-4} cm^{2}V^{-1}S^{-1}, whereas the μ_e of the devices with ZnO/SAR and ZnO/OCS ETLs was determined to be 4.7×10^{-4} cm^{2}V^{-1}S^{-1} and 4.6×10^{-4} cm^{2}V^{-1}S^{-1}, respectively. The increased μ_e of devices based on ZnO-modified ETLs demonstrates improved charge transport, which results in improved J_{sc} of the OSCs. Moreover, the N_{trap} was calculated from the V_{TFL} values shown in Figure 5.13 as 1.51×10^{16}, 1.17×10^{16}, and 1.06×10^{16} cm^{-3} for electron-only devices with ZnO, ZnO/SAR and ZnO/OCS ETLs , respectively. Upon ZnO modification, N_{trap} decreased implying reduced trap recombination, which facilitates faster electron transport, thus improving the J_{sc} of OSCs.
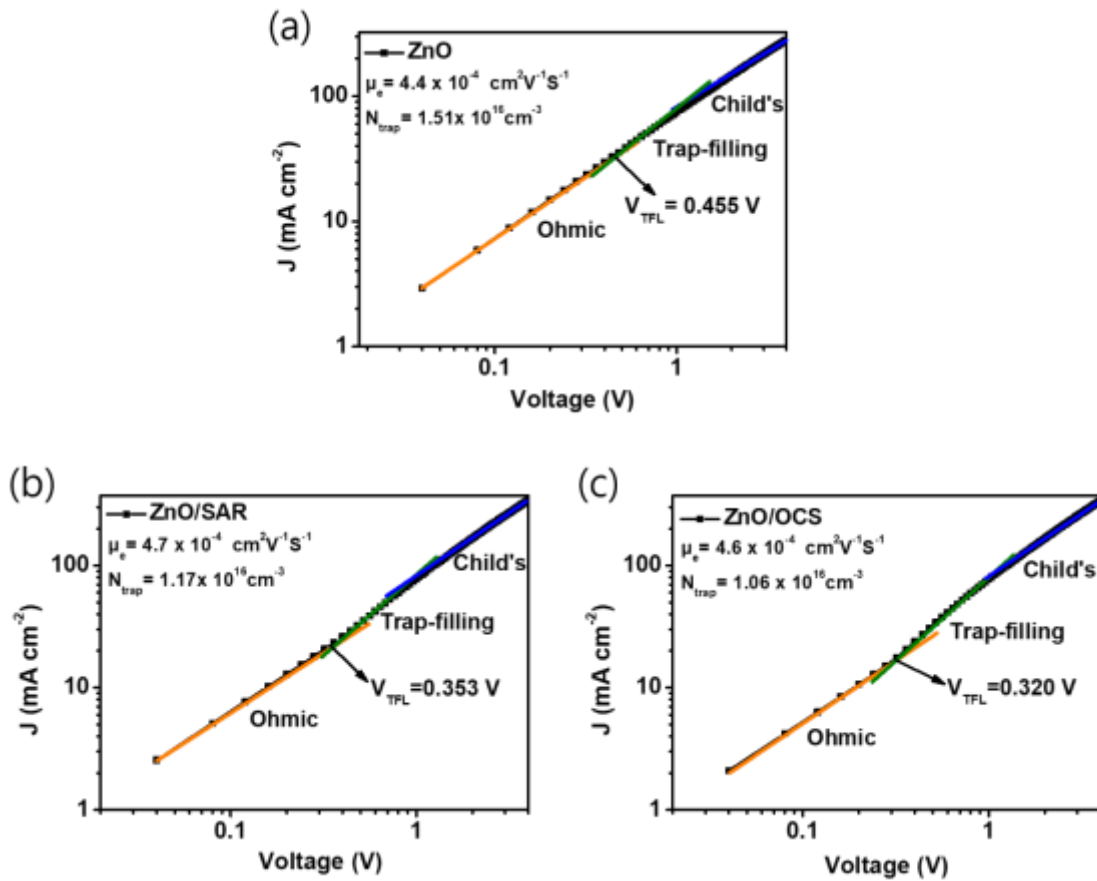
Figure 5.13: Three-segment *J-V* curves in the dark of electron-only devices. (a) ZnO, (b) ZnO/SAR, and (c) ZnO/OCS ETLs.

5.2.5 Stability of OSCs

First, an investigation was performed to establish the concentration at which SAR and OCS resins provided optimal stability. OSCs with SAR or OCS resin interlayers with various concentrations were tested for photostability using a light-soaking chamber as presented in Figure 5.14 (a, b). For both SAR- and OCS-resin-based OSCs, the optimal concentration with the highest photostability after 90 hours was 5.2 wt%. At this optimal concentration, the OSCs based on both SAR and OCS interlayers showed the least dark current of 8.95×10^{-5} A cm^{-2} and 3.51×10^{-6} A cm^{-2}, respectively, at -2V (Figure 5.14 (c, d)), demonstrating the most suppressed charge recombination.
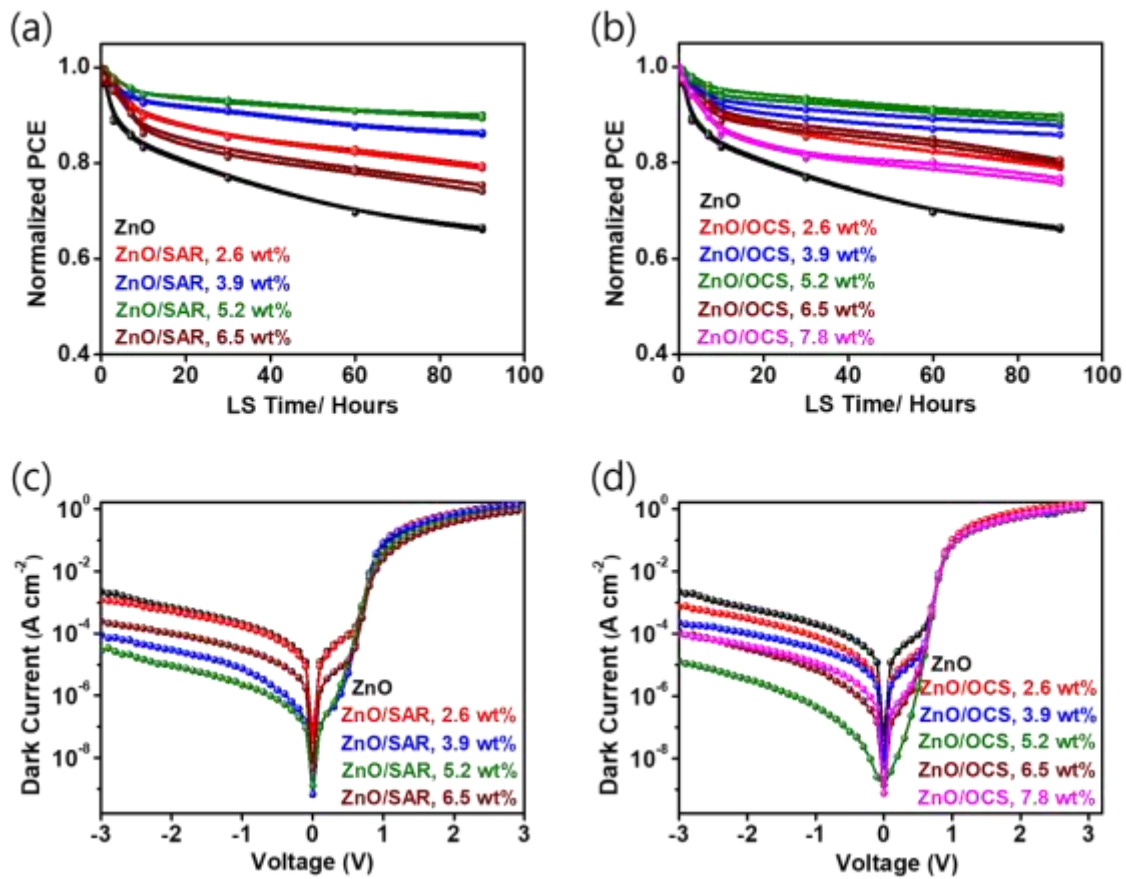
Figure 5.14: (a and b) Photostability and (c and d) Leakage current of OSCs based on various concentrations of the SAR and OCS resin interlayers.

The photostability of the OSCs was further investigated for 1000 h based on the optimal concentration of SAR and OCS resins. As depicted in Figure 5.15 (a), the PCE of OSCs based on pristine ZnO decreased to 57%, while the PCE of OSCs based on modified ZnO ETLs decreased to 79%. As illustrated in Figure 5.15 (b-d) and Table 5.5, the higher stability of OSCs based on ZnO-modified ETLs was mainly due to the higher J_{sc} and FF during the light soaking period.
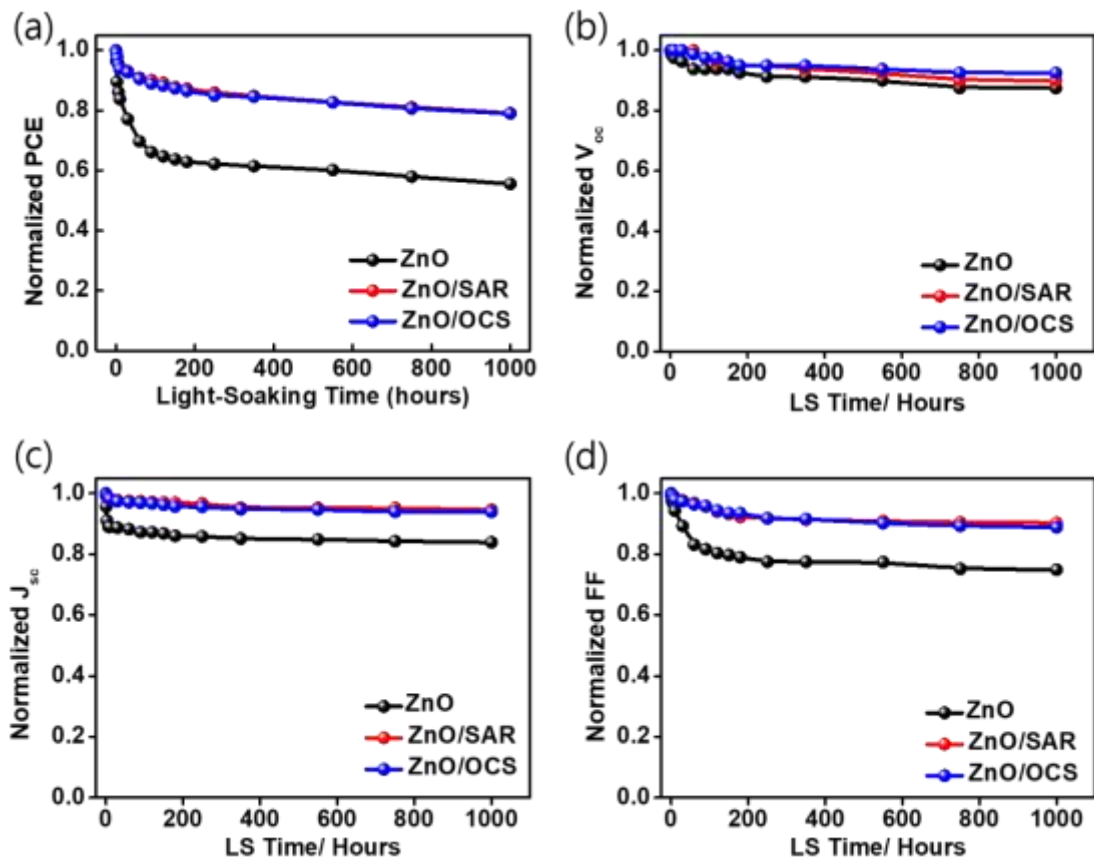
Figure 5.15: PCE, V_{oc}, J_{sc}, and FF of OSCs versus light soaking time.

Table 5. 5: Photovoltaic performance characteristics of photo-aged OSCs based on various ETLs.

ETLs	LS hours	V_{oc} (V)	V_{oc} Drop	J_{sc} (mA cm^{-2})	J_{sc} Drop	FF (%)	FF Drop	PCE (%)	PCE Drop
ZnO	0	0.80		23.91		70.81		13.52	
	1000	0.71	↓11%	20.42	↓15%	52.85	↓25%	7.66	↓43%
ZnO/SAR	0	0.80		23.75		70.00		13.32	
	1000	0.74	↓8%	22.32	↓6%	63.67	↓9%	10.49	↓21%
ZnO/OCS	0	0.80		23.67		71.45		13.58	
	1000	0.75	↓6%	22.27	↓6%	64.27	↓10%	10.72	↓21%

Additionally, the leakage current increase during the 1000 h light soaking period was found to be retarded for OSCs with ZnO-modified ETLs relative to the OSCs with ZnO-only ETL. Figure 5.16 shows that the leakage current in ZnO-based OSCs increased by 2.5 order at -2V. In contrast, the leakage current of the OSCs with the modified ZnO ETLs increased with the lower order (1.3 and 1.4), further supporting the higher stability observed when SAR and OCS resins were used to modify the ZnO ETL. This stability result is comparable to the best-reported ones in the literature for NFA-based inverted OSCs based on ZnO ETLs (Table 5.6).
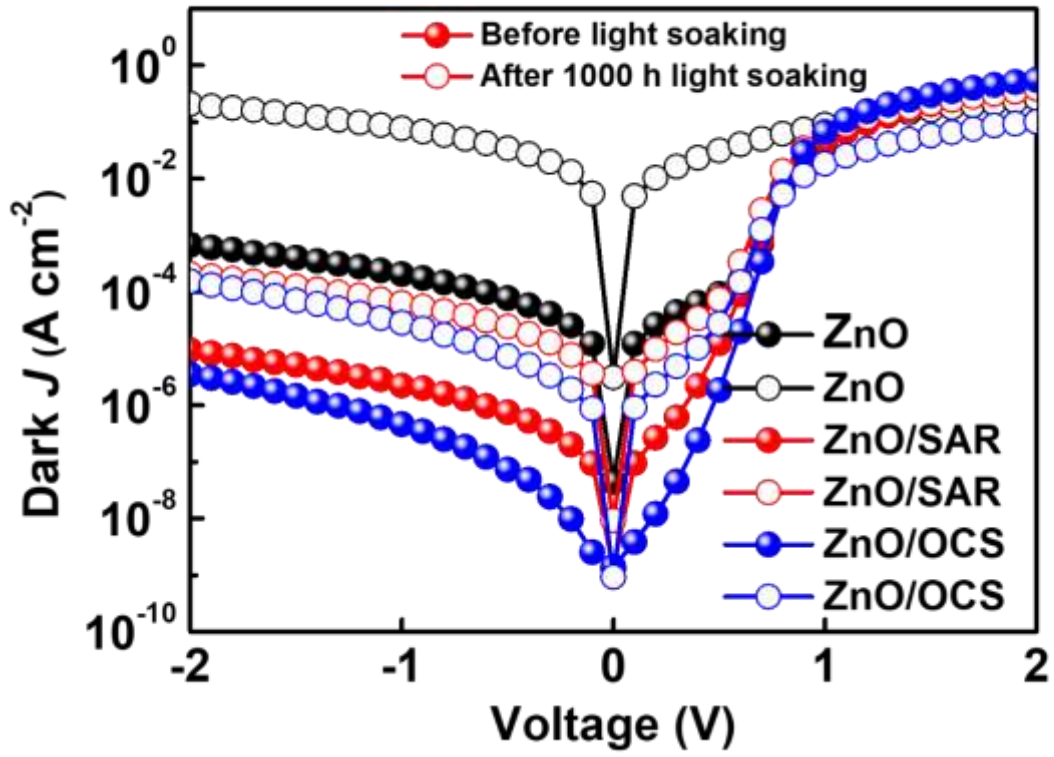
Figure 5.16: Evolution of dark current of OSCs during 1000 hours of light soaking.

Table 5. 6: Comparison of the photostability of OSCs achieved in this study with the previously reported photostability reports of NFA-based inverted OSCs based on ZnO bilayer ETLs.

Active Layer	ETLs	Stability test condition	Light source	Test time (hours)	PCE drop (%)	Reference
PBDB-T:ITIC	ZnO/SAM	1 Sun	Metal halide lamp	180	30	(Liu *et al.*, 2019)
PTB7-Th:IEICO-4F	ZnO/C_{60}-SAM	1 Sun	LED	34000	20	(Xu *et al.*, 2020)
PBDB-T:ITIC	ZnO/poly-Lysine	1 Sun	–	400	20	(Huang *et al.*, 2020a)
PM6:IT-4F	ZnO/Py-BDP	1 Sun	–	9	41	(Soultati *et al.*, 2020)
PCE-10:BT-CIC	ZnO/IC-SAM	1 Sun	LED	1900	6	(Li *et al.*, 2021c)
PM6:Y6:PC$_{71}$BM	ZnO/a-PEI	1 Sun	–	1000	25	(Hu *et al.*, 2021)
PM6:Y6	ZnO/Glu	1 Sun	LED	1250	8	(Liu *et al.*, 2022)
D18:N3	ZnO/NMA	1 Sun	LED	7572	20	(Li *et al.*, 2022b)
PM6:L8-BO	ZnO/C4A	1 Sun	LED	480	20	(Li *et al.*, 2023b)
	ZnO/BuC4A			410		
PM6:Y6	ZnO/NS-GNS	1 Sun	LED	2000	20	(Su *et al.*, 2022)
PM6:Y6-BO	ZnO/SAR	1 Sun	Metal halide lamp	1000	21	This Work
	ZnO/OCS				21	

To further elucidate the reason for the improved photostability, the effect of SAR and OCS resins coated on ZnO ETLs on the degradation of NFA was studied. The ZnO/Y6-BO, ZnO/SAR/Y6-BO, and ZnO/OCS/Y6-BO films were subjected to UV light illumination for 60 h and the changes in the absorption profile (Figure 5.17 (a-c)) and Raman peaks of NFA (Y6-BO) C=C bond (Figure 5.18 (a-c)) were monitored. The ZnO/Y6-BO absorption peak at approximately 830 nm was essentially reduced after 60 h of UV illumination. In contrast, the ZnO/SAR/Y6-BO and ZnO/OCS/Y6-BO films exhibited minor reductions in the absorption intensities. This indicates that the UV resins act as physical barriers to direct contact between ZnO and Y6-BO, thus reducing the degradation of Y6-BO by photocatalytic ZnO. Similarly, the Y6-BO's C=C bond located at 1530 cm^{-1} in the Raman spectra showed a more significant decrease for the ZnO/Y6-BO films than for the Y6-BO films coated on ZnO/SAR and ZnO/OCS based films corroborating the UV results.
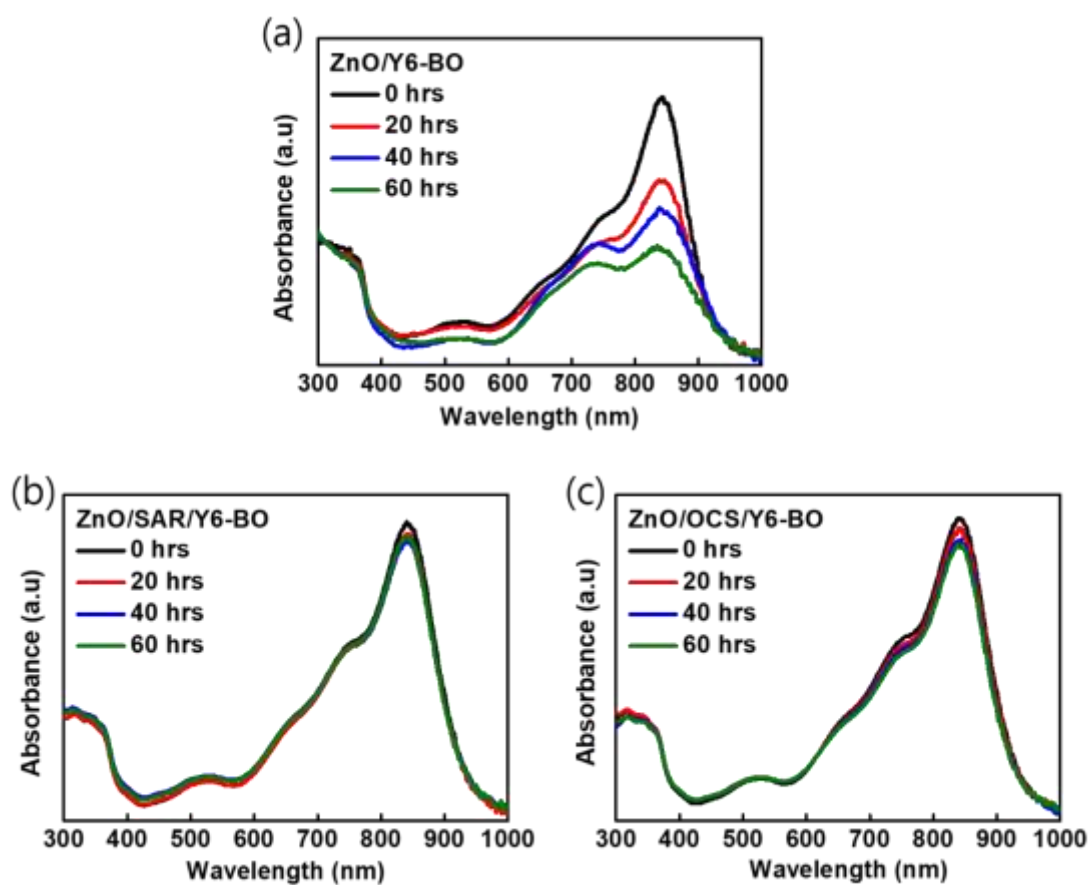
Figure 5.17: The decomposition of Y6-BO by ZnO. (a-c) Absorption spectra of Y6-BO films coated on various ETL films under UV light illumination for 60 hours.
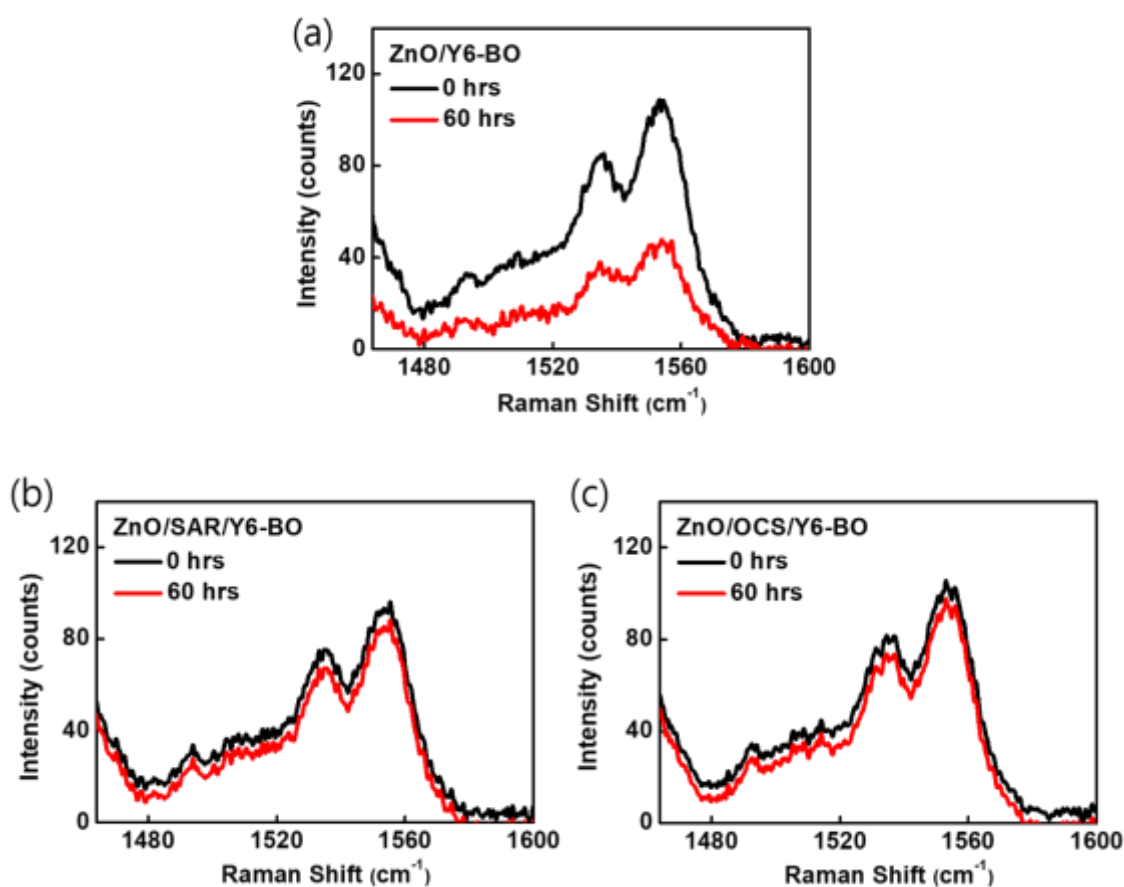
Figure 5.18: The decomposition of Y6-BO by ZnO. (a-c) Raman spectra of Y6-BO films coated on various ETL films under UV light illumination for 60 hours.

Moreover, thermal stability was investigated for a period of 200 h. Figure 5.19 (a) shows that the PCE of OSCs with ZnO-only ETL dropped to 54%, while the PCE of OSCs with ZnO-modified ETLs dropped to 77%. It can also be seen in Figure 5.19 (b-d) and Table 5.7 that the FF mainly contributed to the stable PCE of OSCs based on ZnO-modified ETLs.
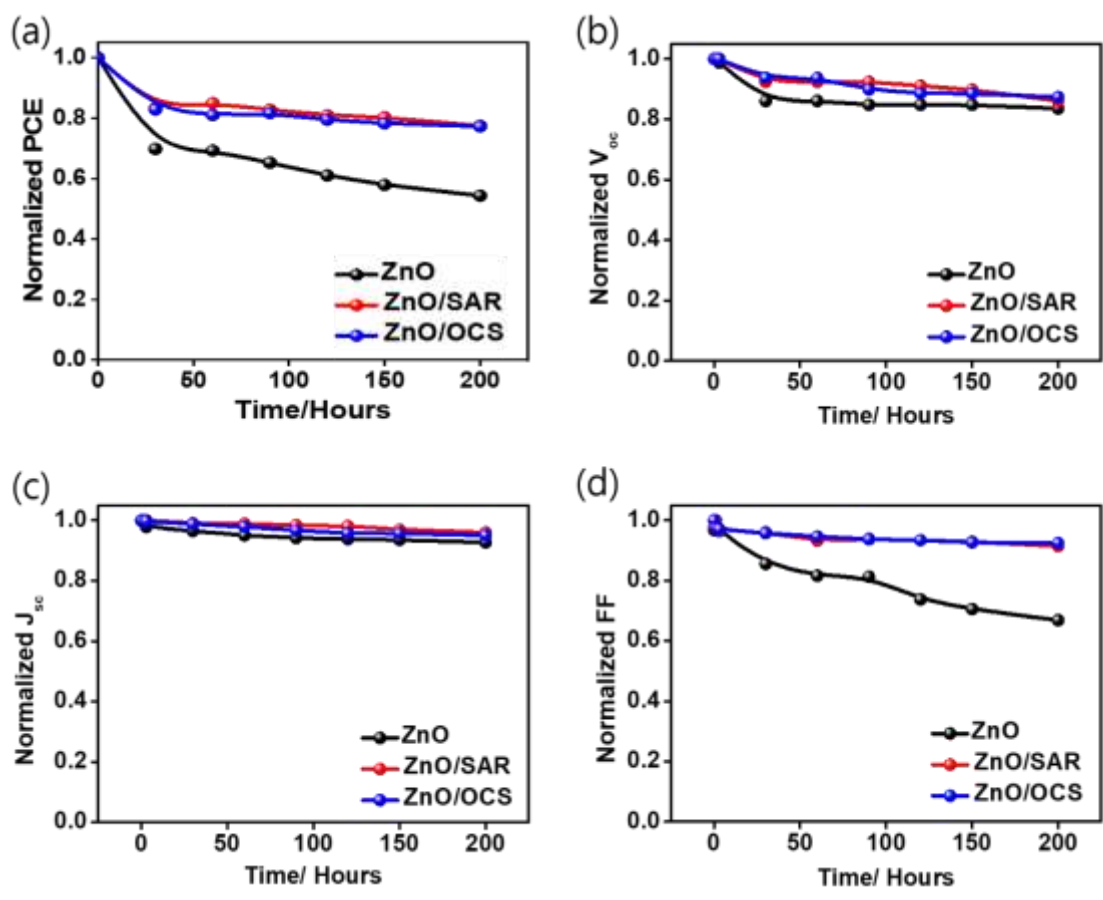
Figure 5.19: Variation of photovoltaic performance characteristics of OSCs during 200 hours of thermal ageing.

Table 5. 7: The photovoltaic performance characteristics of thermal aged OSCs with ZnO, ZnO/SAR, and ZnO/OCS ETLs.

ETLs	Ageing hours	V_{oc} (V)	V_{oc} Drop	J_{sc} (mA cm^{-2})	J_{sc} Drop	FF (%)	FF Drop	PCE (%)	PCE Drop
ZnO	0	0.79		24.31		57.11		10.93	
	200	0.66	↓16%	22.54	↓7%	39.46	↓31%	5.94	↓46%
ZnO/SAR	0	0.79		24.03		61.27		11.67	
	200	0.68	↓14%	23.09	↓4%	57.35	↓6%	9.04	↓23%
ZnO/OCS	0	0.79		24.13		65.51		12.48	
	200	0.69	↓13%	22.94	↓5%	60.55	↓8%	9.64	↓23%

Furthermore, the higher thermal stability resulted from a slower increase in the leakage current (0.7 and 0.8-order) of OSCs based on modified ZnO ETLs relative to that of OSCs with ZnO-only ETL (2.3-order) during the 200 h of thermal stability test as depicted in Figure 5.20.
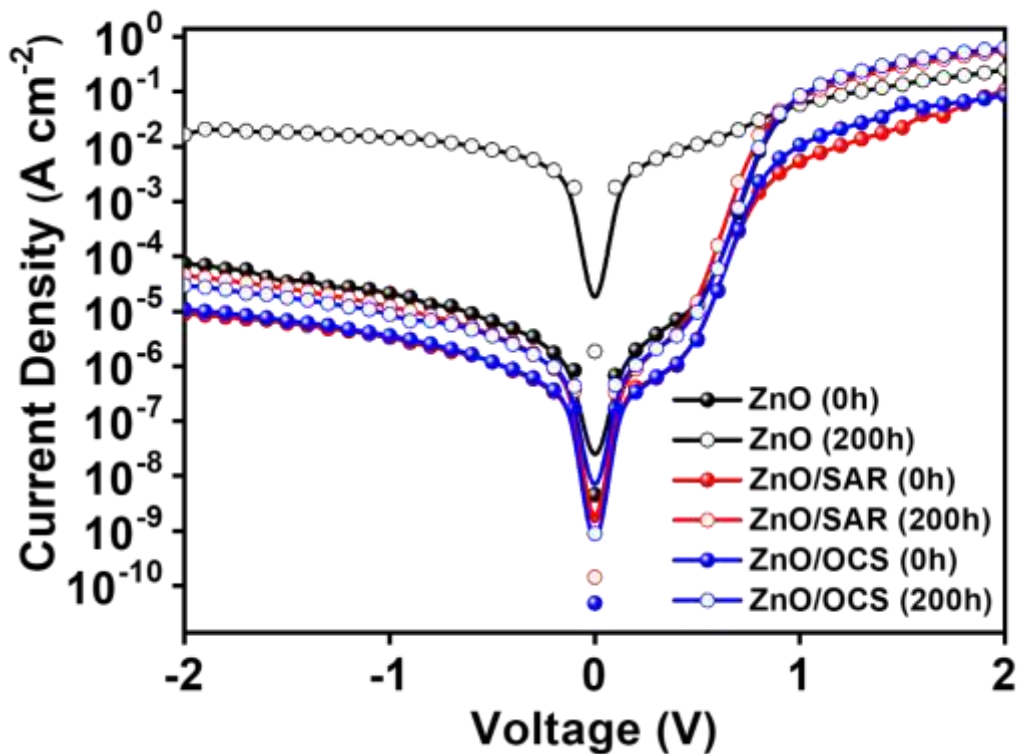
Figure 5.20: Evolution of dark current of OSCs during 200 hours of thermal ageing.

A further study on the morphological changes of the ZnO-modified ETL films was conducted by measuring the AFM images before and after 3 h of heating at 120 °C to establish the causes of the improved thermal stability. As shown in Figure 5.21 and Table 5.8, the ZnO-modified ETL films showed very small variations in surface roughness after heating at 120 °C/3 hours. In contrast, the ZnO-only ETL film displayed a large change in the RMS value under the same heating conditions. This result indicates that the cross-linked UV resins layers on ZnO formed a robust layer that was resistant to heat changes, accounting for the higher thermal stability.
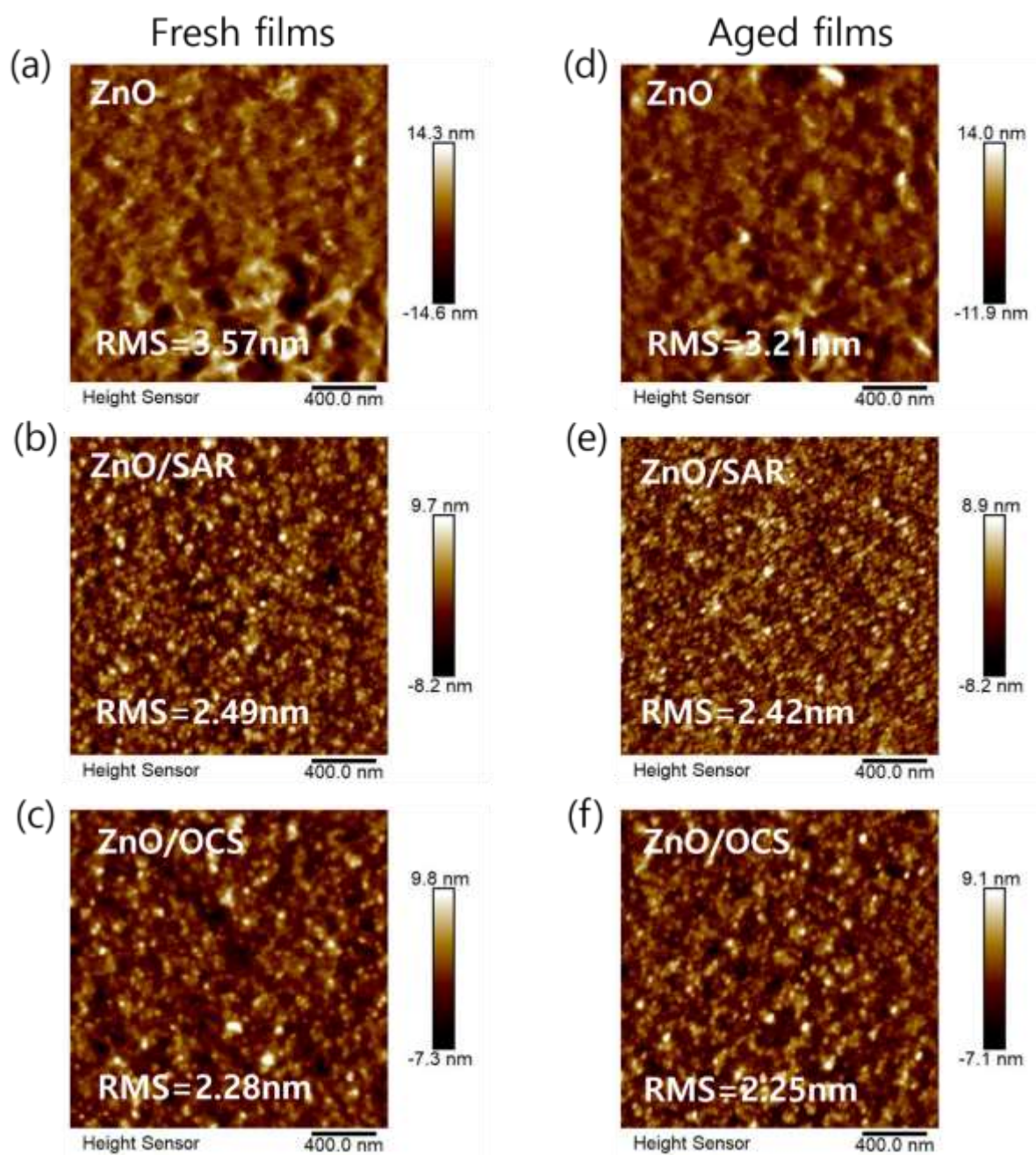
Figure 5.21: AFM height images of ZnO-based ETL films. (a-c) fresh and (d-f) Thermal aged at 120 °C for 3 hours.

Table 5. 8: Variation of the RMS values of different freshly prepared and aged films.

ETL films	Surface Roughness (RMS) (nm)		
	Fresh	Aged	ΔRMS
ZnO	3.57	3.21	0.36
ZnO/SAR	2.49	2.42	0.07
ZnO/OCS	2.28	2.25	0.03

5.3 General Applicability: The Effect of Modifying SnO₂ ETL with Ultraviolet Resins

5.3.1 Properties of SnO₂ Nanoparticles

SnO_2 is a metal oxide used as an ETL in OSCs as a replacement for ZnO because of its wider bandgap, which makes it less sensitive to UV light, and thus, lower photocatalytic activity (Jiang *et al.*, 2019). In this work, this property of SnO_2 was demonstrated by calculating its bandgap and investigating its effect on the photodegradation and photobleaching of Y6-BO, as presented in Figure 5.22 (a-d).
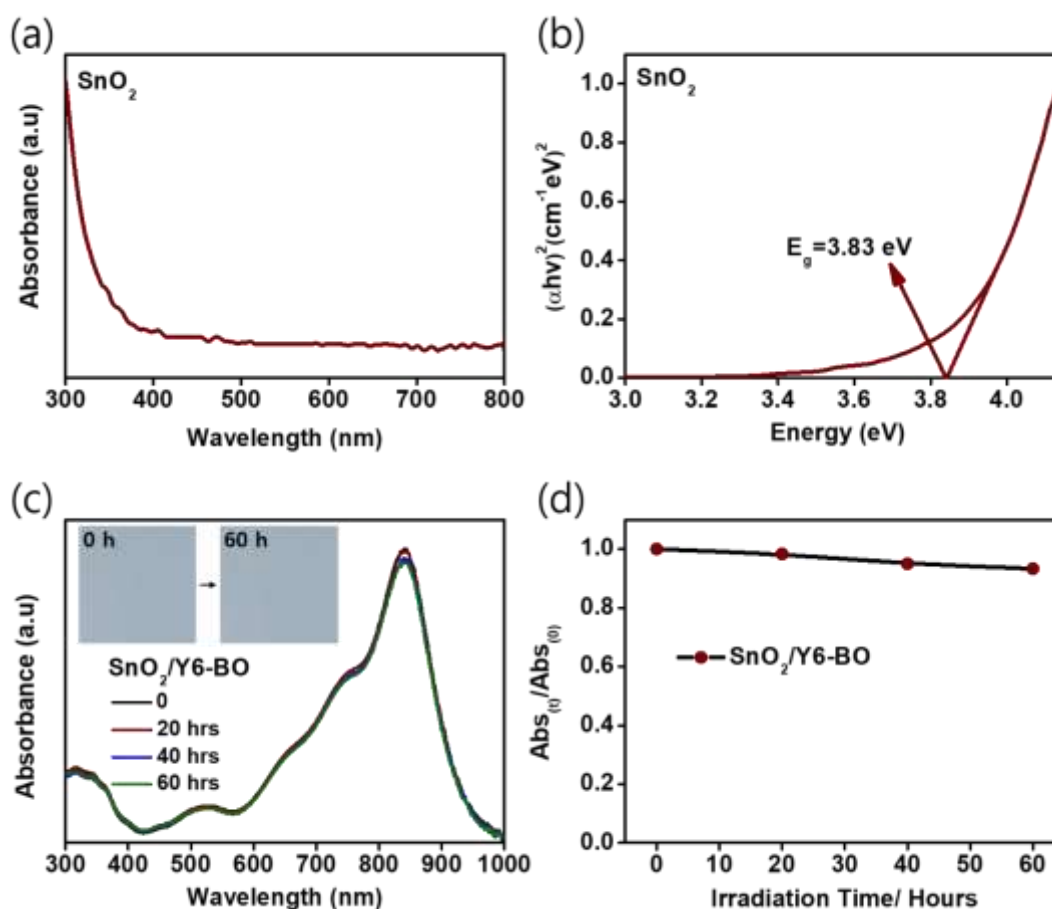
Figure 5.22: (a) Absorption spectra, (b) Tauc plot calculated from the absorption spectra, (c) Absorption curves of the Y6-BO films coated on SnO₂ with various irradiation time, and (d) The variations of the absorption intensities of Y6-BO films with UV light irradiation time.

The bandgap of SnO₂ film was found to be 3.83 eV, which is wider than 3.28 eV calculated for ZnO. After illuminating the Y6-BO film coated on SnO₂ for 60 h, the film showed no signs of photobleaching because the colour of the Y6-BO film was maintained (Figure 5.22 (c)). Also, as shown in Figure 5.22 (c), the absorption intensities of Y6-BO slightly decreased within 60 hours of illumination, further proving that SnO₂ has less photocatalytic activity under UV light illumination and could serve as a better alternative to photocatalytic ZnO as an ETL in inverted OSCs.

5.3.2 Interfacial Modification Properties of UV Resins on SnO₂

To test the effectiveness of UV resins, the effects of SAR or OCS resins on the interfacial properties of SnO_2 were investigated. As shown in Figure 5.23, the modification of SnO_2 with SAR and OCS resins resulted in enhanced absorption intensity, which might have resulted from the increased electron concentration from the UV resins. More importantly, the UV resins increased the optical transmittance of SnO_2 in the wavelength region 450-800 nm. This enhancement in optical transmittance is beneficial for charge transport materials to be able to permit the passage of light to the photoactive layer, resulting in more photon utilisation and improved photovoltaic performance of solar cells (Li *et al.*, 2023c)
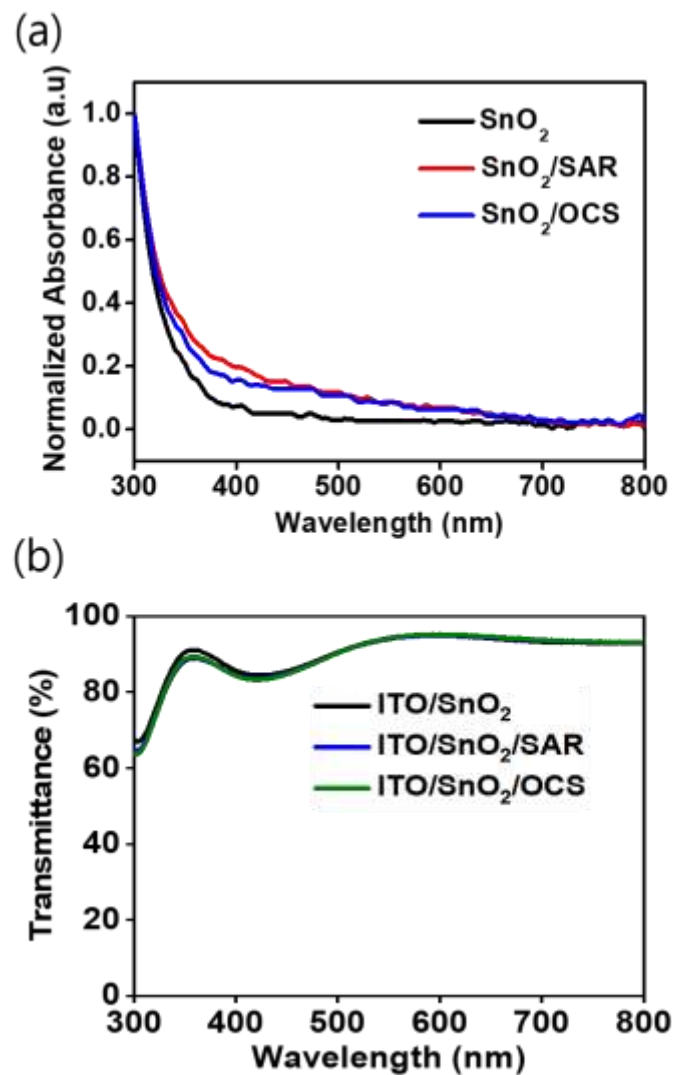
Figure 5.23: Absorption and transmittance curves of SnO_2-modified ETLs. (a) Absorption and (b) Optical transmittance.

The variations in the surface wettability of the SnO_2 ETL films modified with SAR and OCS resins were investigated using contact angle measurements. The measured water and diiodomethane contact angles are shown in Figure 5.24. The SnO_2 nanoparticles showed a small θ_w of 9.3°. In contrast, the SnO_2/SAR and SnO_2/OCS films exhibited θ_w of 40.8° and 31.8°, respectively.
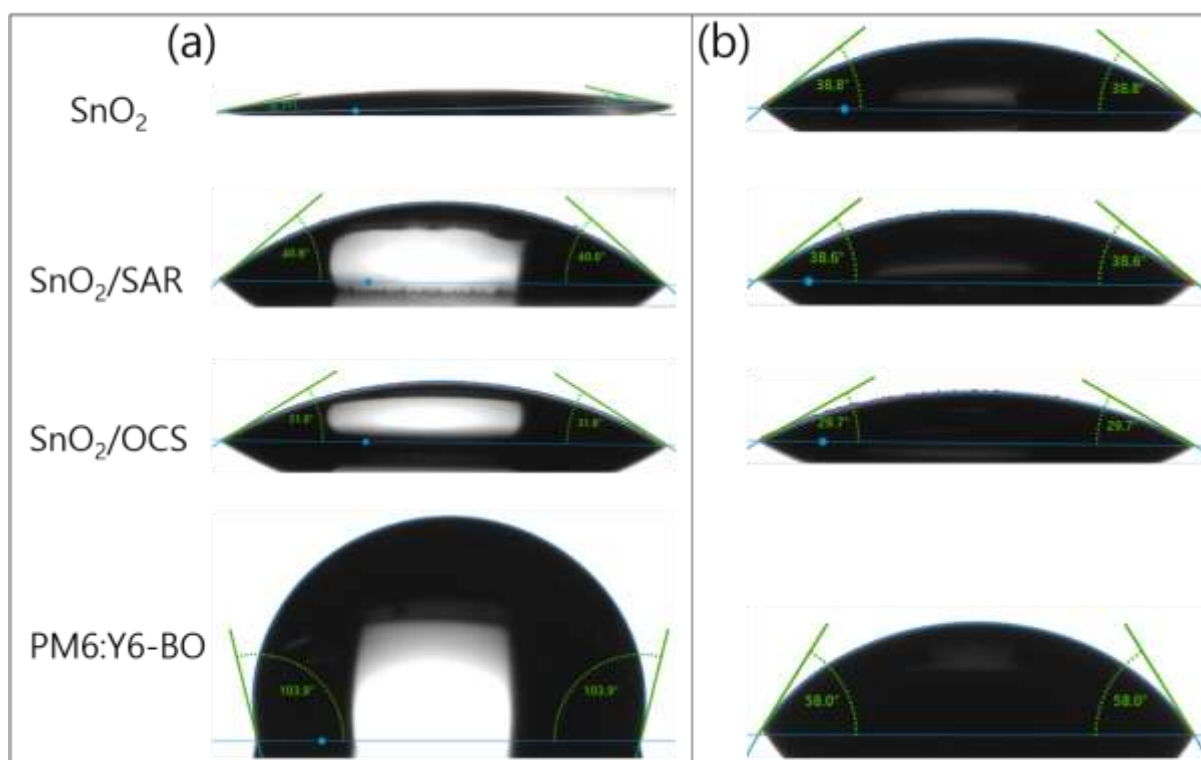
Figure 5.24: θ_C of (a) Water and (b) Diiodomethane on various ETLs and active layer films.

The surface free energies were calculated for the corresponding films, and are presented in Table 5.9. A decrease in the surface energy of SnO_2 upon modification with SAR and OCS resins was observed from 72.5 mJ m^{-2} to 67.5 mJ m^{-2} and 59.6 mJ m^{-2}, respectively. Compared with the surface free energy of the photoactive layer material (29.7 mJ m^{-2}), the SnO_2-modified films showed more similarity than the pristine SnO_2 films. The closer similarity of the films' θ_w and γ based on SnO_2-modified ETLs with that of the Y6-BO demonstrates enhanced contact at the SnO_2/PM6:Y6-BO interface compared to the case of unmodified SnO_2.

Table 5. 9: Summarised θ_w, θ_{dim}, and the corresponding γ of SnO_2, SnO_2/SAR, and SnO_2/OCS films.

Films	θ_{water} (°)	$\theta_{diiodomethane}$ (°)	Surface free energy, γ (mJ m^{-2})
SnO_2	9.70	38.80	72.49
SnO_2/SAR	40.80	38.60	67.53
SnO_2/OCS	31.80	29.70	59.62
PM6:Y6-BO	104.3	58.60	29.74

The work function is an essential parameter when it comes to balancing the ETL and the active layer energy levels to ensure efficient charge extraction. In this study, the effect of UV resins on the work function of SnO_2 was studied as presented in Figure 5.25. The work function of SnO_2 was computed as 4.0 eV, similar to the one previously reported (Huang *et al.*, 2020b). Upon modifying SnO_2 with SAR and OCS resins, the WF was reduced to 3.98 and 3.86 eV, respectively. A decrease in the WF of SnO_2 can be attributed to the creation of surface dipoles, by the UV resins' amine groups (Zhu *et al.*, 2019).
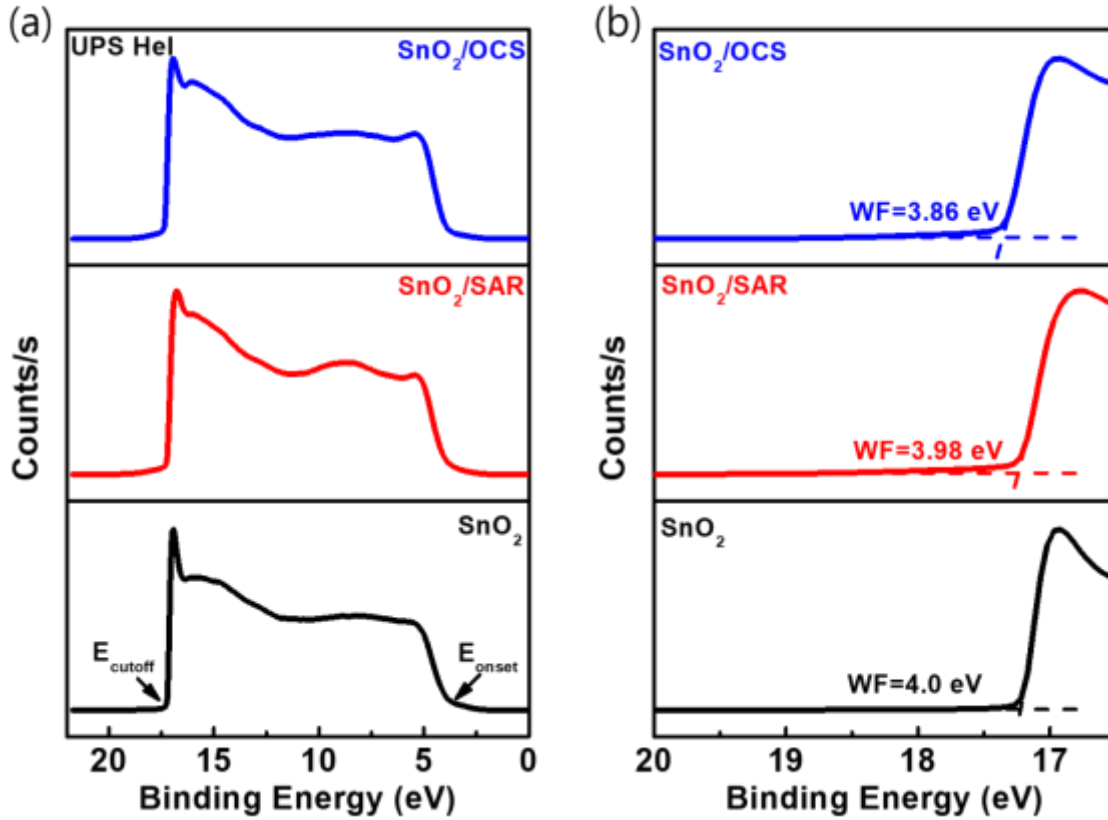
Figure 5.25: (a) Full UPS scan and (b) Secondary electron cutoff spectra of various ETL films.

A decrease in WF balances the electron and hole potential barriers, resulting in reduced charge recombination and improved charge transfer in OSCs (Wu *et al.*, 2023). Additionally, decreased WF results in upshifting of the SnO_2's LUMO level to bring forth a match with that of Y6-BO, as shown in Figure 5.26. This matching of the energy levels results in effective charge extraction from the photoactive layer by the ETL, improving photovoltaic performance (Suo *et al.*, 2023).
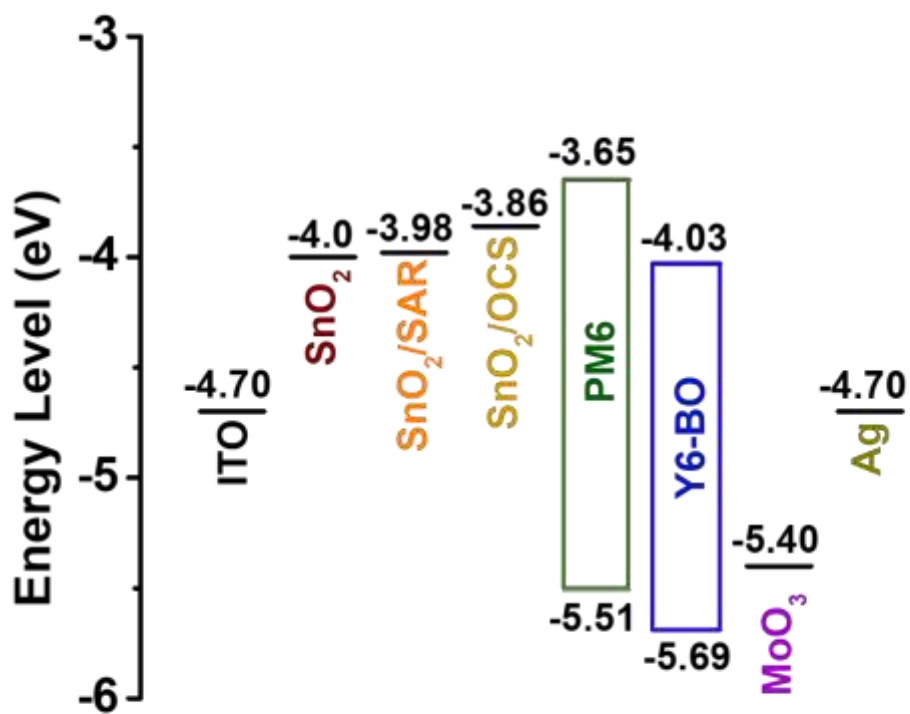
Figure 5.26: Energy level alignment of various layers of iOSCs. The LUMO and HOMO values of the other materials were obtained from the literature (Abbas *et al.*, 2022; Suo *et al.*, 2023).

An XPS study was conducted to determine the effect of modifying SnO_2 with SAR and OCS on surface defects. The full XPS spectra of various ETL films are depicted in Figure 5.27.
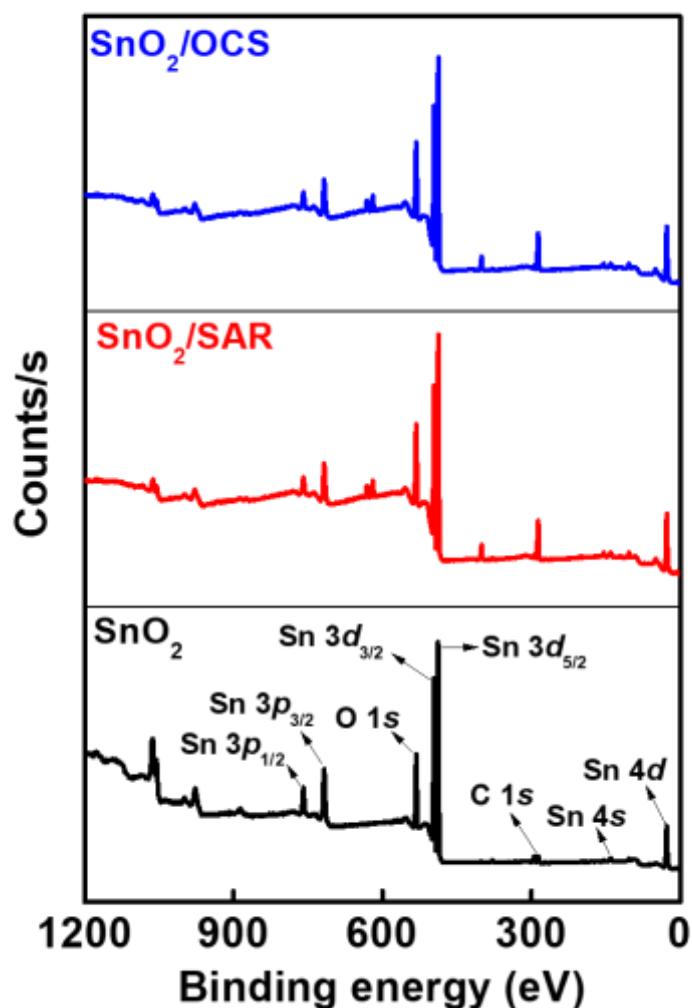
Figure 5.27: Full XPS spectra corresponding to various ETL films.

The change in chemical bonding on the SnO_2 film upon SAR and OCS modification, was studied from the Sn $3d$ core-level electrons. Figure 5.28 (a) shows that the Sn $3d$ spectra had two peaks at 488 and 496 eV. These peaks correspond precisely to the Sn $3d_{5/2}$ and Sn $3d_{3/2}$ core electrons and signify electron interactions or concentrations in SnO_2. These peaks shift toward the lower binding energy by 0.17 eV and 0.13 eV, respectively, upon SAR and OCS modification. This shift towards the lower binding energy demonstrates an enhanced concentration of tin ions, probably due to charge transfer from the SAR and OCS resins, thus showing that electronic interactions occurred between SnO_2 and UV resins (Hu *et al.*, 2020).

79

Moreover, the O 1s XPS spectra were deconvoluted into individual peaks, as presented in Figure 5.28 (b). The SnO$_2$ O 1s spectra had two peaks located at 530 and 532 eV binding energy. These peaks correspond to Sn-O bonds and oxygen vacancies (V$_o$), respectively (Gao *et al.*, 2022). The oxygen vacancies form a part of the surface defects on SnO$_2$.
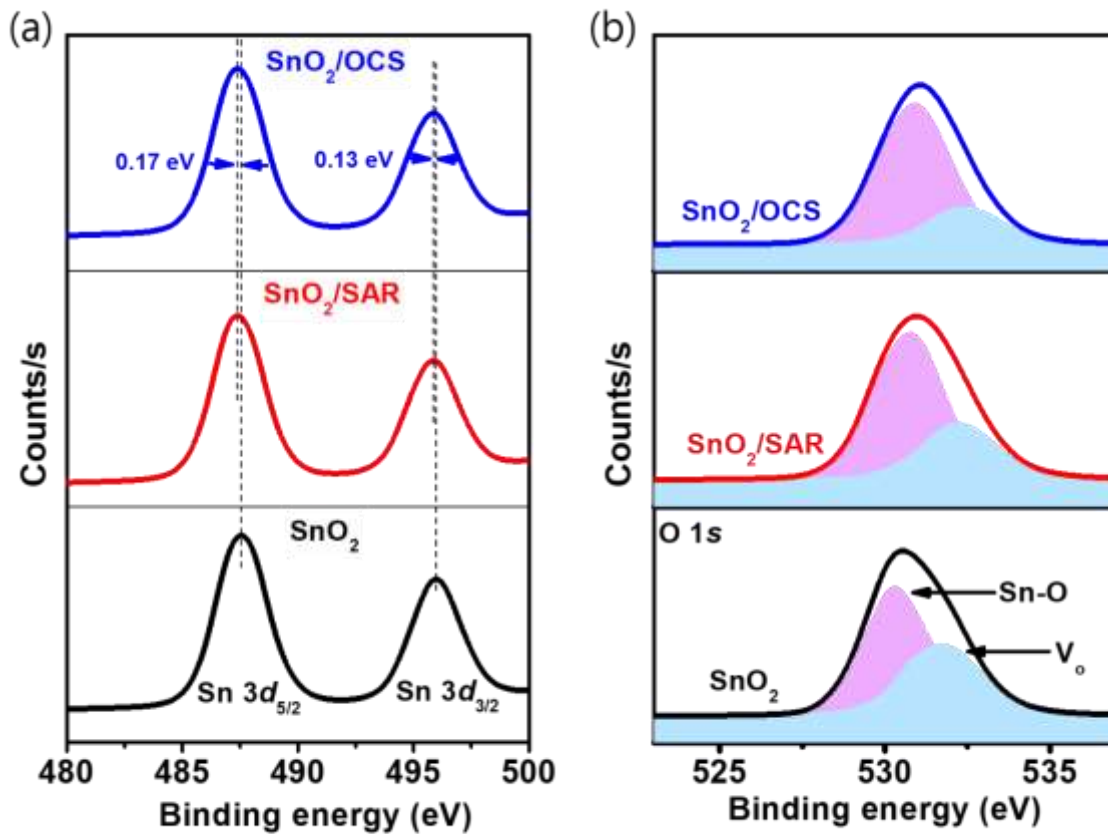
Figure 5.28: Electron counts versus binding energy of SnO$_2$, SnO$_2$/SAR, and SnO$_2$/OCS films. (a) Sn 3d XPS spectra, and (b) Deconvoluted O 1s XPS spectra.

To establish the changes in the surface defects when SnO$_2$ was modified with UV resins, the V$_o$/Sn-O peak intensity ratios were determined, as shown in Table 5.10.

Table 5. 10: The Sn-O and V_o peak intensities, and the V_o/Sn-O ratios of various ETL films.

Films	Sn-O	V_o	V_o/Sn-O
SnO_2	398443.69	221363.894	0.56
SnO_2/SAR	1163709.68	456578.947	0.39
SnO_2/OCS	1433262.59	388539.898	0.27

The calculated V_o/Sn-O ratio corresponding to bare SnO_2 film was 0.56. In contrast, the V_o/Sn-O ratio corresponding to the SnO_2/SAR and SnO_2/OCS ETLs was 0.39 and 0.27, respectively. A reduced V_o/Sn-O ratio for the SnO_2-modified ETLs implies fewer surface defects (Gao *et al.*, 2022). A photoluminescence analysis was done to further establish the effect of SAR and OCS as SnO_2 modification materials on surface defects, as depicted in Figure 5.29. The photoluminescence emission of SnO_2 in the visible region was ascribed to surface defects (Divya *et al.*, 2021). Generally, four visible photoluminescence emission peaks are located at wavelengths of 407, 447, 483, and 530 nm. The peak observed at 407 nm corresponds to luminescent centres originating from dangling bonds and interstitial tin (Divya *et al.*, 2021). At 483 nm, the emission peak was associated with V_o, whereas the broad emission peak at 530 nm was associated with surface traps (Divya *et al.*, 2021). There was a drop in the peak intensity of the photoluminescence emission when SnO_2 was modified with UV resins. The specific values of the photoluminescence intensity of the various ETL films are presented in Table 5.11. The decrease in the photoluminescence peak intensities of SnO_2 upon SAR and OCS modification resulted in reduced surface defects. Minimising the surface defects on SnO_2 is beneficial for forming a better interface with the photoactive layer.
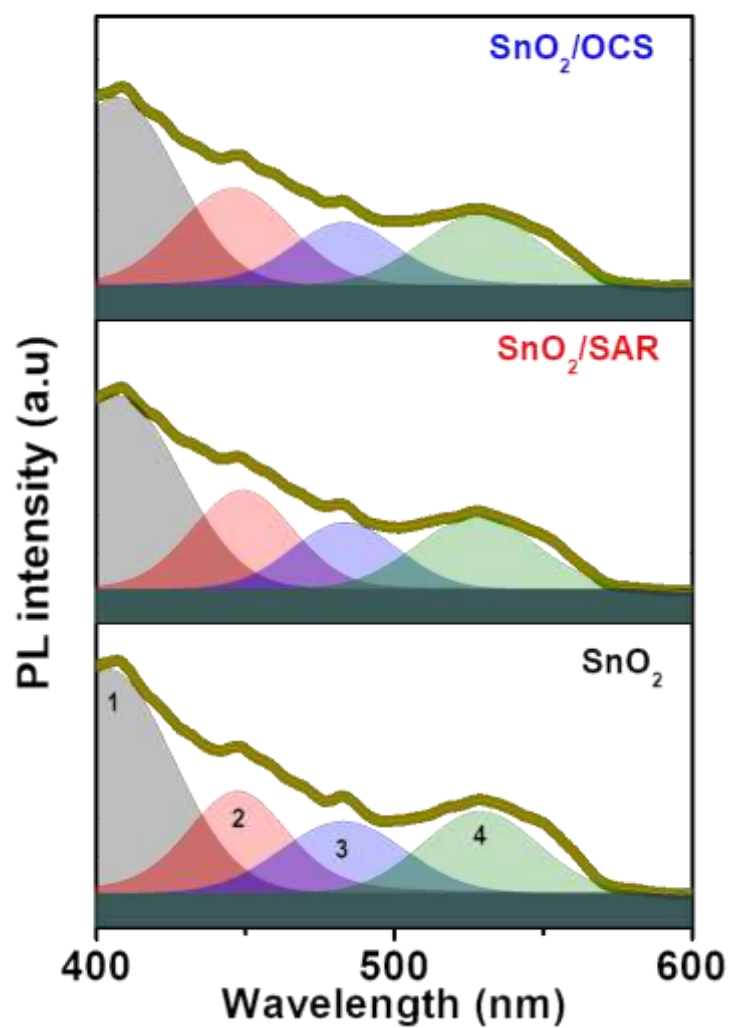
Figure 5.29: Photoluminescence spectra corresponding to various ETL films.

Table 5. 11: Summary of the photoluminescence peak intensities of various ETL films.

Films	Peak 1	Peak 2	Peak 3	Peak 4
SnO_2	82.85	37.83	26.74	30.33
SnO_2/SAR	71.90	36.72	24.70	26.88
SnO_2/OCS	69.72	36.28	23.46	26.43

5.3.3 Photovoltaic Performance of OSC Devices Based on SnO₂ ETLs

The effect of modifying the SnO_2 ETL with UV resins on photovoltaic performance was investigated. Before modifying the SnO_2 ETL, the annealing temperature, annealing time, and concentration were optimised, as shown in Table 5.12 and Figure 5.30. The optimal PCE of the OSCs was obtained at 1:6 v/v of SnO_2:H_2O and 170 °C thermal annealing for 10 minutes.

Table 5. 12: Optimisation of SnO_2 ETL based on thermal annealing temperatures, thermal annealing time, and concentration.

ETL	Temperature (°C) for 10 minutes	V_{oc} [V]	J_{sc} [mA cm^{-2}]	FF [%]	PCE [%]
SnO₂:H₂O (1:3)	110	0.80	23.10	67.81	12.60
	130	0.81	23.39	67.60	12.84
	150	0.82	23.80	66.93	12.99
	170	0.82	23.99	69.29	13.56
	200	0.81	23.73	63.44	12.15
	Time (minutes)				
SnO₂:H₂O (1:3)	10	0.82	23.99	62.29	13.56
	30	0.81	23.13	6712	12.60
	40	0.81	22.62	65.10	11.92
	50	0.81	22.45	64.28	11.70
	Concentration (v/v)				
SnO₂:H₂O	1:3	0.82	23.99	62.29	13.56
	1:6	0.81	24.46	69.38	13.76
	1:9	0.81	24.22	64.66	12.73
	1:12	0.80	24.17	62.58	12.17
	1:15	0.77	24.05	60.79	11.21
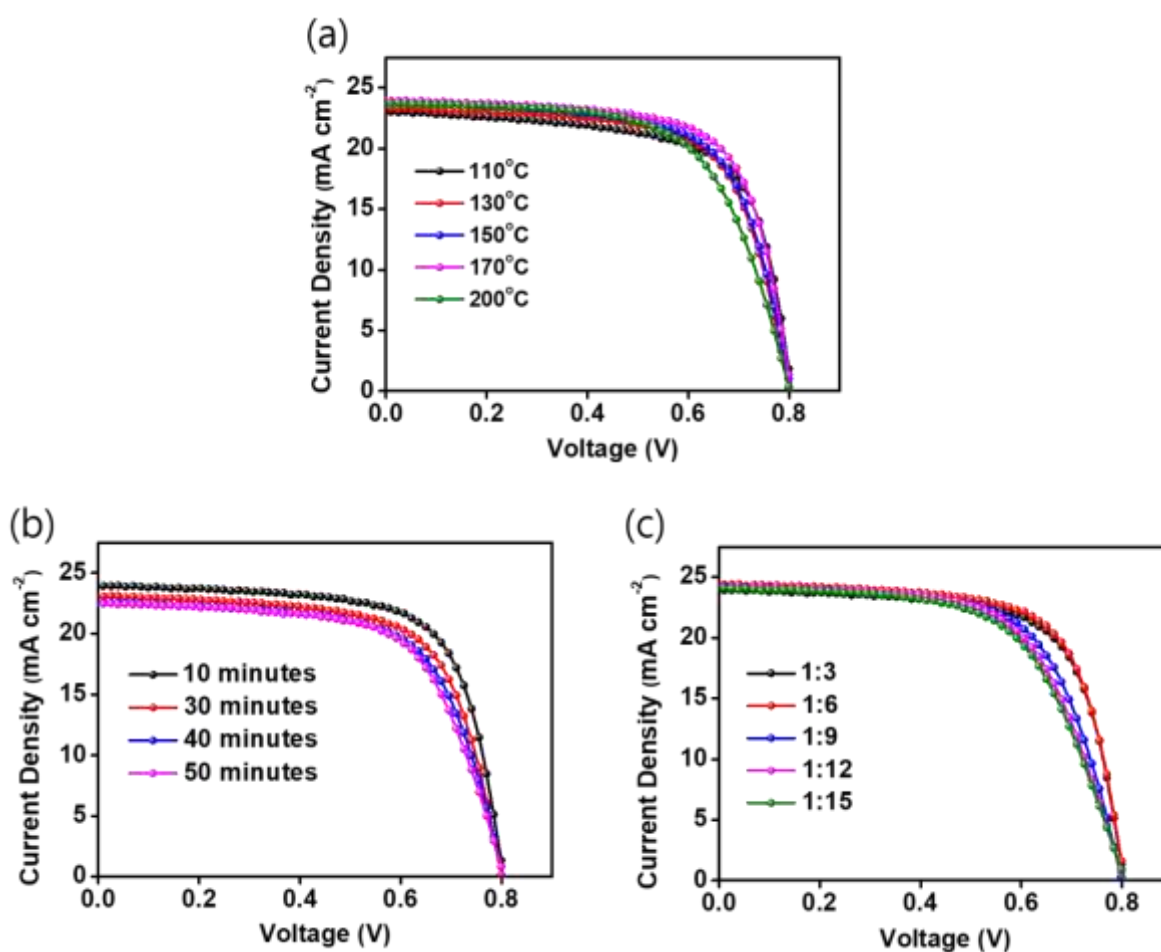
Figure 5.30: The J-V characteristics of OSC devices with SnO_2 ETL optimised under (a) thermal post-treatment, (b) thermal treatment time, and (c) Concentration (dilution ratio of SnO_2 to water).

Based on these optimal conditions, OSCs with SnO_2 modified with SAR and OCS resins were fabricated, and the corresponding photovoltaic performance characteristics are listed in Table 5.13.

Table 5. 13: The photovoltaic performance characteristics of OSCs with SnO_2-modified ETLs. In brackets are the statistical values of 6 OSC devices.

ETLs	V_{oc} (V)	J_{sc} (mA cm^{-2})	FF (%)	PCE (%)
SnO_2	0.81	24.46	69.38	13.76 (13.50±0.20)
SnO_2/SAR	0.81	24.57	72.61	14.41 (14.23±0.15)
SnO_2/OCS	0.82	24.52	72.21	14.43 (14.19±0.18)

The PCE of SnO_2 ETL-based OSCs was 13.76%. This PCE was increased to 14.41% and 14.43% by modifying SnO_2 with SAR and OCS resins, respectively, with simultaneously improved V_{oc}, J_{sc}, and FF. Table 5.14 compares the photovoltaic performance of OSCs manufactured in this study to those of OSCs previously reported based on SnO_2 ETLs. It is seen from this table that our work presented the highest PCE of OSCs processed from a non-halogenated solvent.

Table 5. 14: PCE of NFA-based iOSCs with SnO_2 nanoparticles as ETLs reported in the literature.

Active layer	Solvent	ETLs	PCE (%)	Year	Reference
PBDB-T-2F:Y6	CF+0.5vol% CN	SnO_2	12.88	2019	(Bai *et al.*, 2019)
PBDB-T: ITIC	Cb+0.5% DIO	SnO_2	10.77	2019	(Sun *et al.*, 2019)
J71:ITIC	CF	SnO_2	9.04	2019	(Di Carlo Rasi *et al.*, 2019)
PM6:IT-4F	Cb+0.5% DIO	SnO_2	14.10	2019	(Jiang *et*

					al., 2019)
PM6:Y6	CF+0.5vol% CN	SnO_2	16.10	2020	(Bai *et al.*, 2020)
PM6:Y6	CF+0.5vol% CN	n-SnO_2/InP/ZnS QDs	15.22	2020	(Peng *et al.*, 2020)
PCE10:IEICO-4F	Cb+3vol% CN	SnO_2	10.53	2020	(Jiang *et al.*, 2020)
PM6:Y6: IDIC	CF+0.5vol% CN	SnO_2-PEO	15.90	2020	(Hu *et al.*, 2020)
PBDB-T-SF:IT-4F	Cb+0.5% DIO	SnO_2/PeNWs	10.72	2020	(Zhao *et al.*, 2020)
PBDB-TF:IT-4F	Cb+0.5% DIO	EA - SnO_2	12.45	2020	(Huang *et al.*, 2020b)
PM6:Y6	CF+0.5vol% CN	SnO_2/PDINO	14.90	2021	(Kong *et al.*, 2021)
PM6:Y6	CF+0.5vol% CN	SnO_2/DMAEMA	15.45	2021	(Fu *et al.*, 2021)
PM6:Y6	CF+0.5vol% CN	Co^{2+}- SnO_2	15.30	2021	(Zhang *et al.*, 2021)
PM6:PB2F:BTP-eC9	CF+0.5vol%DIO	SnO_2/1-DPAQ	18.10	2022	(Yu *et al.*, 2022)
PM7:IT-4F	Xylene	SnO_2/ZnO	12.91	2022	(Lin and Dai, 2022)
PM6:BTP-4F-12	Xylene	SnO_2/CNC-a	13.10	2022	(Niazi *et al.*, 2022)
PM6:BTP-eC9	CF+0.5vol% CN	SnO_2:PAS	17.12	2022	(Gao *et al.*, 2022)
PM6:Y6	CF+0.5vol% CN	SnO_2/PDIN-H	10.60	2022	(Munir *et al.*, 2022)

TPD-3F:IT-4F	Xylene:DIO:DPE	SnO_2	11.70	2023	(Di Mario *et al.*, 2023b)
PM6:L8-BO	CF+0.25% DIO	SnO_2	16.03	2023	(Di Mario *et al.*, 2023a)
PM6:PC71BM:Y6	CF+CN	SnO_2	16.70	2023	(Liu *et al.*, 2023)
TPD-3F:IT-4F	Xylene	SnO_2	12.82	2023	(Romero *et al.*, 2023)
PM6:L8-BO	CF+0.25vol%DIO	SnO_2	16.26	2023	(Romero *et al.*, 2023)
PM6:L8-BO	CF+0.5vol%DIO	SnO_2/Phen-NaDPO	18.31	2023	(Wu *et al.*, 2023)
PM6:L8-BO	CF+DIO	SnO_2/NMA	18.33	2023	(Suo *et al.*, 2023)
PM6:Y6-BO	Xylene	SnO_2/OCS	14.43	2023	This work

The J-V and EQE curves of OSCs with SnO_2-based ETLs are presented in Figure 5.31. As observed in Figure 5.31, the OSC device with the SnO_2-only ETL display a lower J-V curve than those based on SnO_2-modified ETLs. Moreover, the EQE response in the wavelength range 380-830 nm was improved for OSC devices based on SnO_2-modified ETLs, demonstrating that enhanced photon-to-electron conversion resulted to the J_{sc} and FF improvement. This EQE result corroborates with the enhanced transmittance observed.
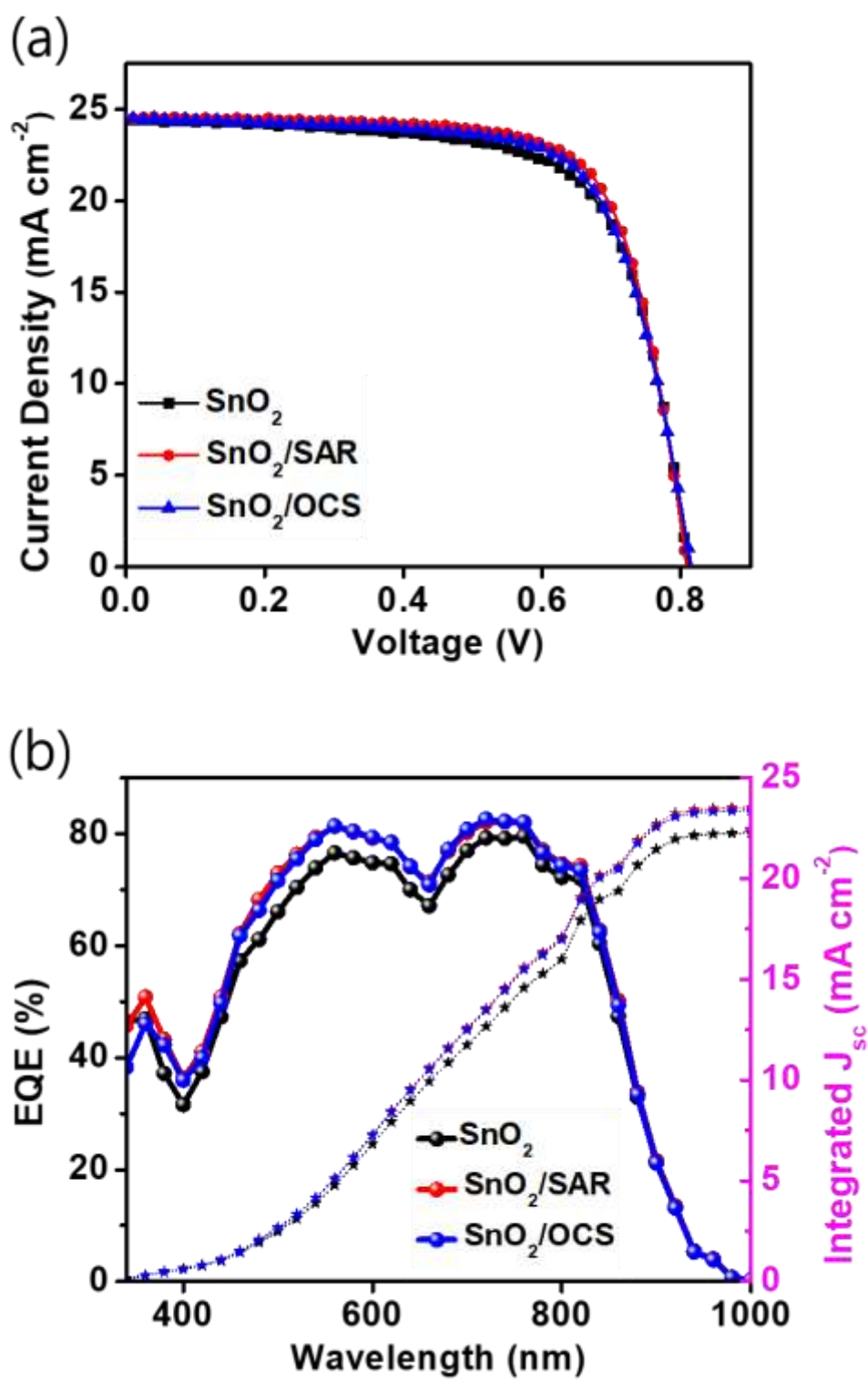
Figure 5.31: (a) The J-V curves and (b) EQE (left y-axis) and integrated current density (right y-axis) curves of OSCs with various ETLs.

5.3.4 Charge Dissociation and Recombination

The J_{ph}-V_{eff} curves were studied to establish the effect of modifying SnO_2 with SAR and OCS resins, as presented in Figure 5.32 (a). The P (E, T) of the OSCs with SnO_2 ETL was 96%, while that of OSCs with modified SnO_2 ETLs was 97.1%. The higher exciton dissociation probability obtained in the SnO_2-modified OSCs implies improved charge extraction efficiency, thus contributing to enhanced photovoltaic performance. The effect of modifying SnO_2 on the charge carrier recombination dynamics was first investigated by measuring the V_{oc} and J_{sc} versus P_{light} curves, as presented in Figure 5.32 (b, c). The slopes of the V_{oc} and J_{sc} vs. light intensity curves (n and α) provide estimates of trap-assisted and bimolecular recombination in OSCs, respectively. The closer the n value is to 2kT/q, the more dominant the trap-assisted recombination (Cai *et al.*, 2021), whereas the higher the α value is, the lesser the bimolecular recombination (Hwang *et al.*, 2019). It can be seen that upon modifying SnO_2 with SAR and OCS resins, both trap-assisted and bimolecular recombination were suppressed, which accounts for improved PCE. Further study on the recombination dynamics was conducted using electrochemical impedance spectroscopy, as shown in Figure 5.32 (d). The EIS curves were fitted with the circuit model discussed in the methods section to obtain the OSCs resistances, as detailed in Table 5.15. The series resistance of OSCs decreased from 29.3 Ω to 17.5 Ω and 16.9 Ω upon modifying SnO_2 with SAR and OCS resins, respectively. Similarly, the surface resistance reduced from 18.8 Ω to 14.2 Ω and 13.8 Ω upon modifying SnO_2 with SAR and OCS resins. The simultaneous decrease in the series and surface resistances of OSCs based on modified SnO_2 ETLs demonstrates reduced interfacial charge recombination (Li *et al.*, 2022b), which results in improved photovoltaic performance.
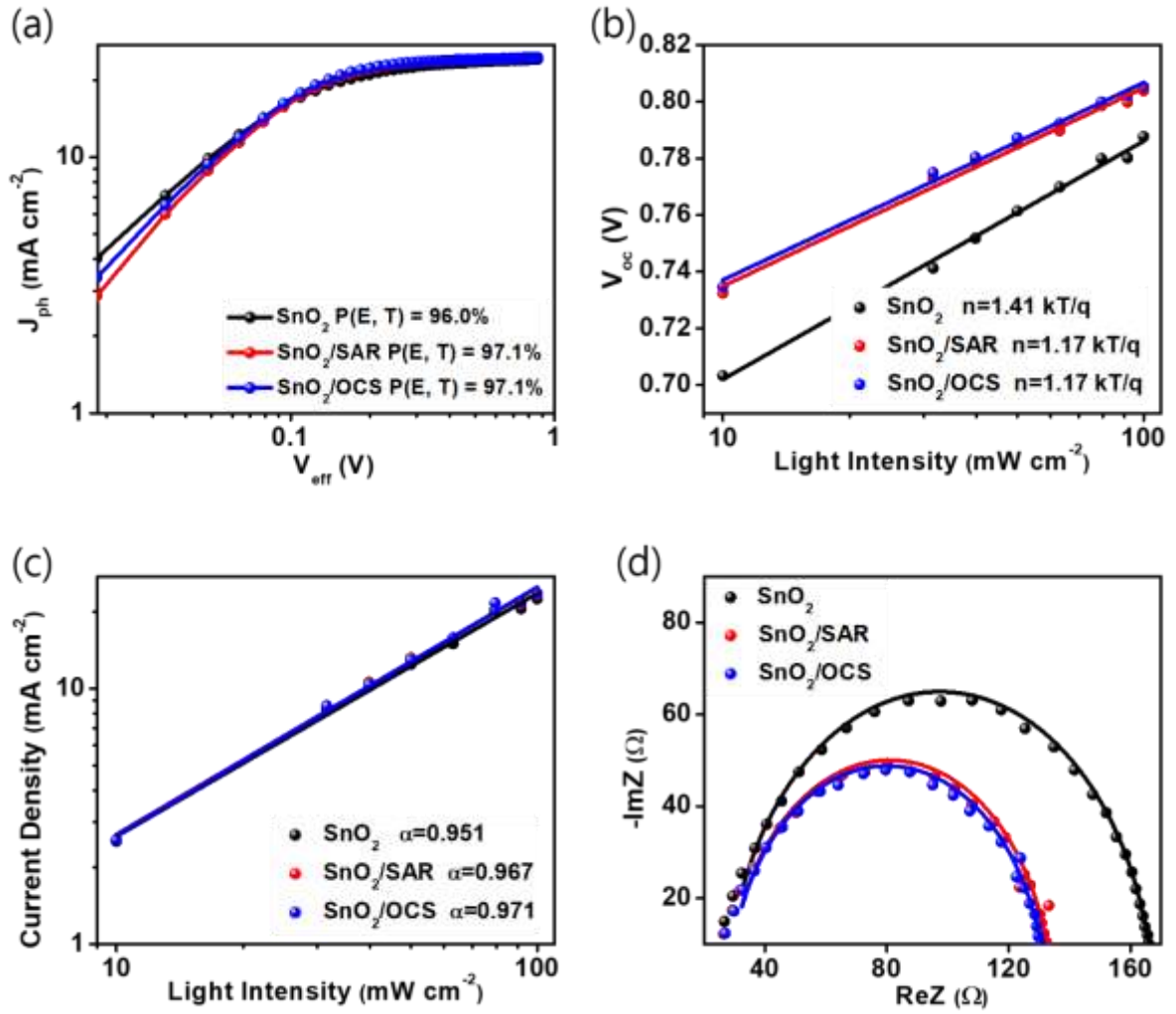
Figure 5.32: Plots of OSCs with various ETLs. (a) Photocurrent curves, (b) V_{oc}-P_{light} curves, (c) J_{sc}-P_{light} curves, and (d) Electrochemical impedance spectra.

Table 5. 15: The series and surface resistance of OSCs with various ETLs.

ETLs	R_{series} (Ω)	$R_{surface}$ (Ω)
SnO_2	29.316	18.811
SnO_2/SAR	17.548	14.250
SnO_2/OCS	16.881	13.822

5.3.5 Charge Transport

Further study was conducted on the charge transport behaviour using the SCLC method. The ITO/ETLs/PM6:Y6-BO/SnO$_2$/Ag devices were constructed to study the effect of modifying SnO$_2$ with SAR and OCS resins on electron mobility and trap density. The dark J-V curves are presented in Figure 5.33. The calculated electron mobility of SnO$_2$-only based devices was 4.12 $\times 10^{-4}$ cm^{2}V^{-1}s^{-1}, whereas the electron mobilities of the SnO$_2$/SAR and SnO$_2$/OCS based devices were 4.58 $\times 10^{-4}$ cm^{2}V^{-1}s^{-1} and 4.59 $\times 10^{-4}$ cm^{2}V^{-1}s^{-1}, respectively. Improved electron mobility through SnO$_2$ modification demonstrates improved charge transport in OSCs, thus improving photovoltaic performance. Additionally, the trap-filled voltages (V$_{TFL}$) were obtained as 0.285, 0.269, and 0.266 V for SnO$_2$, SnO$_2$/SAR, and SnO$_2$/OCS based devices, respectively, as depicted in Figure 5.33. The trap densities were obtained as 9.45×10^{15} cm^{-3}, 8.92×10^{15} cm^{-3}, and 8.82×10^{15} cm^{-3} for electron-only devices with SnO$_2$, SnO$_2$/SAR and SnO$_2$/OCS, respectively. It was observed that the trap density reduced after modifying SnO$_2$ ETL, which demonstrates lower trap recombination in OSCs. The modification of SnO$_2$ with SAR or OCS resins is speculated to have improved the crystallinity of the PM6:Y6-BO films thus reducing the trap densities. This further accounts for the enhanced J$_{sc}$ of OSCs with SnO$_2$-modified ETLs.
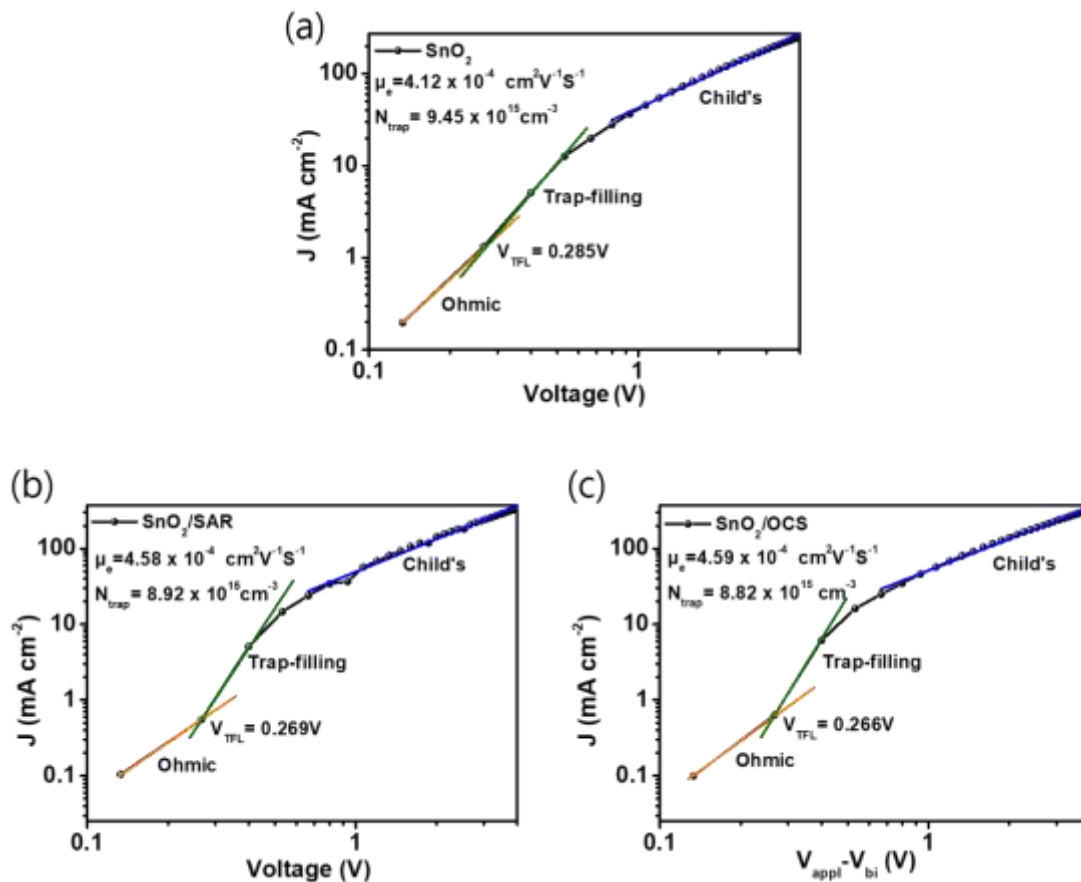
Figure 5.33: The three-segment J-V curves of the devices measured under dark conditions. ETLs used (a) SnO$_2$, (b) SnO$_2$/SAR, and (c) SnO$_2$/OCS.

5.3.6 Stability of OSCs

In addition to their photovoltaic performance, the stability is a critical factor for commercialisation of OSCs. In this regard, photostability was investigated to access the effects of SAR and OCS resin interlayers on the degradation of OSCs under light illumination for 450 h. The PCE evolution, J-V, and leakage current during 450 h of light irradiation is depicted in Figure 5.34.
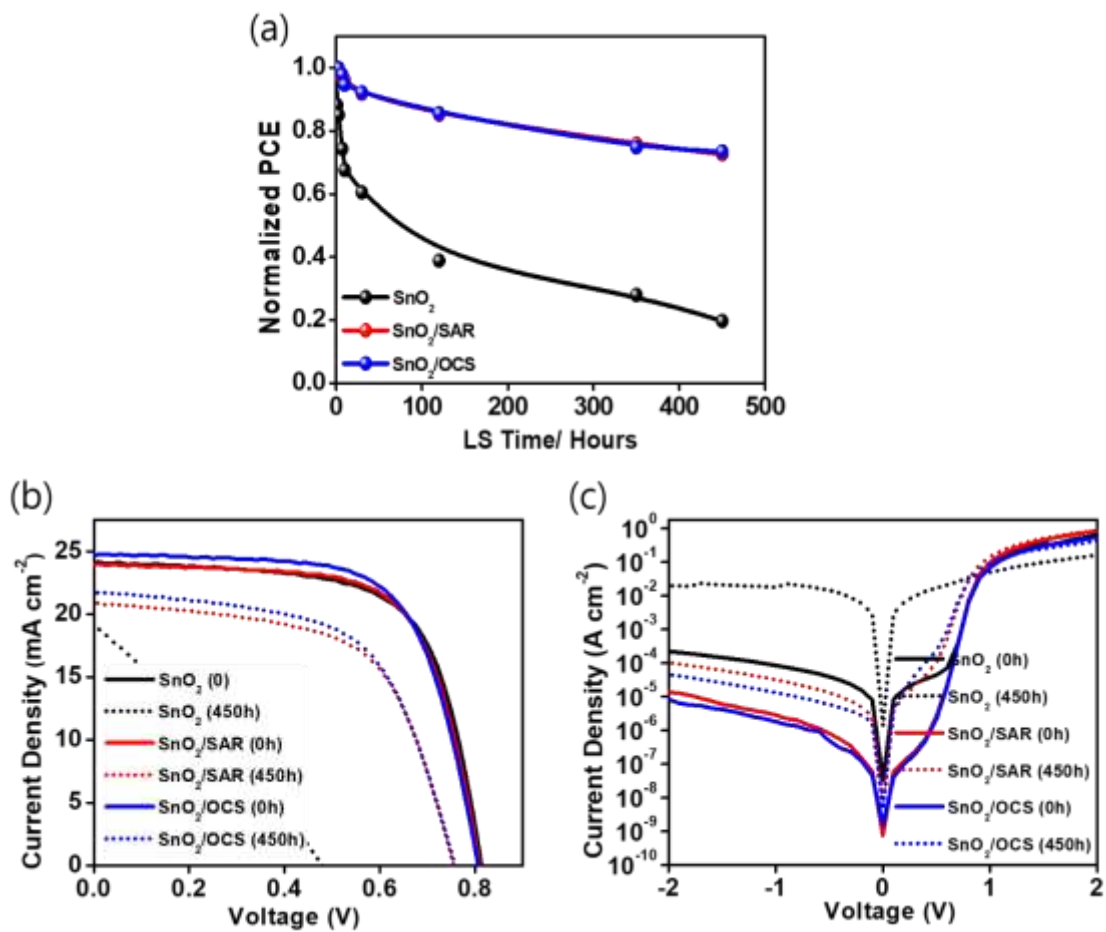
Figure 5.34: OSC devices with SnO_2, SnO_2 /SAR SnO_2 /OCS ETLs during 450 hours of light illumination. The evolution of (a) PCE, (b) J-V curves, and (c) Dark current density.

As depicted in Figure 5.34 (a), the PCE of OSCs with SnO_2-only ETL dropped to 20% within 450 h of light irradiation. Conversely, the PCE of OSC devices with SnO_2/SAR and SnO_2/OCS ETLs decreased to 73% after the same time. This shows that the SAR and OCS interlayers contribute to reducing the decomposition of OSCs under light. The J-V curves presented in

92

Figure 5.34 (b) demonstrate that during light illumination, the photovoltaic performance characteristics of OSCs with SnO_2/SAR or SnO_2/OCS ETLs were much retained compared to the case of OSCs with SnO_2-only ETLs. Figure 5.34 (c) shows that during the light ageing time, the leakage current at -2V of OSCs with SnO_2 ETL increased with a higher order of 2 relative to the OSCs with SnO_2/SAR and SnO_2/OCS ETLs whose leakage current increased by 0.71 and 0.63 order, respectively. A smaller order of increased leakage current of OSCs based on modified SnO_2 ETLs during light illumination demonstrates lower charge recombination and, hence, higher stability. The evolution of V_{oc}, J_{sc}, and FF during 450 h of light irradiation is presented in Figure 5.35, and the contribution of each photovoltaic performance parameter to the stable PCE is given in Table 5.16.
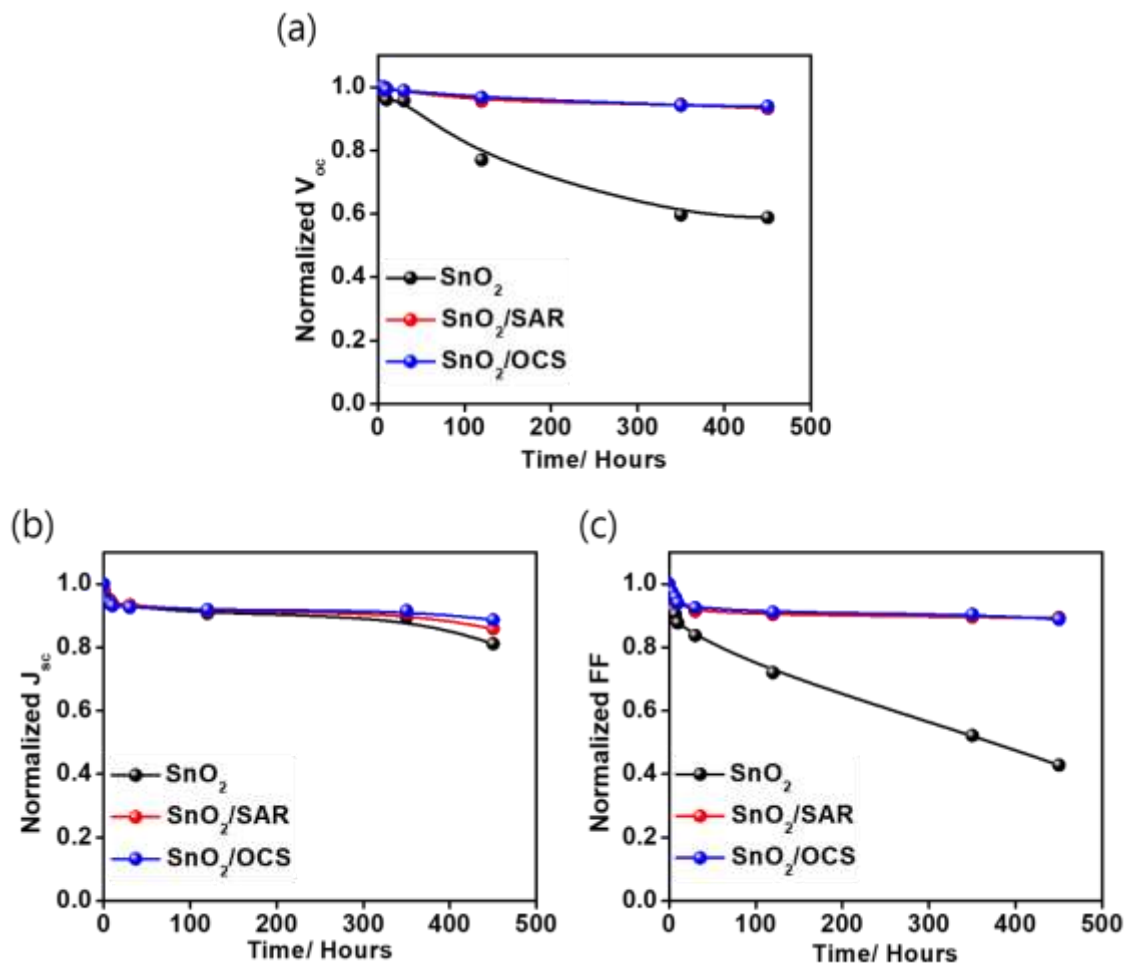
Figure 5.35: OSC devices with SnO_2, SnO_2/SAR, and SnO_2/OCS during the 450 hours of light illumination. The evolution of (a) V_{oc}, (b) J_{sc}, and (c) FF.

Table 5. 16: The detailed V_{oc}, J_{sc}, FF, and PCE drops of photo-aged OSC devices with SnO_2, SnO_2/SAR, and SnO_2/OCS ETLs.

ETLs	LS hours	V_{oc} (V)	V_{oc} Drop	J_{sc} (mA cm^{-2})	J_{sc} Drop	FF (%)	FF Drop	PCE (%)	PCE Drop
SnO_2	0	0.81		24.13		66.65		13.52	
	450	0.48	↓41%	19.12	↓21%	28.52	↓57%	2.61	↓80%
SnO_2/SAR	0	0.81		23.96		67.90		13.18	
	450	0.76	↓6%	20.87	↓13%	60.69	↓11%	9.56	↓27%
SnO_2/OCS	0	0.81		24.71		67.23		13.40	
	450	0.76	↓6%	21.74	↓12%	59.74	↓11%	9.84	↓27%

As shown in Figure 5.35 and Table 5.16, the key contribution to the high PCE of OSC devices with SnO_2-modified ETLs came from the high V_{oc} and FF retained during the light illumination time. The variations in the optical absorption of the photoactive material coated on SnO_2-modified ETLs upon light illumination for 3 h was investigated to establish the cause of the observed high photostability of OSC devices with SnO_2/SAR and SnO_2/OCS ETLs (see Figure 5.36). This investigation established whether the SAR and OCS interlayers contributed to mitigating the photodecomposition of individual PM6 and Y6-BO photoactive materials.
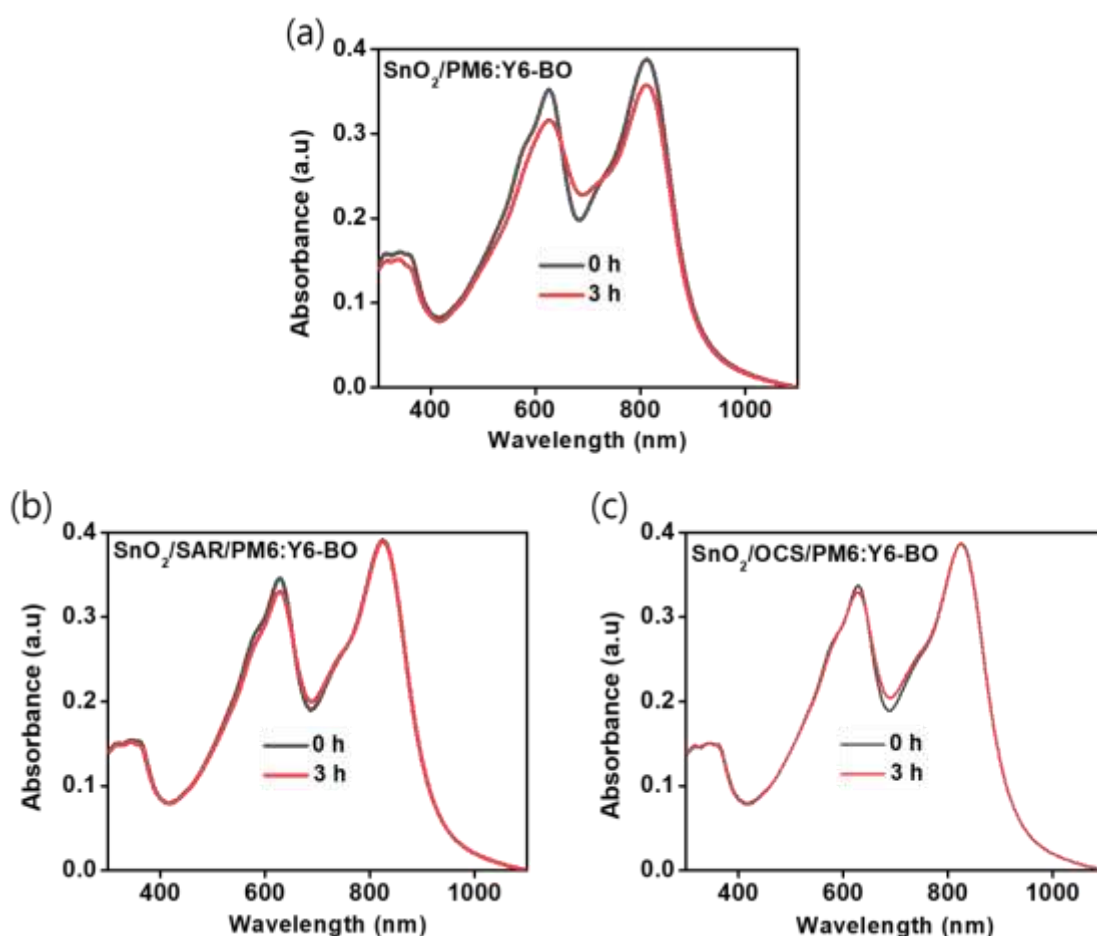
Figure 5.36: Absorption of fresh and photo-aged PM6:Y6-BO blends casted on (a) SnO_2, (b) SnO_2/SAR, and (c) SnO_2/OCS films.

As depicted in Figure 5.36, the PM6:Y6-BO film coated on SnO_2 showed a significant drop in the absorption intensities of PM6 and Y6-BO at 626 nm and 813 nm wavelengths, respectively, after 3 h of light illumination. In contrast, the absorption intensities of PM6:Y6-BO films casted on SAR and OCS resins showed a lesser decrease. Notably, the absorption peaks of Y6-BO at 813 nm remained nearly unchanged during 3 h of light illumination for the films casted on SnO_2/SAR and SnO_2/OCS. This proves that the photocatalytic activity of SnO_2, which might have resulted in the degradation of Y6-BO upon light illumination, was mitigated by inserting SAR or OCS resin interlayers at SnO_2/photoactive layer interface. This accounts for the observed improved light stability of the OSCs with the SnO_2/SAR and SnO_2/OCS ETLs.

Apart from the degradation of OSCs due to the light effect, degradation due to heat cannot be ignored. This is because, under practical operation in an outdoor environment, OSCs are subjected to direct sunlight, which generates heat. In this regard, a thermal stability test of OSCs based on modified SnO_2 was performed for a period of 200 h. The variations in the PCE, J-V curves, and dark current density during 200 h of thermal ageing are shown in Figure 5.37.
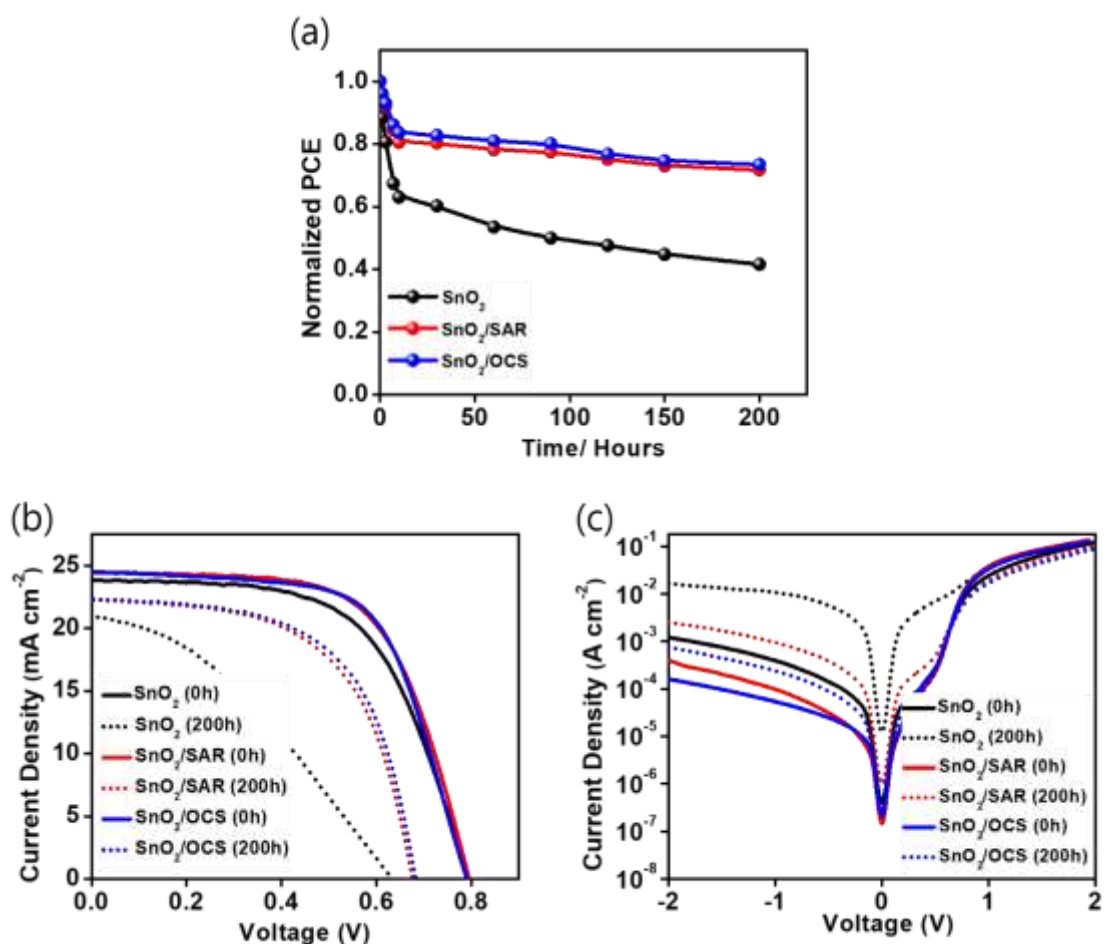
Figure 5.37: OSCs based on SnO_2, SnO_2/SAR, and SnO_2/OCS ETLs during 200 hours of thermal ageing. The variation of (a) PCE, (b) J-V, and (c) The dark current density.

As shown in Figure 5.37 (a), the PCE of the OSCs with the SnO_2 ETL dropped to 42% of the original value after 200 h of thermal ageing. Conversely, the PCE of the OSCs with SnO_2/SAR and SnO_2/OCS decreased to 72% and 73% of the initial value, respectively. This demonstrates that the modification of SnO_2 with SAR and OCS resins improves thermal stability. The J-V curves in Figure 5.37 (b) during 200 h of thermal ageing demonstrate that higher J_{sc} and V_{oc}

values were retained for the OSCs based on modified SnO_2, consistent with the higher thermal stability observed. The leakage currents of various thermally aged OSCs are shown in Figure 5.37 (c). After 200 hours of thermal ageing, the leakage current of SnO_2-based OSCs increased by one order, whereas the leakage current of OSCs with SnO_2/SAR and SnO_2/OCS increased by 0.8 and 0.6 orders, respectively. The lesser order of increase in the leakage current of the OSCs with SnO_2/SAR and SnO_2/OCS ETLs during the thermal ageing process demonstrates a lower charge recombination process, which leads to higher PCE. The evolution of V_{oc}, J_{sc}, and FF during the thermal ageing process is depicted in Figure 5.38, whereas the individual photovoltaic characteristics of the various thermally aged OSC devices are given in Table 5.17.
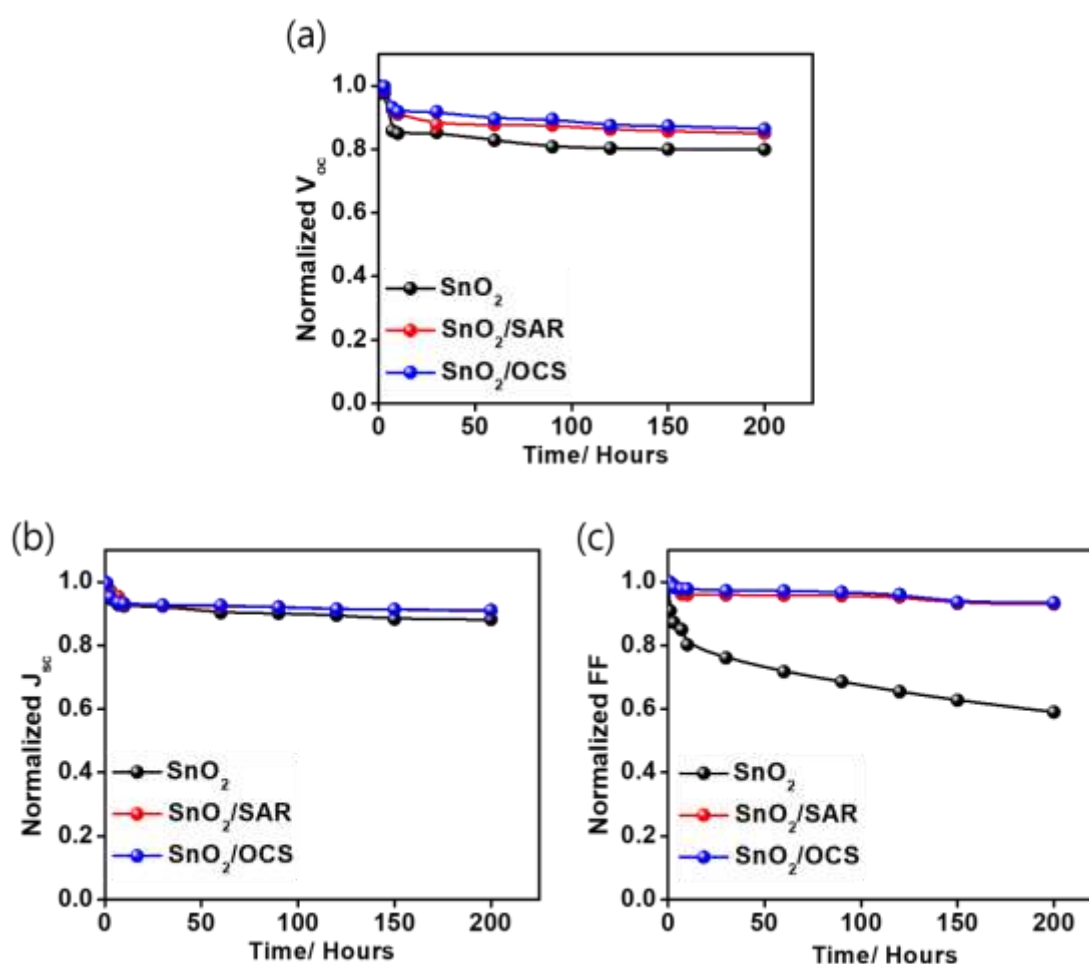
Figure 5.38: OSCs with SnO_2, SnO_2/SAR, and SnO_2/OCS ETLs during the 200 hours of thermal ageing. The evolution of (a) V_{oc}, (b) J_{sc}, and (c) FF.

Table 5. 17: The detailed V_{oc}, J_{sc}, FF, and PCE drops of thermal aged OSC devices with SnO_2, SnO_2/SAR, and SnO_2/OCS ETLs.

ETLs	LS hours	V_{oc} (V)	V_{oc} Drop	J_{sc} (mA cm^{-2})	J_{sc} Drop	FF (%)	FF Drop	PCE (%)	PCE Drop
SnO_2	0	0.79		23.80		60.06		11.32	
	200	0.63	↓20%	20.98	↓27%	35.44	↓41%	4.71	↓58%
SnO_2/SAR	0	0.79		24.48		62.88		12.24	
	200	0.68	↓14%	22.23	↓9%	58.48	↓7%	8.78	↓28%
SnO_2/OCS	0	0.79		24.52		63.92		12.39	
	200	0.68	↓14%	22.33	↓9%	59.71	↓7%	9.10	↓27%

Figure 5.38 and Table 5.17 demonstrate that the significant contribution to the higher thermal stability of OSCs with SnO_2/SAR and SnO_2/OCS ETLs was FF, which was higher during the thermal ageing period as compared to that of OSCs based on SnO_2 ETLs. To reveal the cause of the improved thermal stability of OSCs with modified SnO_2 ETLs, the morphological evolution of the ETL films after 3 h of thermal ageing was studied. AFM was utilised to measure the surface roughness of the films, as depicted in Figure 5.39.
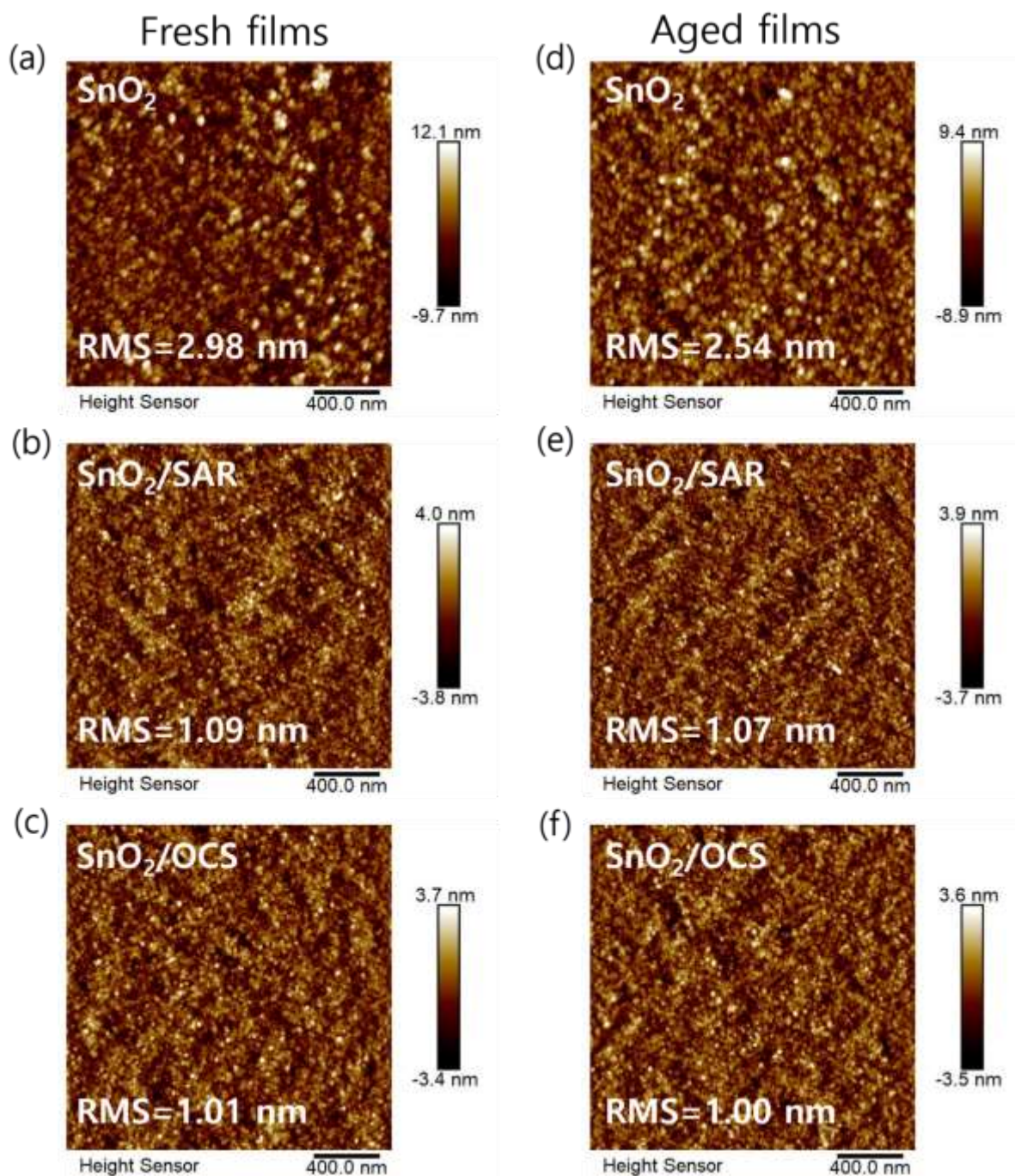
Figure 5.39: The topographic height images (from AFM) of (a-c) fresh films and (d-e) thermal aged ETL films.

The surface roughness of SnO_2 film was observed to reduce from 2.98 nm to 1.09 nm and 1.01 nm upon modification by SAR and OCS resins, respectively. A smoother ETL film is beneficial for the formation of a decent physical contact with the photoactive layer. Notably, the thermally

aged SnO_2 film showed a noticeable change in RMS, whereas the thermally aged SnO_2-modified films showed negligible changes in the RMS values. These changes in the RMS values of the films before and after thermal ageing are outlined in Table 5.18.

Table 5. 18: The changes in RMS values of various ETL films before and after thermal ageing for 3 hours.

ETL films	Surface Roughness (RMS) (nm)		
	Fresh	Aged	ΔRMS
SnO_2	2.98	2.54	0.44
SnO_2/SAR	1.09	1.07	0.02
SnO_2/OCS	1.01	1.00	0.01

The negligible change in the RMS of SnO_2 modified films upon thermal ageing demonstrates that a robust heat-resistant film was formed by UV resins modification. The formation of a robust ETL film is believed to account for the higher thermal stability observed in OSCs with the SnO_2/SAR and SnO_2/OCS ETLs. The stability results for OSCs with SnO_2 ETLs obtained in this work were compared to those obtained in other reports for OSCs based on non-fullerene acceptors with SnO_2 ETLs, as depicted in Table 5.19.

Table 5. 19: An overview of photo and thermal stability studies on non-fullerene acceptor-based inverted OSCs with SnO_2 ETLs reported up to date.

Active layer	ETLs	Stability test condition	Light source	Test time (h)	PCE drop (%)	Ref.
PM6:IT-4F	SnO_2	1 SUN	Solar simulator	24	11.0	(Jiang *et al.*, 2019)
PM6:Y6: IDIC	SnO_2-PEO	1 SUN	Solar simulator	50	73.7	(Hu *et al.*,

PM6:Y6	Co^{2+}- SnO_2	1 SUN	LED	73	20	(Zhang *et al.*, 2021)
PM6:PB2F:BTP-eC9	SnO_2/1-DPAQ	1 SUN	-	370	40.7	(Yu *et al.*, 2022)
PM6:BTP-eC9	SnO_2:PAS	1 SUN	-	1000	63.5	(Gao *et al.*, 2022)
TPD-3F:IT-4F	SnO_2	1 SUN	-	150	27	(Di Mario *et al.*, 2023b)
		120 °C in N_2	-	5	20	
PM6:L8-BO	SnO_2	1 SUN	-	100	15	(Romero *et al.*, 2023)
TPD-3F:IT-4F	SnO_2	1 SUN	-	100	13	(Romero *et al.*, 2023)
PM6:Y6-BO	SnO_2/OCS	1 SUN	Metal halide lamp	450	27	This work
		85 °C in the air	-	200	27	

As shown in Table 5.19, this study presents one of the best photo- and thermal-stability results reported so far for NFA-based inverted OSCs with SnO_2 nanoparticle ETLs.

CHAPTER SIX: CONCLUSIONS AND RECOMMENDATIONS

6.1 Conclusions

This study intended to enhance the performance and stability of NFA-based OSCs by modifying the electron transport layer. ZnO was used as the ETL in the OSCs studied. Modification of ZnO electron transport layer with commercially obtained ultraviolet resins, SAR and OCS, was successfully carried out to enhance the performance and the stability of OSCs. The optimal cross-linking times of SAR and OCS resins coated on ZnO were found to be 5 and 10 minutes, respectively whereas the optimal concentrations of SAR and OCS resins were found to be 5.2 wt%. The optical bandgaps of SAR and OCS resins were found to be 3.95 and 3.88 eV, respectively while a narrower optical bandgap of 3.28 eV was obtained for ZnO film. It was found that SAR and OCS resins could effectively reduce the WF of ZnO to bring forth an energy level match with the photoactive layer. The UV resins enhanced the hydrophobicity and minimised The γ of ZnO, thus improving the ZnO/PM6:Y6-BO interfacial contact. Using XPS and PL analyses, the effectiveness of SAR or OCS resins in reducing surface defects such as oxygen vacancies on ZnO was demonstrated. Altogether, the reduced work function, improved interfacial contact, and reduced surface defects on ZnO resulted in an improvement in the performance of OSCs from 13.6% to 14.6%. This improved PCE was supported by the increased exciton dissociation efficiency, charge transfer process, and reduced charge recombination in OSCs.

Using UV-Vis spectroscopy and Raman spectroscopy, it was demonstrated that the photocatalytic nature of ZnO, which degrades the photoactive layer upon light illumination, was mitigated by coating it with thin SAR and OCS resins. This resulted to photostability enhancement of the studied OSCs. Wherein, the OSCs with ZnO-modified ETLs retained 79% of their original PCE after 1000 h of light soaking. Conversely, OSCs with unmodified ZnO showed poor light stability, retaining only 57% of their initial efficiency after the same time. Moreover, it was demonstrated that the SAR and OCS resins formed a cross-linked network on ZnO, which was resistant to solvent washing and heat changes. The robustness of the cross-linked SAR and OCS resins improved the thermal stability of the OSCs. Specifically, OSCs with modified ZnO electron transport layers reserved 77% of their original PCE after 200 h of thermal ageing. In contrast, OSCs with ZnO ETL showed poorer stability, by retaining 54% of

their original PCE after the same time.

To prove the effectiveness of SAR and OCS resins in modifying the ETL and enhancing the PCE and the stability of organic solar cells, ZnO was replaced with SnO_2 in further investigation. The optimal concentration, post-treatment temperature, and post-treatment time of SnO_2 nanoparticles were found to be 1:6 v/v (SnO_2: water), 170 °C, and 10 minutes, respectively. The bandgap of SnO_2 film was determined to be 3.83 eV. Similar to the ZnO case, applying ultraviolet resins on SnO_2 reduced its WF from 4.0 eV to 3.86 eV, aligning its energy level with the photoactive material for effective charge extraction. Neat SnO_2 was found to be very hydrophilic based on water contact angle measurements, and it became hydrophobic upon SAR or OCS resin modification. The γ of SnO_2 was reduced upon SAR or OCS modification, resulting in improved SnO_2/photoactive layer interfacial contact. Furthermore, XPS and PL studies demonstrated that the surface defects on SnO_2, including oxygen vacancies, dangling bonds, and tin interstitials, were passivated by SAR and OCS modification. These interfacial modification results of SAR and OCS on SnO_2 resulted in a performance improvement of 13.8% to 14.4%.

Additionally, it has been demonstrated that SAR and OCS resins contribute in reducing the photodegradation of the photoactive layer materials under light illumination by the catalytic effect of SnO_2, using UV-Vis analysis. The photodegradation mitigation of the photoactive layer by SnO_2 using ultraviolet resins improved the light stability of the OSCs. The OSCs with SnO_2-modified ETLs reserved 73% of their original efficiency after 450 h of light illumination. In contrast, those based on SnO_2's neat electron transport layer retained only 20% of their initial efficiency. Moreover, it was demonstrated that both the SAR and OCS interlayers improved the thermal stability of the OSCs. Organic solar cells with SnO_2-only electron transport layer showed poor thermal stability, retaining only 42% of their original efficiency after 200 h of thermal ageing. Conversely, OSCs with SnO_2 modified with SAR and OCS resins demonstrated better thermal stability, retaining 72% and 73% of their original PCE after the same thermal ageing time. Overall, our study paves the way for commercially available ultraviolet resins to be applied as electron transport interlayers to improve the performance and stabilise OSCs.

6.2 Recommendations

This study demonstrated that organic forms of UV-curable resins based on acrylate chemical groups can increase the stability of OSCs. Therefore, further studies are recommended on the inorganic and organic-inorganic forms of ultraviolet resins. Moreover, the potential of ultraviolet resins based on other chemical groups such as azide, vinyl, epoxide, oxetane, and alkyl bromide, among others, requires investigation for application in OSCs. Further characterisation of the effect of ultraviolet resins used in this study on OSCs should be performed to realise their full potential.

REFERENCES

Abbas, Z., Ryu, S. U., Haris, M., Song, C. E., Lee, H. K., Lee, S. K., Shin, W. S., Park, T., and Lee, J. C. (2022). Optimized vertical phase separation via systematic Y6 inner side-chain modulation for non-halogen solvent processed inverted organic solar cells. *Nano Energy* **101**, 1–11.

Ahmad, T., and Zhang, D. (2020). A critical review of comparative global historical energy consumption and future demand: The story told so far. *Energy Reports* **6**, 1973–1991.

Almora, O., Cabrera, C. I., Garcia-Cerrillo, J., Kirchartz, T., Rau, U., and Brabec, C. J. (2021). Quantifying the Absorption Onset in the Quantum Efficiency of Emerging Photovoltaic Devices. *Adv. Energy Mater.* **11**, 1–9.

Alshehawy, A. M., Mansour, D. E. A., Ghali, M., Lehtonen, M., and Darwish, M. M. F. (2021). Photoluminescence spectroscopy measurements for effective condition assessment of transformer insulating oil. *Processes* **9**, 1–15.

An, K., Zhong, W., Peng, F., Deng, W., Shang, Y., Quan, H., Qiu, H., Wang, C., Liu, F., Wu, H., Li, N., Huang, F., and Ying, L. (2023a). Mastering morphology of non-fullerene acceptors towards long-term stable organic solar cells. *Nat. Commun.* **14**, 1–11.

An, K., Zhong, W., Zhu, C., Peng, F., Xu, L., Lin, Z., Wang, L., Zhou, C., Ying, L., Li, N., Huang, F., An, K., Zhong, W., Zhu, C., Peng, F., Xu, L., Lin, Z., Wang, L., and Zhou, C. (2023b). Optimizing the morphology of all-polymer solar cells for enhanced photovoltaic performance and thermal stability. *J. Semicond.* **44**, 1–9.

Anwar, M., Abdul, M. A. S., Khan, U. M., Hassan, M., Khoja, A. H., and Muchtar, A. (2022). A Review of X-ray Photoelectron Spectroscopy Technique to Analyze the Stability and Degradation Mechanism of Solid Oxide Fuel Cell Cathode Materials. *Materials* **15**, 1–23.

Armin, A., Li, W., Sandberg, O. J., Xiao, Z., Ding, L., Nelson, J., Neher, D., Vandewal, K., Shoaee, S., Wang, T., Ade, H., Heumüller, T., Brabec, C., and Meredith, P. (2021). A History and Perspective of Non-Fullerene Electron Acceptors for Organic Solar Cells. *Adv. Energy Mater.* **11**, 1–42.

Avrutin, V., Izyumskaya, N., and Morko, H. (2011). Semiconductor solar cells: Recent progress in terrestrial applications. *Superlattices Microstruct.* **49**, 337–364.

Axnanda, S., Crumlin, E. J., Mao, B., Rani, S., Chang, R., Karlsson, P. G., Edwards, M. O. M., Lundqvist, M., Moberg, R., Ross, P., Hussain, Z., and Liu, Z. (2015). Using "tender" X-ray Ambient Pressure X-Ray Photoelectron Spectroscopy as A Direct Probe of Solid-Liquid Interface. *Sci. Rep.* **5**, 1–12.

Aygül, U., Hintz, H., Egelhaaf, H. J., Distler, A., Abb, S., Peisert, H., and Chassé, T. (2013). Energy level alignment of a P3HT/fullerene blend during the initial steps of degradation. *J. Phys. Chem.C* **117**, 4992–4998.

Bai, Y., Zhao, C., Chen, X., Zhang, S., Zhang, S., Hayat, T., Alsaedi, A., Tan, Z., Hou, J., and Li, Y. (2019). Interfacial engineering and optical coupling for multicolored semitransparent inverted organic photovoltaics with a record efficiency of over 12%. *J. Mater. Chem. A* **7**, 15887–15894.

Bai, Y., Zhao, C., Zhang, S., Zhang, S., Yu, R., Hou, J., Tan, Z., and Li, Y. (2020). Printable SnO2 cathode interlayer with up to 500 nm thickness-tolerance for high-performance and large-area organic solar cells. *Sci. China Chem.* **63**, 957–965.

Cai, P., Huang, X., Zhan, T., Chen, G., Qiu, R., Zhang, L., Xue, X., Wang, Z., and Chen, J. (2021). Cross-Linkable and Alcohol-Soluble Pyridine-Incorporated Polyfluorene Derivative as a Cathode Interface Layer for High-Efficiency and Stable Organic Solar Cells. *ACS Appl. Mater. Interfaces* **13**, 12296–12304.

Cai, Y., Xie, C., Li, Q., Liu, C., Gao, J., Jee, M. H., Qiao, J., Li, Y., Song, J., Hao, X., Woo, H. Y., Tang, Z., Zhou, Y., Zhang, C., Huang, H., and Sun, Y. (2023). Improved Molecular Ordering in a Ternary Blend Enables All-Polymer Solar Cells over 18% Efficiency. *Adv. Mater.* **35**, 1–9.

Chang, M., Meng, L., Wang, Y., Ke, X., Yi, Y. Q. Q., Zheng, N., Zheng, W., Xie, Z., Zhang, M., Yi, Y., Zhang, H., Wan, X., Li, C., and Chen, Y. (2020). Achieving an Efficient and Stable Morphology in Organic Solar Cells Via Fine-Tuning the Side Chains of Small-Molecule Acceptors. *Chem. Mater.* **32**, 2593–2604.

Chen, H., Jeong, S. Y., Tian, J., Zhang, Y., Naphade, D. R., Alsufyani, M., Zhang, W., Griggs, S., Hu, H., Barlow, S., Woo, H. Y., Marder, S. R., Anthopoulos, T. D., McCulloch, I., and Lin, Y. (2023). A 19% efficient and stable organic photovoltaic device enabled by a guest nonfullerene acceptor with fibril-like morphology. *Energy Environ. Sci.* **16**, 1062–1070.

Cheng, P., and Zhan, X. (2016). Stability of organic solar cells: Challenges and strategies. *Chem. Soc. Rev.* **45**, 2544–2582.

Cho, Y. C., and Ahn, S. Il. (2020). Fabricating a Raman spectrometer using an optical pickup unit and pulsed power. *Sci. Rep.* **10**, 1–8.

Dahlström, S., Ahläng, C., Björkström, K., Forsblom, S., Granroth, B., Jansson, K., Luukkonen, A., Masood, M. T., Poulizac, J., Qudsia, S., and Nyman, M. (2020). Extraction current transients for mobility determination-A comparative study. *AIP Adv.* **10**, 1–9.

Dambhare, M. V., Butey, B., and Moharil, S. V. (2021). Solar photovoltaic technology: A review of different types of solar cells and its future trends. *J. Phys. Conf. Ser.* **1913**, 1–17.

Deng, X., Xiong, F., Li, X., Xiang, B., Li, Z., Wu, X., Guo, C., Li, X., Li, Y., Li, G., Xiong, W., and Zeng, Z. (2018). Application of atomic force microscopy in cancer research. *J. Nanobiotechnology* **16**, 1–15.

Dhere, N. G. (2006). Present status and future prospects of CIGSS thin film solar cells. *Sol. Energy Mater. Sol. Cells* **90**, 2181–2190.

Di Carlo Rasi, D., van Thiel, P. M. J. G., Bin, H., Hendriks, K. H., Heintges, G. H. L., Wienk, M. M., Becker, T., Li, Y., Riedl, T., and Janssen, R. A. J. (2019). Solution-Processed Tin Oxide-PEDOT:PSS Interconnecting Layers for Efficient Inverted and Conventional Tandem Polymer Solar Cells. *Sol. RRL* **3**, 1–10.

Di Mario, L., Garcia Romero, D., Wang, H., Tekelenburg, E. K., Meems, S., Zaharia, T., Portale, G., and Loi, M. A. (2023a). Outstanding Fill Factor in Inverted Organic Solar Cells with SnO2 by Atomic Layer Deposition. *Adv. Mater.* **2301404**, 1–10.

Di Mario, L., Garcia Romero, D., Pieters, M. J., Eller, F., Zhu, C., Bongiovanni, G., Herzig, E. M., Mura, A., and Loi, M. A. (2023b). Effects of the diphenyl ether additive in halogen-free processed non-fullerene acceptor organic solar cells. *J. Mater. Chem. A* **11**, 2419–2430.

Divya, J., Pramothkumar, A., Hilary, H. J. L., Jayanthi, P. J., and Jobe prabakar, P. C. (2021). Impact of copper (Cu) and iron (Fe) co-doping on structural, optical, magnetic and electrical properties of tin oxide (SnO2) nanoparticles for optoelectronics applications. *J. Mater. Sci. Mater. Electron.* **32**, 16775–16785.

Downes, A., and Elfick, A. (2010). Raman spectroscopy and related techniques in biomedicine. *Sensors* **10**, 1871–1889.

Duan, L., and Uddin, A. (2020). Progress in Stability of Organic Solar Cells. *Adv. Sci.* **7**, 1–39.

Duan, L., Yi, H., Zhang, Y., Haque, F., Xu, C., and Uddin, A. (2019). Comparative study of light- and thermal-induced degradation for both fullerene and non-fullerene-based organic solar cells. *Sustain. Energy Fuels* **3**, 723–735.

Ebrahimi, M., and Rahmani, D. (2019). A five-dimensional approach to sustainability for prioritizing energy production systems using a revised GRA method: A case study. *Renew. Energy* **135**, 345–354.

El Chaar, L., Lamont, L. A., and El Zein, N. (2011). Review of photovoltaic technologies. *Renew. Sustain. Energy Rev.* **15**, 2165–2175.

Fan, L., Zhang, Y., Zhang, Q., Wu, X., Cheng, J., Zhang, N., Feng, Y., and Sun, K. (2016). Graphene Aerogels with Anchored Sub-Micrometer Mulberry-Like ZnO Particles for High-Rate and Long-Cycle Anode Materials in Lithium Ion Batteries. *Small* **37**, 5208–5216.

Franke, R., Maennig, B., Petrich, A., and Pfeiffer, M. (2008). Long-term stability of tandem solar cells containing small organic molecules. *Sol. Energy Mater. Sol. Cells* **92**, 732–735.

Fu, J., Jiang, Z., Zhang, J., Chen, Q., Ma, H., Guo, X., Zhang, M., Zhou, Y., and Song, B. (2021). Highly stable inverted non-fullerene OSCs by surface modification of SnO2 with an easy-accessible material. *Chem. Eng. J.* **426**, 1–9.

Ganesamoorthy, R., Sathiyan, G., and Sakthivel, P. (2017). Review: Fullerene based acceptors for efficient bulk heterojunction organic solar cell applications. *Sol. Energy Mater. Sol. Cells* **161**, 102–148.

Gao, H., Wei, X., Yu, R., Cao, F. Y., Gong, Y., Ma, Z., Cheng, Y. J., Hsu, C. S., and Tan, Z. (2022). Coordination-Induced Defects Elimination of SnO2 Nanoparticles via a Small Electrolyte Molecule for High-Performance Inverted Organic Solar Cells. *Adv. Opt. Mater.* **10**, 1–10.

Gertsen, A. S., Castro, M. F., Søndergaard, R. R., and Andreasen, J. W. (2020). Scalable fabrication of organic solar cells based on non-fullerene acceptors. *Flex. Print. Electron.* **5**, 1–24.

Glatthaar, M., Riede, M., Keegan, N., Sylvester-Hvid, K., Zimmermann, B., Niggemann, M., Hinsch, A., and Gombert, A. (2007). Efficiency limiting factors of organic bulk heterojunction solar cells identified by electrical impedance spectroscopy. *Sol. Energy Mater. Sol. Cells* **91**, 390–393.

Gul, E., Baldinelli, G., Bartocci, P., Shamim, T., Domenighini, P., Cotana, F., Wang, J., Fantozzi, F., and Bianchi, F. (2023). Transition toward net zero emissions - Integration and optimization of renewable energy sources: Solar, hydro, and biomass with the local grid station in central Italy. *Renew. Energy* **207**, 672–686.

He, Y., and Li, Y. (2011). Fullerene derivative acceptors for high performance polymer solar cells. *Phys. Chem. Chem. Phys.* **13**, 1970–1983.

Holechek, J. L., Geli, H. M. E., Sawalhah, M. N., and Valdez, R. (2022). A Global Assessment: Can Renewable Energy Replace Fossil Fuels by 2050? *Sustainability* **14**, 1–22.

Hosenuzzaman, M., Rahim, N. A., Selvaraj, J., Hasanuzzaman, M., Malek, A. B. M. A., and Nahar, A. (2015). Global prospects, progress, policies, and environmental impact of solar photovoltaic power generation. *Renew. Sustain. Energy Rev.* **41**, 284–297.

Hu, L., Jiang, Y., Sun, L., Xie, C., Qin, F., Wang, W., and Zhou, Y. (2021). Significant Enhancement of Illumination Stability of Nonfullerene Organic Solar Cells via an Aqueous Polyethylenimine Modification. *J. Phys. Chem. Lett.* **12**, 2607–2614.

Hu, L., Zhao, N., Jiang, X., Jiang, Y., Qin, F., Sun, L., Wang, W., and Zhou, Y. (2020). Sn-N/Sn-O interaction improving electron collection in non-fullerene organic solar cells. *J. Mater. Chem. C* **8**, 12218–12223.

Huang, J., Yu, H., and Zhou, X. (2022). ZnO nanoparticles modified with biomaterial GHK-Cu as electron transport layer to fabricate highly efficient inverted polymer solar cells. *Chem. Eng. J.* **428**, 1–12.

Huang, K. T., Chen, C. P., Jiang, B. H., Jeng, R. J., and Chen, W. C. (2020a). Green poly-lysine as electron-extraction modified layer with over 15% power conversion efficiency and its application in bio-based flexible organic solar cells. *Org. Electron.* **87**, 1–9.

Huang, S., Ali, N., Huai, Z., Ren, J., Sun, Y., Zhao, X., Fu, G., Kong, W., and Yang, S. (2020b). A facile strategy for enhanced performance of inverted organic solar cells based on low-temperature solution-processed SnO2 electron transport layer. *Org. Electron.* **78**, 1–7.

Hwang, H., Sin, D. H., Park, C., and Cho, K. (2019). Ternary Organic Solar Cells Based on a Wide-Bandgap Polymer with Enhanced Power Conversion Efficiencies. *Sci. Rep.* **9**, 1–9.

Jiang, S., Chen, X., Bai, Y., Yao, J., Wakeel, M., Alhodaly, M. S., Hayat, T., and Tan, Z. (2020). Water-Soluble SnO2 Nanoparticles as the Electron Collection Layer for Efficient and Stable Inverted Organic Tandem Solar Cells. *ACS Appl. Energy Mater.* **3**, 12662–12671.

Jiang, Y., Sun, L., Jiang, F., Xie, C., Hu, L., Dong, X., Qin, F., Liu, T., Hu, L., Jiang, X., and Zhou, Y. (2019). Photocatalytic effect of ZnO on the stability of nonfullerene acceptors and its mitigation by SnO2 for nonfullerene organic solar cells. *Mater. Horizons* **6**, 1438–1443.

Jin, J., Wang, Q., Ma, K., Shen, W., Belfiore, L. A., Bao, X., and Tang, J. (2023). Recent Developments of Polymer Solar Cells with Photovoltaic Performance over 17%. *Adv. Funct. Mater.* **33**, 1–43.

Juillard, S., Planes, E., Matheron, M., Perrin, L., Berson, S., and Flandin, L. (2018). Mechanical Reliability of Flexible Encapsulated Organic Solar Cells: Characterization and Improvement. *ACS Appl. Mater. Interfaces* **10**, 29805–29813.

Kabeyi, M. J. B., and Olanrewaju, O. A. (2022). Sustainable Energy Transition for Renewable and Low Carbon Grid Electricity Generation and Supply. *Front. Energy Res.* **9**, 1–45.

Kong, T., Wang, R., Zheng, D., and Yu, J. (2021). Modification of the SnO2 Electron Transporting Layer by Using Perylene Diimide Derivative for Efficient Organic Solar Cells. *Front. Chem.* **9**, 1–8.

Korin, E., Froumin, N., and Cohen, S. (2017). Surface Analysis of Nanocomplexes by X-ray Photoelectron Spectroscopy (XPS). *ACS Biomater. Sci. Eng.* **3**, 882–889.

Kozbial, A., Li, Z., Conaway, C., McGinley, R., Dhingra, S., Vahdat, V., Zhou, F., Durso, B., Liu, H., and Li, L. (2014). Study on the surface energy of graphene by contact angle measurements. *Langmuir* **30**, 8598–8606.

Kumari, T., Lee, S. M., Kang, S. H., Chen, S., and Yang, C. (2017). Ternary solar cells with a mixed face-on and edge-on orientation enable an unprecedented efficiency of 12.1%. *Energy Environ. Sci.* **10**, 258–265.

Lan, A., Li, Y., Zhu, H., Zhu, J., Lu, H., Do, H., Lv, Y., Chen, Y., Chen, Z., Chen, F., and Huang, W. (2023). Improved Efficiency and Stability of Organic Solar Cells by Interface Modification Using Atomic Layer Deposition of Ultrathin Aluminum Oxide. *Energy Environ. Mater.* **0**, 1–9.

Laschuk, N. O., Easton, E. B., and Zenkina, O. V. (2021). Reducing the resistance for the use of electrochemical impedance spectroscopy analysis in materials chemistry. *RSC Adv.* **11**, 27925–27936.

Lazanas, A. C., and Prodromidis, M. I. (2023). Electrochemical Impedance Spectroscopy─A Tutorial. *ACS Meas. Sci. Au* **3**, 162–193.

Li, M., Zhang, Y., Xia, D., Fang, J., Xie, Q., Li, Y., Zhao, C., Xiao, C., You, S., Zhang, J., Jiang, L., Jen, A. K. Y., and Li, W. (2023c). Simple and Low-Cost Vanadyl Oxalate as Hole Transporting Layer Enables Efficient Organic Solar Cells. *Adv. Funct. Mater.* **34**, 1–8.

Li, S., Fu, Q., Meng, L., Wan, X., Ding, L., Lu, G., Lu, G., Yao, Z., Li, C., and Chen, Y. (2022b). Achieving over 18 % Efficiency Organic Solar Cell Enabled by a ZnO-Based Hybrid Electron Transport Layer with an Operational Lifetime up to 5 Years. *Angew. Chemie - Int. Ed.* **61**, 1–10.

Li, S., Xiao, Z., Li, J. J., Hu, Z. Y., Yang, Y., Kan, B., Guo, D. S., Wan, X., Yao, Z., Li, C., and Chen, Y. (2023b). Calixarenes enabling well-adjusted organic-inorganic interface for inverted organic solar cells with 18.25% efficiency and multifold improved photostability under max power point tracking. *Sci. China Chem.* **66**, 195–201.

Li, T., Chen, Z., Wang, Y., Tu, J., Deng, X., Li, Q., and Li, Z. (2020). Materials for Interfaces in Organic Solar Cells and Photodetectors. *ACS Appl. Mater. Interfaces* **12**, 3301–3326.

Li, T., Li, A., and Song, Y. (2021a). Development and utilization of renewable energy based on carbon emission reduction-evaluation of multiple mcdm methods. *Sustainability* **13**, 1–20.

Li, Y., Huang, B., Zhang, X., Ding, J., Zhang, Y., Xiao, L., Wang, B., Cheng, Q., Huang, G., Zhang, H., Yang, Y., Qi, X., Zheng, Q., Zhang, Y., Qiu, X., Liang, M., and Zhou, H. (2023a). Lifetime over 10000 hours for organic solar cells with Ir/IrOx electron-transporting layer. *Nat. Commun.* **14**, 1–10.

Li, Y., Huang, W., Zhao, D., Wang, L., Jiao, Z., Huang, Q., Wang, P., Sun, M., and Yuan, G. (2022a). Recent Progress in Organic Solar Cells: A Review on Materials from Acceptor to Donor. *Molecules* **27**, 1–31.

Li, Y., Huang, X., Ding, K., Sheriff, H. K. M., Ye, L., Liu, H., Li, C. Z., Ade, H., and Forrest, S. R. (2021c). Non-fullerene acceptor organic photovoltaics with intrinsic operational lifetimes over 30 years. *Nat. Commun.* **12**, 1–9.

Li, Z., Song, D., Xu, Z., Qiao, B., Zhao, S., Wageh, S., Al-Ghamdi, A. A., and Huo, X. (2021b). Synergetic effect of different carrier dynamics in Pm6: Y6: ITIC-M ternary cascade energy level system. *Polymers* **13**, 1–13.

Liang, Z., Zhang, Q., Jiang, L., and Cao, G. (2015). ZnO cathode buffer layers for inverted polymer solar cells. *Energy Environ. Sci.* **8**, 3442–3476.

Liber-Kneć, A., and Łagan, S. (2021). Surface testing of dental biomaterials—determination of contact angle and surface free energy. *Materials* **14**, 1–15.

Lin, T., and Dai, T. (2022). Double Cathode Modification Improves Charge Transport and Stability of Organic Solar Cells. *Energies* **15**, 1–13.

Lin, Y. K., Leong, H. Y., Ling, T. C., Lin, D. Q., and Yao, S. J. (2021). Raman spectroscopy as process analytical tool in downstream processing of biotechnology. *Chinese J. Chem. Eng.* **30**, 204–211.

Liu, B. W., Li, Z. R., Yan, L. P., Guo, J. B., Luo, Q., and Ma, C. Q. (2022). ZnO Surface Passivation with Glucose Enables Simultaneously Improving Efficiency and Stability of Inverted Polymer: Non-fullerene Solar Cells. *Chinese J. Polym. Sci.* **40**, 1594–1603.

Liu, C., Xiao, C., and Li, W. (2021). Zinc oxide nanoparticles as electron transporting interlayer in organic solar cells. *J. Mater. Chem. C* **9**, 14093–14114.

Liu, H., Liu, Z. X., Wang, S., Huang, J., Ju, H., Chen, Q., Yu, J., Chen, H., and Li, C. Z. (2019). Boosting Organic–Metal Oxide Heterojunction via Conjugated Small Molecules for Efficient and Stable Nonfullerene Polymer Solar Cells. *Adv. Energy Mater.* **9**, 1–9.

Liu, Z., Wang, L., Zhao, H., Chen, P., and Xie, X. (2023). High-performance inverted ternary organic solar cells using solution-processed tin oxide as the electron transport layer. *Org. Electron.* **120**, 1–7.

Luo, D., Jang, W., Babu, D. D., Kim, M. S., Wang, D. H., and Kyaw, A. K. K. (2022). Recent progress in organic solar cells based on non-fullerene acceptors: materials to devices. *J. Mater. Chem. A* **10**, 3255–3295.

Maheu, C., Cardenas, L., Puzenat, E., Afanasiev, P., and Geantet, C. (2018). UPS and UV spectroscopies combined to position the energy levels of TiO2 anatase and rutile nanopowders. *Phys. Chem. Chem. Phys.* **20**, 25629–25637.

Mai, T. L. H., Jeong, S., Kim, S., Jung, S., Oh, J., Sun, Z., Park, J., Lee, S., Kim, W., and Yang, C. (2023). Over 18.2%-Efficiency Organic Solar Cells with Exceptional Device Stability Enabled by Bay-Area Benzamide-Functionalized Perylene Diimide Interlayer. *Adv. Funct. Mater.* **33**, 1–10.

Mateker, W. R., and McGehee, M. D. (2017). Progress in Understanding Degradation Mechanisms and Improving Stability in Organic Photovoltaics. *Adv. Mater.* **29**, 1–16.

Mohamed El Amine, B., Zhou, Y., Li, H., Wang, Q., Xi, J., and Zhao, C. (2023). Latest Updates of Single-Junction Organic Solar Cells up to 20% Efficiency. *Energies* **16**, 1–12.

Müller, D. J., Dumitru, A. C., Lo Giudice, C., Gaub, H. E., Hinterdorfer, P., Hummer, G., De Yoreo, J. J., Dufrêne, Y. F., and Alsteens, D. (2021). Atomic Force Microscopy-Based Force Spectroscopy and Multiparametric Imaging of Biomolecular and Cellular Systems. *Chem. Rev.* **121**, 11701–11725.

Mundo-Hernández, J., De Celis Alonso, B., Hernández-Álvarez, J., and De Celis-Carrillo, B. (2014). An overview of solar photovoltaic energy in Mexico and Germany. *Renew. Sustain. Energy Rev.* **31**, 639–649.

Munir, R., Cieplechowicz, E., Lamarche, R. M., Chernikov, R., Trudel, S., and Welch, G. C. (2022). Air-Processed Organic Photovoltaics for Outdoor and Indoor Use Based upon a Tin Oxide-Perylene Diimide Electron Transporting Bilayer. *Adv. Mater. Interfaces* **9**, 1–7.

Niazi, M. R., Zhao, H., Lamarche, R. M., Munir, R., Trudel, S., Hu, J., and Welch, G. C. (2022). Cellulose Nanocrystals–Tin-Oxide Hybrid Electron Transport Layers for Solar Energy Conversion. *Adv. Mater. Interfaces* **9**, 1–7.

Palencia, M. (2017). Surface free energy of solids by contact angle measurements. *J. Sci. with Technol. Appl.* **2**, 84–93.

Pastuszak, J., and Węgierek, P. (2022). Photovoltaic Cell Generations and Current Research Directions for Their Development. *Materials* **15**, 1–30.

Peng, R., Yan, T., Chen, J., Yang, S., Ge, Z., and Wang, M. (2020). Passivating Surface Defects of n-SnO2 Electron Transporting Layer by InP/ZnS Quantum Dots: Toward Efficient and Stable Organic Solar Cells. *Adv. Electron. Mater.* **6**, 1–10.

Planes, E., Juillard, S., Matheron, M., Charvin, N., Cros, S., Qian, D., Zhang, F., Berson, S., and Flandin, L. (2020). Encapsulation Effect on Performance and Stability of Organic Solar Cells. *Adv. Mater. Interfaces* **7**, 1–13.

Pletikapia, G., and Ivoševi Denardis, N. (2017). Application of surface analytical methods for hazardous situation in the Adriatic Sea: Monitoring of organic matter dynamics and oil pollution. *Nat. Hazards Earth Syst. Sci.* **17**, 31–44.

Ramadhani, F., Supriyanto, A., Ahmad, M. K. Bin, Diyanahesa, N. E.-H., and Saputri, D. G. (2019). Optical properties of dye DN-F01 as sensitizer. *J. Phys. Theor. Appl.* **3**, 36–42.

Rathore, N., Panwar, N. L., Yettou, F., and Gama, A. (2021). A comprehensive review of different types of solar photovoltaic cells and their applications. *Int. J. Ambient Energy* **42**, 1200–1217.

Rocha, F. S., Gomes, A. J., Lunardi, C. N., Kaliaguine, S., and Patience, G. S. (2018). Experimental methods in chemical engineering: Ultraviolet visible spectroscopy—UV-Vis. *Can. J. Chem. Eng.* **96**, 2512–2517.

Romero, D. G., Mario, L. Di, Yan, F., Ibarra-barreno, C. M., Mutalik, S., Protesescu, L., Rudolf, P., and Loi, M. A. (2023). Understanding the Surface Chemistry of SnO 2 Nanoparticles for High Performance and Stable Organic Solar Cells. *Adv. Funct. Mater.* **2307958**, 1–10 .

Rudawska, A., and Jacniacka, E. (2009). Analysis for determining surface free energy uncertainty by the Owen-Wendt method. *Int. J. Adhes. Adhes.* **29**, 451–457.

Sampaio, P. G. V., and González, M. O. A. (2017). Photovoltaic solar energy: Conceptual framework. *Renew. Sustain. Energy Rev.* **74**, 590–601.

Schauer, F. (2005). Space-charge-limited currents for organic solar cells optimisation. *Sol. Energy Mater. Sol. Cells* **87**, 235–250.

Shockley, W., and Queisser, H. J. (1961). Detailed balance limit of efficiency of p-n junction solar cells. *J. Appl. Phys.* **32**, 510–519.

Solak, E. K., and Irmak, E. (2023). Advances in organic photovoltaic cells: a comprehensive review of materials, technologies, and performance. *RSC Adv.* **13**, 12244–12269.

Song, X., Song, Y., Xu, H., Gao, S., Wang, Y., Li, J., Hai, J., Liu, W., and Zhu, W. (2023). Solvent-Induced Anti-Aggregation Evolution on Small Molecule Electron-Transporting Layer for Efficient, Scalable, and Robust Organic Solar Cells. *Adv. Energy Mater.* **13**, 1–11.

Soultati, A., Verykios, A., Panagiotakis, S., Armadorou, K. K., Haider, M. I., Kaltzoglou, A., Drivas, C., Fakharuddin, A., Bao, X., Yang, C., Yusoff, A. R. B. M., Evangelou, E. K., Petsalakis, I., Kennou, S., Falaras, P., Yannakopoulou, K., Pistolis, G., Argitis, P., and Vasilopoulou, M. (2020). Suppressing the Photocatalytic Activity of Zinc Oxide Electron-Transport Layer in Nonfullerene Organic Solar Cells with a Pyrene-Bodipy Interlayer. *ACS Appl. Mater. Interfaces* **12**, 21961–21973.

Spanggaard, H., and Krebs, F. C. (2004). A brief history of the development of organic and polymeric photovoltaics. *Sol. Energy Mater. Sol. Cells* **83**, 125–146.

Su, L. Y., Huang, H. H., Tsai, C. E., Hou, C. H., Shyue, J. J., Lu, C. H., Pao, C. W., Yu, M. H., Wang, L., and Chueh, C. C. (2022). Improving Thermal and Photostability of Polymer Solar Cells by Robust Interface Engineering. *Small* **18**, 1–12.

Sun, L., Chen, Y., Sun, M., and Zheng, Y. (2023). Organic Solar Cells: Physical Principle and Recent Advances. *Chem. - An Asian J.* **18**, 1–12.

Sun, Y., Lu, S., Xu, R., Liu, K., Zhou, Z., Yue, S., Azam, M., Ren, K., Wei, Z., Wang, Z., Qu, S., Lei, Y., and Wang, Z. (2019). Collection optimization of photo-generated charge carriers for efficient organic solar cells. *J. Power Sources* **412**, 465–471.

Suo, Z., Xiao, Z., Li, S., Liu, J., Xin, Y., Meng, L., Liang, H., Kan, B., Yao, Z., Li, C., Wan, X., and Chen, Y. (2023). Efficient and stable inverted structure organic solar cells utilizing surface-modified SnO2 as the electron transport layer. *Nano Energy* **118**, 1–8.

Swami, S. K., Khan, J. I., Dutta, V., Lee, J., Laquai, F., and Chaturvedi, N. (2023). Spray-Deposited Aluminum-Doped Zinc Oxide as an Efficient Electron Transport Layer for Inverted Organic Solar Cells. *ACS Appl. Energy Mater.* **6**, 2906–2913.

Taghizadeh, A., Leffers, U., Pedersen, T. G., and Thygesen, K. S. (2020). A library of ab initio Raman spectra for automated identification of 2D materials. *Nat. Commun.* **11**, 1–10.

Tang, C. W. (1986). Two-layer organic photovoltaic cell. *Appl. Phys. Lett.* **48**, 183–185.

Tauc, J., Grigorovici, R., and Vancu, A. (1966). Optical Properties and Electronic Structure of Amorphous Germanium. *Phys. status solidi* **15**, 627–637.

Vadhva, P., Hu, J., Johnson, M. J., Stocker, R., Braglia, M., Brett, D. J. L., and Rettie, A. J. E. (2021). Electrochemical Impedance Spectroscopy for All-Solid-State Batteries: Theory, Methods and Future Outlook. *ChemElectroChem* **8**, 1930–1947.

Viezbicke, B. D., Patel, S., Davis, B. E., and Birnie, D. P. (2015). Evaluation of the Tauc method for optical absorption edge determination: ZnO thin films as a model system. *Phys. Status Solidi Basic Res.* **252**, 1700–1710.

Vodapally, S. N., and Ali, M. H. (2022). A Comprehensive Review of Solar Photovoltaic (PV) Technologies, Architecture, and Its Applications to Improved Efficiency. *Energies* **16**, 1–18.

Voroshazi, E., Uytterhoeven, G., Cnops, K., Conard, T., Favia, P., Bender, H., Muller, R., and Cheyns, D. (2015). Root-cause failure analysis of photocurrent loss in polythiophene:Fullerene-based inverted solar cells. *ACS Appl. Mater. Interfaces* **7**, 618–623.

Whitten, J. E. (2023). Ultraviolet photoelectron spectroscopy: Practical aspects and best practices. *Appl. Surf. Sci. Adv.* **13**, 1–11.

Wu, J., Tang, F., Wu, S., Li, Y., Xiao, L., and Zhu, X. (2023). Interface Modification of Tin Oxide Electron-Transport Layer for the Efficiency and Stability Enhancement of Organic Solar Cells. *Adv. Energy Mater.* **14**, 1–11.

Xu, X., Li, D., Yuan, J., Zhou, Y., and Zou, Y. (2021). Recent advances in stability of organic solar cells. *EnergyChem* **3**, 1–41.

Xu, X., Xiao, J., Zhang, G., Wei, L., Jiao, X., Yip, H. L., and Cao, Y. (2020). Interface-enhanced organic solar cells with extrapolated T80 lifetimes of over 20 years. *Sci. Bull.* **65**, 208–216.

Xue, R., Zhang, J., Li, Y., and Li, Y. (2018). Organic Solar Cell Materials toward Commercialization. *Small* **14**, 1–24.

Yan, L., Wang, Y., Zhao, W., Zha, H., Song, H., Hao, H., Hao, Y., Luo, Q., Liu, F., Yang, Y., Su, Q., Wang, H., and Ma, C. Q. (2023). Simultaneous UV and air stability improvement of organic solar cells enabled by carbon-coated zinc oxide as cathode buffer layer. *Cell Reports Phys. Sci.* **4**, 1–18.

Yang, S., and Yu, H. (2023). The modification of ZnO surface with natural antioxidants to fabricate highly efficient and stable inverted organic solar cells. *Chem. Eng. J.* **452**, 1–11.

Yu, R., Wei, X., Wu, G., Zhang, T., Gong, Y., Zhao, B., Hou, J., Yang, C., and Tan, Z. (2022). Efficient interface modification via multi-site coordination for improved efficiency and stability in organic solar cells. *Energy Environ. Sci.* **15**, 822–829.

Zhang, C., Heumueller, T., Leon, S., Gruber, W., Burlafinger, K., Tang, X., Perea, J. D., Wabra, I., Hirsch, A., Unruh, T., Li, N., and Brabec, C. J. (2019a). A top-down strategy identifying molecular phase stabilizers to overcome microstructure instabilities in organic solar cells. *Energy Environ. Sci.* **12**, 1078–1087.

Zhang, Y., Lang, Y., and Li, G. (2023). Recent advances of non-fullerene organic solar cells: From materials and morphology to devices and applications. *EcoMat* **5**, 1–23.

Zhang, Y., Xu, Y., Ford, M. J., Li, F., Sun, J., Ling, X., Wang, Y., Gu, J., Yuan, J., and Ma, W. (2018). Thermally Stable All-Polymer Solar Cells with High Tolerance on Blend Ratios. *Adv. Energy Mater.* **8**, 1–10.

Zhang, Y., Zhao, X., Han, X., Li, Y., Zhang, Z., Li, T., Xing, J., Zuo, X., and Lin, Y. (2021). Co2+-Tuned Tin Oxide Interfaces for Enhanced Stability of Organic Solar Cells. *Langmuir* **37**, 3173–3179.

Zhang, Z., Wang, W., Korpacz, A. N., Dufour, C. R., Weiland, Z. J., Lambert, C. R., and Timko, M. T. (2019b). Binary Liquid Mixture Contact-Angle Measurements for Precise Estimation of Surface Free Energy. *Langmuir* **35**, 12317–12325.

Zhao, F., Deng, L., Wang, K., Han, C., Liu, Z., Yu, H., Li, J., and Hu, B. (2020). Surface Modification of SnO2 via MAPbI3 Nanowires for a Highly Efficient Non-Fullerene Acceptor-Based Organic Solar Cell. *ACS Appl. Mater. Interfaces* **12**, 5120–5127.

Zhao, F., Wang, C., and Zhan, X. (2018). Morphology Control in Organic Solar Cells. *Adv. Energy Mater.* **8**, 1–34.

Zhao, W., Li, S., Yao, H., Zhang, S., Zhang, Y., Yang, B., and Hou, J. (2017). Molecular Optimization Enables over 13% Efficiency in Organic Solar Cells. *J. Am. Chem. Soc.* **139**, 7148–7151.

Zheng, Z., Wang, J., Bi, P., Ren, J., Wang, Y., Yang, Y., Liu, X., Zhang, S., and Hou, J. (2022). Tandem Organic Solar Cell with 20.2% Efficiency. *Joule* **6**, 171–184.

Zhu, X., Guo, B., Fang, J., Zhai, T., Wang, Y., Li, G., Zhang, J., Wei, Z., Duhm, S., Guo, X., Zhang, M., and Li, Y. (2019). Surface modification of ZnO electron transport layers with glycine for efficient inverted non-fullerene polymer solar cells. *Org. Electron.* **70**, 25–31.

Internet References

National Renewable Energy Laboratory. (2024). Best Research-Cell Efficiencies: https://www.nrel.gov/pv/cell-efficiency.html.

APPENDICES

The following peer reviewed publications and presentations came out of this research work.

A. Peer Reviewed Publications

1. Mbilo, M., Haris, M., Ryu, D. H., Mwabora, J. M., Musembi, R. J., Lee, S., Song, C. E., and Shin, W. S. (2024). Improved Light Soaking and Thermal Stability of Organic Solar Cells by Robust Interfacial Modification. *Adv. Energy Sustainability Res.* **5**, (2300210) 1–10. https://doi.org/10.1002/aesr.202300210

2. Mbilo, M., Ryu, D.H., Lee, S., Haris, M., Mwabora, J.M., Musembi, R.J., Lee, H.K., Lee, S.K., Song, C.E., and Shin, W.S. (2024). Highly efficient and stable organic solar cells with SnO2 electron transport layer enabled by UV-curing acrylate oligomers. *J. Energy Chem.* **92**, 124–131. https://doi.org/10.1016/j.jechem.2024.01.022

B. Conference Presentations

1. Mwende Mbilo, Won Suk Shin, Chang Eun Song, Julius Mwakondo Mwabora and Robinson Juma Musembi (2023). Improved Performance and Stability of Organic Solar Cells Enabled by Interface Engineering. *Korea Photovoltaic Society Spring Conference, Busan, Korea.*

2. Mwende Mbilo, Won Suk Shin, Chang Eun Song, Julius Mwakondo Mwabora and Robinson Juma Musembi. (2023). Enhanced Thermal and Light Soaking Stability of Polymer Solar Cells by Interface Modification. *The Polymer Society of Korea Spring Conference, Daejeon, Korea.*

3. Mwende Mbilo, Muhammad Haris, Du Hyeon Ryu, Julius Mwakondo Mwabora, Robinson Juma Musembi, Chang Eun Song and Won Suk Shin. (2023). Highly Stable Organic Solar Cells Enabled by Robust Interface Modification. *The Global Photovoltaic Society Conference, Gwangju, Korea.*